博士論文

Application of Continuumnization for the Analysis of Dynamic Characteristics of Brick Structures

(連続体化の組積造構造物動的特性解析への適用)

A DISSERTATION
SUBMITTED TO THE DEPARTMENT OF CIVIL ENGINEERING
OF THE GRADUATE SCHOOL OF ENGINEERING,
UNIVERSITY OF TOKYO
IN PARTIAL FULFILLMENT OF THE REQUIREMENTS
FOR THE DEGREE OF
DOCTOR OF PHILOSOPHY

Sumet Supprasert
(スプラサート・スメット)
March, 2017

Application of Continuumnization for the Analysis of Dynamic Characteristics of Brick Structures

Sumet Supprasert

March 8, 2017

Acknowledgement

First of all, I would like to express my deep sense gratitude and appreciation to Prof. Lalith Wijerathne and Prof. Muneo Hori for their guidance and support during 3 years of my research. This 3 year research could not be done without their supports. Specifically, Lalith Wijerathne taught me how to manage stress and encouraged me to be brave enough to give presentations though I am a fearful speaker.

I also express the gratitude for my committees, Prof. Tsuyoshi Ichimura, Prof. Kohei Nagai, Prof. Hide Sakaguchi, for kind advises during examination. Their comments provide a lot of improvement of my thesis.

I would like to thank the Ministry of Education, Culture, Sports, Science and Technology of Japan (MEXT) for awarding me scholarship. This gives me the opportunity to study in Japan as a doctoral student and to develop both my country and Japan.

Moreover, I would like to thank Earthquake Research Institute (ERI) for providing supports, like high performance computer, research room. These supports make me convenient to do my research.

Also, I am thankful to my lab friends, especially to Muhammad Rizwan Riaz, Wasuwat Petprakop and all others for there kind supports. My research life is happy because of them.

I would like to thank my friends form different laboratories, Jetpan Wetwitoo and Punyawut Jiradilok. They make my life in Japan fun. Also, I can complain everything to them.

I would like to express gratitude to my parents, brother and elder sister for their encouragement and support to fulfill this task.

Finally, I would like to express my love to my favorite singer, Miku Hatsune. Her existence gives me a lot of meaning of my life because her songs make me realize that I can be a happy person even in the most sadness situation. Her sound give me future.

Abstract

Although discrete models are commonly used in numerical simulation of brick structures, alternated equivalent continuum form can provide some advantages. This continuum form allows one to analytically study dynamic characteristics of brick structure for given brick-mortar geometric and material properties. With this analytical solution, we can verify numerical discrete codes. In addition, the continuum form allows us to formulate finite element model (FEM) for brick structures. This FEM implementation allows one to use commercial software to analyze brick models using proper structural elements such as beams or shells without writing computational code. Also it is convenient to use the analytical solution and FEM implementation in design proposes.

This study aims to use an approximation treatment called continuumniztion to derive the equivalent continuum form of discrete governing equations and obtain analytical prediction of dynamic characteristic. Once the analytical prediction is verified, continuumniztion based Particle Discretization Scheme Finite Element Method (PDS-FEM) implementation is formulated. Finally hypothesis of the role of high frequency rotation is to be explored.

Before applying continuumnzation, a regularly packed brick-mortar systems is constructed. In this system, bricks are assumed to be rigid blocks and mortar are assumed to be tiny linear springs with normal and tangential constants. Based on Hamilton principle, discrete equations of motion of the system are obtained. This equations consist of the equation of translation and equation of rotation. Also there are coupling term between translation and rotation.

Based on the continuumnzation, it is assumed that brick size are small such that the relative motions of discrete equations of motion can be replaced by gradient term. With this approach continuumnized equations of motion are obtained.

mortar systems. Using Fourier transform with respect to length and time, a characteristic equation in frequency-wavelength domain can be obtained. Solving the characteristic equation, the relation between frequency and wave number is obtained. For relatively long wavelength, analytical wave phase velocities of p-wave and s-wave are predicted. Also, the corresponding modes including rotational wave are obtained.

To verify the analytical solutions based on continuumnzation, a numerical model of 2d brick wall is constructed. The numerical model is subjected by 2 cases of input condition at the center of the model. First is translational input to compare the wavefronts for a given travel time. Second is rotational input to compare the relation between wave frequency and wavenumber for givens length domain. According to the verification, the analytical wavefront are in good agreement with

numerical wavefront, especially for horizontal and vertical propagation of waves which is commonly occur in earthquake engineering. For the frequency-wavenumber relation, the numerical relation and the analytical relation are in good agreement for wavelengh longer than 7 times of the size of bricks which is sufficient for civil engineer.

Continuumnized based FEM of brick structures can be derived. Since bricks are rigid particles, PDS-FEM can be can provide better representation of brick movements. Unlike standard FEM, the derivatives of translation and rotation are approximate on a triangle formed by centers of 3 neighboring bricks such that characteristic function is 1 for inside the triangle and 0 for outside. To obtain the range of applicability of the PDS-FEM, numerical simulations of PDS-FEM were verified with RBSM and analytically predict frequency wave number relation. According to the results, the continuumnzation based PDS-FEM is applicable for wavelengh longer than 7 times of the size of bricks which is sufficient for civil engineer.

According to the analytical solution of continuumnization and numerical solution of PDS-FEM, high frequency of rotation is observed which is possible to be one of the sources of damping. To study the effect of the rotational damping, the special care of damping model is required instead of using Rayleigh damping which lacks of physical explanation. To study the effect of rotation on the damping mechanism, the rotation in equation of rotation is derived in term of translation and substituted in to the equation of translation. With this approach the single equation of translation which include the effect of damping due to high frequency rotation is obtained. According to the numerical experiment of the damping, small energy dissipation is observed. This can conclude that high frequency rotation can be one of the sources of damping.

To conclude, this study formulate the governing equations of the equivalent continuum brick mass-spring system and applied them for three main applications. First, frequency-wavenumber relation of p-, s- and rotational waves and corresponding wave speed are predicted. Second, PDS-DEM for brick wall is formulated. According to its verification, PDS-DEM for brick wall is applicable for civil engineering applications. Finally, the damping term which include brick mortar properties unlike empirical damping is obtained.

Contents

List of Figures

Chapter 1

Introduction

Although discrete models like DEM and RBSM are useful for analysis of brick structures, continuum model can provides us advantages in some applications. For example, we can obtain analytical solutions of governing equations of continuum system. With the obtained analytical solutions, we can predict dynamic characteristics, like wave frequency or velocity, for given brick arrangement, size, density, and brick-mortar material property. For verification proposes, we can use the predicted dynamic characteristics to check the accuracy of numerical simulation of discrete models. For design proposes, we can choose proper brick-mortar geometric and material property for desired dynamic characteristic without blindly using numerical trial and error as there are many parameters like brick geometry, arrangement and brick-mortar material properties. Also, the equivalent continuous governing equation can be simplified to construct simpler model like beam or shell and make us easy to design brick structures.

The equivalent continuum systems is a bridge to effectively use the numerical methods used in continuum mechanics, like FEM, to analyze brick structures. With FEM, it is simple to use powerful commercial software to analyze brick structures without writing computational code. Further, the brick-mortar FEM can be simulated along with other mostly used materials like concrete and steel seamlessly. Obviously, these continuum models, and possibly simplified structural models like shells based on continuum form for analyzing brick structures, will be quite attractive solutions for brick structure designers.

The mechanism of damping of brick structures or particle systems, like sand, is poorly understood and current analysis of damping such systems are heavily rely on empirical relations obtained from experimental observations. Though Rayleigh damping can be empirically used for continuum system, there is no physical explanation of this kind of damping. Understanding the underlying mechanism of damping of granular materials, brick structures, etc. is one of the important problem in engineering and physics. The continuum models would be useful in exploring the mechanism of damping in granule systems or brick structures.

This research aims to uses an approximation tool called continuumnization proposed by Hori et al[1] in order to obtain the continuum form of governing equations of brick structures and explore its applications. Based on the continuumnization, the discrete relative translations and rotations

of discrete regularly packed particles are approximate to be equivalent continuum vector fields assuming that the particles are relatively small compared to wavelength. With this approximation, continuumnized governing equations of particle motion of the brick-mortar system is obtained. With this continuumnized governing equations, this research aims to predict dynamic characteristic of brick mortar systems for verification propose. In addition to the continuumnization, higher accurate continuum forms with wider range of applicability also are developed and their applications are explored.

For further application, this research aims to develop FEM for brick structures based on the continuumnization. Since standard FEM might not provide us a good representation of brick movement as the brick structures are generally set of particles, this research uses particle discretization scheme finite element method (PDS-FEM)[2] of continuumnized brick-mortar system instead of standard FEM. In PDS-FEM for brick structures, the characteristic function is defined on a brick itself. As PDS-FEM is particle schemed, the movement of bricks can be well represented. Also, geometric property like mass moment of inertia in PDS-FEM is well defined.

Though there are lacks of understanding of damping mechanism as explained earlier, there is a hypothesis that the high frequency rotation of particles can be one of the sources of damping[1]. To test this hypothesis, this research aims to use the continuumnizaton to analytically investigate the role of high frequency rotation. Once the damping term due to high frequency rotation is defined, this research aims to develop PDS-FEM of the damped systems. Then, the effect of the damping term will be numerically studied..

1.1 Thesis structure

This thesis consists of 8 chapters and several appendices. The contents of the thesis are expressed as follows. Chapter 2 shows the past researches of several types of modeling of brick structures, specially for the use of continuum form of brick structures. Chapter 3 explains the continuumnization of the spherical systems. Dynamic characteristics of the system are predicted and verified with RBSM to explores its applicable range. Chapter 4 shows the formulation of the continuumnized governing equations of brick structures and prediction of dynamic characteristics of the system. Also, the continuumnization of brick structures is verified like chapter 3. Chapter 5 explains the use of the continuumnization of brick wall to formulate PDS-FEM for conunuumnized brick wall systems. Then, chapter 6 explains the exploration of the role of rotation on damping mechanism of brick walls. Finally, chapter 7 expresses the concluding remark of the whole research and some idea for future research.

Chapter 2

Literature Review

The modeling of brick structures can be characterized by two main types based on assumptions of the brick-mortar material. The first type is discrete model assuming that the bricks are rigid blocks. The second type is continuum model assuming continuous material that can represent brick and mortar properties.

Since brick structures generally consist of brick units and mortar, discrete models are widely used. For small movement of brick particles, many researchers use rigid body spring model (RBSM)[3, 4, 5, 6, 7] assuming that bricks are rigid blocks and mortar is infinitesimal small springs with normal and tangential spring constants. With RBSM, it is simple to include cracking in mortar[7]. In addition, some simulate the crack of brick units for various cracking modes[5]. In case of large movement of brick units, it is common to use discrete element model (DEM)[8, 9, 10]. It's popular in simulations of collapse of brick structures[9].

While discrete model of brick structures are very useful in brick structural analysis as described above, it is troublesome for design purposes. What is preferred in design of brick structures is simple means to predict the characteristics of different combinations of brick mortar properties and brick arrangement, simplified numerical models like shells and beams for brick structures, etc. Availability of some equivalent continuum models for brick structures would address these needs. At the same time, these continuum models can be useful in finding analytical solutions which is one of the most desired in the verification of RBSM or DEM codes.

There are numbers of method to obtain continuum form of brick structures. Standard finite element model (FEM) with solid elements smaller than brick sizes and mortar thickness can be implemented[11, 12] to study micro structural behaviors. In this model, elastic properties of bricks and mortar can be directly applied to solid elements of brick and mortar. This method can provide high accuracy since there is no assumption. However, it is not suitable for preliminary design purposes or simulating large structures since the computational cost is high due to the involvement of a large degrees of freedoms. To model such a large size of brick structures, brick-mortar materials are converted into equivalent homogeneous material so-called homogenization in order to reduce degree of freedom. In this method, equivalent material property of the continuous domain can be obtained by the average of brick and mortar's properties[13, 14, 15]. Alternatively,

equivalent material property can be obtained by validation of experimental wave velocity using sonic tests[16, 17, 18]. However, assuming the brick-mortar to be isotopic ignoring the effect of brick arrangement causes the lack of accuracy. Thus, this method is not reliable to predict dynamic characteristics.

Equivalent continuum form that can provide reliable analytical prediction of dynamic characteristic for verification purpose have been found in regularly packed spherical mass-spring systems[19, 20, 21]. To obtain the equivalent continuum form, discrete translation and rotation in discrete governing equations are approximated based on second order Taylor's expansion[21]. This approximation method can be useful to verify the discrete system with long wavelength. For example, dynamic characteristics such as the wave frequency-wavenumber relation and wave velocity are predicted analytically. The expansion for short wavelength is also applied assuming the results of equation of motion to be complex exponential wave function[21] . However, assuming wave function to be the results of equation is not rigorous as the analytical solutions could be any functions other than wave function.

Stefanou et al. have obtained equivalent continuum form of regularly arranged brick structures based on second order Taylor's expansion[22]. With the equivalent continuous governing equation, they have analytically predicted frequency-wavenumber relation. Further, they applied the same method for periodic arrangement of brick wall[23]. With the continuum form of governing equation proposed by Stefanou et al., FEM which includes rotational degree of freedom can be constructed [28]. Note that obtaining the continuum form of randomly arranged is also applicable[26].

Other method of obtaining continuum form is to assume the relative translation and rotation as gradient term[24, 25]. The main different between this approach and Taylor's expansion is that the gradient term directly represent the continuous translational and rotational vector field.

One of the dynamic characteristics of brick structures that have not been explored is the mechanism of damping. Understanding the damping mechanism of particle systems is one of the important problem both in engineering and physics. Though, there are various experimental research, such as effect of damage damping ratio[30], its mechanism cannot be well explained. In analysis of discrete model, damping term is model by the rate of deformation of springs induce non-conservative force[31, 32, 33]. For continuum form, Rayleigh damping is used[34]. Though damping property can be obtained by experiments, there are lack of physical explanation of viscous damping. Though there are some research on energy dissipation due to rocking[37, 38], the dissipation does not cause viscous damping since it is not velocity dependent.

A key of rational modeling of damping in particle mass-spring system is found in Hori et al's research [1]. Hori et al.[1] developed continuumnization to obtain the continuum form of the rigid spherical mass-spring systems. Unlike the approximation based in second order Taylor's expansion described earlier, continuumnization approximate the relative translation and rotation of neighboring particles to be gradient term in the assumption that wave length is relatively longer than the size of particle. According to analytical solutions based on the continuumnization, Hori et al.[1] propose the hypothesis that high frequency rotation might cause damping in particle systems.

2.1 Observation from literature review

Though analytical solutions usable for the verification of RBSM or DEM models have been proposed, these solutions can be further improved increasing the accuracy and the range of applicability. Though such improvements are not essential for ordinary engineering applications, some special engineering applications and most probably some applications in physics may benefit from these improvements. Also, these accurate solutions with wider range of applicability will be quite useful in verification of general numerical codes or particle types simulations.

The FEM of brick structure may not proper as the bricks are basically particles. As alternative method called particle discretization scheme finite element method (PDS-FEM)[2] could provide better representation of brick translation and rotation as PDS-FEM is particle typed model as well as brick particles. The formulation of PDS-FEM is expressed in chapter 5.

There are lacks of understanding of viscous damping mechanism of brick structures. However, Hori et al.[1] proposes a hypothesis that high frequency rotation of particle mass-spring systems may cause damping. This hypothesis could be explored based on the continuumnization.

2.2 Objectives of the current work

The Objectives of the current work are expressed as follows

- Derive the equivalent continuum forms for brick structures
  - Based on Continuumnization
  - Based on Taylor series expansion
- Explore the applications of continuum forms
  - Obtain analytical solutions for verification of RBSM
  - Formulate PDS-FEM for brick structures
- Test the hypothesis that high frequency rotation can be a source of damping in brick structures or particle systems

Chapter 3

Continuumnization of spherical mass-spring systems

Continuumnization can be applied to idealize a regularly packed interacting particle system as a continuum. The resulting equivalent continuum form lead to two major advantages: enable to analytically predict the particle system's dynamic characteristics; and enables to use numerical tools used in continuum mechanics, like FEM, to analyze particle systems. Though only linearly interacting particle systems are considered in this thesis, it is a possibility to extend to nonliearly interacting particles.

The original proposal on continuumnization by Hori et al. idealizes a regularly packed particle system as a continuum by considering the limit of particle size going to zero. Hence the name continuumnization. Though conceptually different, the same governing equation obtained with of continuumnization can be derived based on a Taylor series approach. The major difference between continuumnization and the Taylor series approach is that the latter does not involve the limiting process. While the author independently developed this Taylor series based approach,Stefanou et al. have proposed a similar technique in reference [22]. An interesting reader is referred to Stefanou et al.[22] for a summary of several homogenization techniques used to derive equivalent continuum forms for regularly packed mass spring systems. In therir work, Stefanou et al. only considered the case of first order expansion for the rotation. In this thesis, the second order and infinite order cases are considered. As it is demonstrated in the latter half of this chapter, the infinite series solution is valid for wider range of frequencies, while continuumnization and second order Taylor series solutions are applicable for low frequency ranges.

In this chapter, the continuumnization and the Taylor series approaches are presented. 2D hexagonally packed spherical mas spring system is considered for the simplicity. The analytically obtained dynamic characteristics are compared with those from Rigid Body Spring Model (RBSM). Application of continuumnization for regularly arranged brick mortar system is presented in the next section.

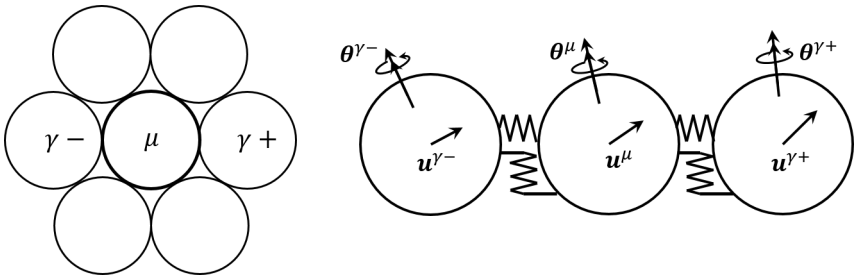

Figure 3.1: Regularly packed sphere Connection of a sphere μ and two neighbors $\gamma\pm$ with normal spring constant, k, and tangential spring constant, h.

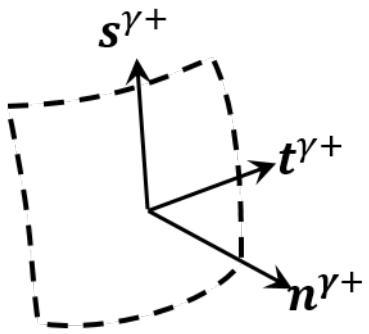

Figure 3.2: Contact point of the connection between the sphere μ and the neighbor $\gamma+$.

3.1 Equations of motion of a discrete sphere system

Consider large collection of regularly packed spherical particles on a plane. The mass of each spherical particle is m while the radius is a. The spherical particles are assumed to be connected with elastic springs at the contact surface. Figure 3.1 shows a particle μ and its six neighbors in three directions; $\gamma\pm$ denotes neighbors in opposite directions. At each contact point, neighbors are assumed to be connected with infinitesimal small linear elastic springs of stiffness k and h in normal and tangential directions, respectively. As shown in Figure 3.2, the normal and two tangential unit vectors at the contact surface with γ^+ are $\boldsymbol{n}^{\gamma+}$, $\boldsymbol{t}^{\gamma+}$, and $\boldsymbol{s}^{\gamma+}$, where $\boldsymbol{n}^{\gamma+}=\boldsymbol{t}^{\gamma+}\times \boldsymbol{s}^{\gamma+}$.

3.1.1 Potential energy of the system

Given the translation and rotation of a particle μ, $\boldsymbol{u}^{\mu}$ and $\boldsymbol{\theta}^{\mu}$, and those of its neighbor $\gamma+$, $\boldsymbol{u}^{\gamma+}$ and $\boldsymbol{\theta}^{\gamma+}$, their relative movements at the contact point can be expressed as

$$\boldsymbol{L}^{\mu\gamma+}=\boldsymbol{u}^{\gamma+}-\boldsymbol{u}^{\mu}-a\left(\boldsymbol{\theta}^{\gamma+}+\boldsymbol{\theta}^{\mu}\right)\times\boldsymbol{n}^{\gamma+}. \tag{3.1}$$

The corresponding elastic potential energy , $V^{\mu\gamma+}$, can be expressed as

$$V^{\mu\gamma+} = \frac{1}{2}k\left(\boldsymbol{n}^{\gamma+}\cdot\boldsymbol{L}^{\mu\gamma+}\right)^2+\frac{1}{2}h\left(\boldsymbol{t}^{\gamma+}\cdot\boldsymbol{L}^{\mu\gamma+}\right)^2+\frac{1}{2}h\left(\boldsymbol{s}^{\gamma+}\cdot\boldsymbol{L}^{\mu\gamma+}\right)^2 \tag{3.2}$$

3.1.2 First variation of potential energy

From Eq. 3.2, the first variation of spring energy,$\delta V^{\mu\gamma+}$, can be expressed as

$$\begin{aligned}\delta V^{\mu\gamma+} &= \left\{-\boldsymbol{K}^{\gamma+}\cdot\left(\boldsymbol{u}^{\gamma+}-\boldsymbol{u}^{\mu}\right)+\hat{\boldsymbol{K}}^{\gamma+}\cdot\left(\boldsymbol{\theta}^{\gamma+}+\boldsymbol{\theta}^{\mu}\right)\right\}\cdot\delta\boldsymbol{u}^{\mu}\\ &\quad+\left\{-\left(\hat{\boldsymbol{K}}^{\gamma+}\right)^{\mathrm{T}}\cdot\left(\boldsymbol{u}^{\gamma+}-\boldsymbol{u}^{\mu}\right)+\overline{\boldsymbol{K}}^{\gamma+}\cdot\left(\boldsymbol{\theta}^{\gamma+}+\boldsymbol{\theta}^{\mu}\right)\right\}\cdot\delta\boldsymbol{\theta}^{\mu}\end{aligned}$$

where

$$\begin{aligned}\boldsymbol{K}^{\gamma+} &= k\boldsymbol{n}^{\gamma+}\otimes\boldsymbol{n}^{\gamma+}+h\boldsymbol{t}^{\gamma+}\otimes\boldsymbol{t}^{\gamma+}+h\boldsymbol{s}^{\gamma+}\otimes\boldsymbol{s}^{\gamma+}\\ \hat{\boldsymbol{K}}^{\gamma+} &= ah\left(\boldsymbol{t}^{\gamma+}\otimes\boldsymbol{s}^{\gamma+}-\boldsymbol{s}^{\gamma+}\otimes\boldsymbol{t}^{\gamma+}\right)\\ \overline{\boldsymbol{K}}^{\gamma+} &= a^2h\left(\boldsymbol{t}^{\gamma+}\otimes\boldsymbol{t}^{\gamma+}+\boldsymbol{s}^{\gamma+}\otimes\boldsymbol{s}^{\gamma+}\right).\end{aligned}$$

Using symmetry, it is straightforward to express the corresponding matrices, $\boldsymbol{K}^{\gamma-}$, $\hat{\boldsymbol{K}}^{\gamma-}$ and $\overline{\boldsymbol{K}}^{\gamma-}$, for the particle pair μ and$\gamma-$; $\boldsymbol{K}^{\gamma-}=\boldsymbol{K}^{\gamma+}$, $\hat{\boldsymbol{K}}^{\gamma-}=-\hat{\boldsymbol{K}}^{\gamma+}$, and $\overline{\boldsymbol{K}}^{\gamma-}=\overline{\boldsymbol{K}}^{\gamma+}$.

Taking the summation over all the three directions of γ's for all the particles in the domain, we can express the first variation of the total potential energy of the mass spring system as

$$\begin{aligned}\delta V &= \sum_{\mu}\sum_{\gamma}\left(\delta V^{\mu\gamma+}+\delta V^{\mu\gamma-}\right)\\ &= \sum_{\mu}\sum_{\gamma}\left\{-\boldsymbol{K}^{\gamma}\cdot\left(\boldsymbol{u}^{\gamma+}-2\boldsymbol{u}^{\mu}-\boldsymbol{u}^{\gamma-}\right)+\hat{\boldsymbol{K}}^{\gamma}\cdot\left(\boldsymbol{\theta}^{\gamma+}-\boldsymbol{\theta}^{\gamma-}\right)\right\}\cdot\delta\boldsymbol{u}^{\mu} \qquad (3.3)\\ &\quad+\left\{-\left(\hat{\boldsymbol{K}}^{\gamma}\right)^{\mathrm{T}}\cdot\left(\boldsymbol{u}^{\gamma+}-\boldsymbol{u}^{\gamma-}\right)+\overline{\boldsymbol{K}}^{\gamma}\cdot\left(\boldsymbol{\theta}^{\gamma+}+2\boldsymbol{\theta}^{\mu}+\boldsymbol{\theta}^{\gamma-}\right)\right\}\cdot\delta\boldsymbol{\theta}^{\mu} \qquad (3.4)\end{aligned}$$

3.1.3 First variation of kinetic energy

For given translational and angular speeds of, $\dot{\boldsymbol{u}}^{\mu}$ and $\dot{\boldsymbol{\theta}}^{\mu}$, the kinetic energy, T, of the mass spring system is

$$T=\sum_{\mu}\left(\frac{1}{2}m\dot{\boldsymbol{u}}^{\mu}\cdot\dot{\boldsymbol{u}}^{\mu}+\frac{1}{2}\dot{\boldsymbol{\theta}}^{\mu}\cdot\boldsymbol{I}\cdot\dot{\boldsymbol{\theta}}^{\mu}\right).$$

It is straightforward to obtain the first variation of kinetic energy as

$$\delta T=\sum_{\mu}\left\{\frac{\mathrm{d}}{\mathrm{d}t}(m\dot{\boldsymbol{u}}^{\mu}\cdot\delta\boldsymbol{u}^{\mu})-m\ddot{\boldsymbol{u}}^{\mu}\cdot\delta\boldsymbol{u}^{\mu}+\frac{\mathrm{d}}{\mathrm{d}t}\{(\boldsymbol{I}\cdot\boldsymbol{\theta}^{\mu})\cdot\delta\boldsymbol{\theta}^{\mu}\}-\left(\boldsymbol{I}\cdot\ddot{\boldsymbol{\theta}}^{\mu}\right)\cdot\delta\boldsymbol{\theta}^{\mu}\right\}. \tag{3.5}$$

3.1.4 Equations of motion

According to the hamilton's principle, the above conservative system evolves such that

$$\delta\int_{t_1}^{t_2}(T-V)\,\mathrm{d}t=0 \tag{3.6}$$

Substituting Eq. 3.4 and 3.5 into Eq. 3.6, we can obtain

$$\begin{aligned}0 \;=\; &-\int_{t_1}^{t_2}\sum_{\gamma}\Big\{\Big\{\boldsymbol{K}^{\gamma}\cdot\big(\boldsymbol{u}^{\gamma+}-2\boldsymbol{u}^{\mu}-\boldsymbol{u}^{\gamma-}\big)-\hat{\boldsymbol{K}}^{\gamma}\cdot\big(\boldsymbol{\theta}^{\gamma+}-\boldsymbol{\theta}^{\gamma-}\big)\Big\}\cdot\delta\boldsymbol{u}^{\mu}\\ &\Big\{\Big(\hat{\boldsymbol{K}}^{\gamma}\Big)^{\mathrm{T}}\cdot\big(\boldsymbol{u}^{\gamma+}-\boldsymbol{u}^{\gamma-}\big)-\overline{\boldsymbol{K}}^{\gamma}\cdot\big(\boldsymbol{\theta}^{\gamma+}+2\boldsymbol{\theta}^{\mu}+\boldsymbol{\theta}^{\gamma-}\big)\Big\}\cdot\delta\boldsymbol{\theta}^{\mu}\\ &+m\ddot{\boldsymbol{u}}^{\mu}\cdot\delta\boldsymbol{u}^{\mu}+\left(\boldsymbol{I}\cdot\ddot{\boldsymbol{\theta}}^{\mu}\right)\cdot\delta\boldsymbol{\theta}^{\mu}\Big\}\,\mathrm{d}t.\end{aligned}$$

Since the above equation should hole for compatible arbitrary variations $\delta\boldsymbol{u}^{\mu}$ and $\delta\boldsymbol{u}^{\mu}$, we can obtain the following pair of governing equations for our spherical mass-spring system.

$$\begin{aligned}m\ddot{\boldsymbol{u}}^{\mu}-\sum_{\gamma}\boldsymbol{K}^{\gamma}\cdot\big(\boldsymbol{u}^{\gamma+}-2\boldsymbol{u}^{\mu}+\boldsymbol{u}^{\gamma-}\big)+\sum_{\gamma}\hat{\boldsymbol{K}}^{\gamma}\cdot\big(\boldsymbol{\theta}^{\gamma+}-\boldsymbol{\theta}^{\gamma-}\big) &= \boldsymbol{0}\\ \boldsymbol{I}\cdot\ddot{\boldsymbol{\theta}}^{\mu}-\sum_{\gamma}\Big(\hat{\boldsymbol{K}}^{\gamma}\Big)^{\mathrm{T}}\cdot\big(\boldsymbol{u}^{\gamma+}-\boldsymbol{u}^{\gamma-}\big)+\sum_{\gamma}\overline{\boldsymbol{K}}^{\gamma}\cdot\big(\boldsymbol{\theta}^{\gamma+}+2\boldsymbol{\theta}^{\mu}+\boldsymbol{\theta}^{\gamma-}\big) &= \boldsymbol{0}\end{aligned} \tag{3.7}$$

In the above pair, the first is the governing equation for translational components, while the second is that for the rotational components. It is seen that these pair of equations are coupled via the matrix $\hat{\boldsymbol{K}}^{\gamma}$.

3.2 Equivalent continuum form for the discrete system

In this section, we derive an equivalent continuum form for the above considered discrete governing equations for the mass-spring system. The above obtained governing equations for the discrete variables, $\boldsymbol{u}^{\mu}$ and $\boldsymbol{\theta}^{\mu}$, are of little use in identifying the characteristics of the mass spring system. Often, characteristics fo such discrete systems are analytically studied using equivalent continuum forms. Stefanou et al.[22] has summarized several homogenization techniques used to derive equivalent continuum forms for regularly packed mass spring systems. Instead of these standard homogenization techniques, we use continuumnization proposed by Hori et al. and a Taylor series

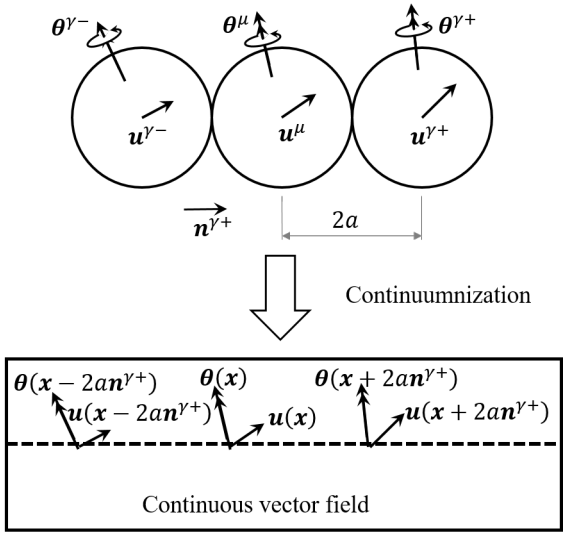

Figure 3.3: Concept of the continuumnization of the spherical system.

based approach with which higher order accurate predictions can be made. Details of formulations of these two methods are presented in the rest of this sub-section.

In deriving equivalent continuum forms, we assume that there exists two vector fields $\boldsymbol{u}(\boldsymbol{x})$ and $\boldsymbol{\theta}(\boldsymbol{x})$ which satisfy $\boldsymbol{u}(\boldsymbol{x}^{\mu})=\boldsymbol{u}^{\mu}$ and $\boldsymbol{\theta}(\boldsymbol{x}^{\mu})=\boldsymbol{\theta}^{\mu}$ (see Figure 3.3).

3.2.1 Continuumnization

Continuumnization proposed by Hori et al. [1] assumes that, in a regularly packed particle system, the particles are small compared to the dimensions of the domain occupied by the particles or the wave lengths of interest, and idealizes the particle system as a continuum considering the limit of particle size going to zero. This assumption of particle size is small compared to a certain length scale of interest allows to approximate relative discrete displacement gradients of discrete vector field as a directional derivative of a continuous vector field. As examples, we can make following approximations involving first and second order directional derivatives.

$$\lim_{a\longrightarrow 0}\frac{\boldsymbol{u}^{\gamma\pm}-\boldsymbol{u}^{\mu}}{2a}\approx\pm\boldsymbol{n}^{\gamma+}\cdot\nabla\boldsymbol{u} \tag{3.8}$$

$$\lim_{a\longrightarrow 0}\frac{\boldsymbol{u}^{\gamma+}-2\boldsymbol{u}^{\mu}+\boldsymbol{u}^{\gamma-}}{4a^2} \approx \boldsymbol{n}^{\gamma+}\cdot\nabla\left(\boldsymbol{n}^{\gamma+}\cdot\nabla\boldsymbol{u}\right) \tag{3.9}$$

Based on the above pair of approximations, we can approximate the following discrete terms in terms of continuous vector fields as

$$\boldsymbol{u}^{\gamma+}-2\boldsymbol{u}^{\mu}+\boldsymbol{u}^{\gamma-} \approx 4a^2\boldsymbol{n}^{\gamma+}\cdot\nabla\left(\boldsymbol{n}^{\gamma+}\cdot\nabla\boldsymbol{u}\right), \tag{3.10}$$

$$\boldsymbol{u}^{\gamma+}-\boldsymbol{u}^{\gamma-} \approx 4a\boldsymbol{n}^{\gamma+}\cdot\nabla\boldsymbol{u}, \tag{3.11}$$

$$\boldsymbol{\theta}^{\gamma+}-\boldsymbol{\theta}^{\gamma-}\approx 4a\boldsymbol{n}^{\gamma+}\cdot\nabla\boldsymbol{\theta}, \tag{3.12}$$

$$\boldsymbol{\theta}^{\gamma+}+2\boldsymbol{\theta}^{\mu}+\boldsymbol{\theta}^{\gamma-} \approx 4\boldsymbol{\theta}. \tag{3.13}$$

Substituting Eq. 3.10 and 3.11 into Eq. 3.7, we get the continuum for of the governing equations for translations.

$$\begin{aligned} m\ddot{u}_j &= 4a^2\sum_{\gamma}\frac{\partial}{\partial x_i}\left(kn_i^{\gamma+}n_j^{\gamma+}n_k^{\gamma+}n_l^{\gamma+}+hn_i^{\gamma+}t_j^{\gamma+}n_k^{\gamma+}t_l^{\gamma+}+hn_i^{\gamma+}s_j^{\gamma+}n_k^{\gamma+}s_l^{\gamma+}\right)\left(\frac{\partial}{\partial x_k}u_l\right) \\ &\quad -4a^2\sum_{\gamma}h\left(t_j^{\gamma+}n_k^{\gamma+}s_l^{\gamma+}-s_j^{\gamma+}n_k^{\gamma+}t_l^{\gamma+}\right)\left(\frac{\partial}{\partial x_k}\theta_l\right) \end{aligned}$$

Note that we use the fact that $\frac{\partial \boldsymbol{n}^{\gamma}}{\partial x_i}=\frac{\partial \boldsymbol{s}^{\gamma}}{\partial x_i}=\frac{\partial \boldsymbol{t}^{\gamma}}{\partial x_i}=0$. Similarly, substituting Eq. 3.12 and Eq. 3.13, we can obtain the the continuum form for the Eq. 3.7 as

$$I\ddot{\theta}_j = a^2\sum_{\gamma}h\left(t_j^{\gamma+}n_k^{\gamma+}s_l^{\gamma+}-s_j^{\gamma+}n_k^{\gamma+}t_l^{\gamma+}\right)\left(\frac{\partial}{\partial x_k}u_l\right)-4a^2\sum_{\gamma}h\left(t_k^{\gamma+}t_l^{\gamma+}+s_k^{\gamma+}s_l^{\gamma+}\right)(\theta_l)$$

Thus, the continuumnized equations of motion can be written as

$$\begin{aligned} m\ddot{\boldsymbol{u}}-4a^3\nabla\cdot(\boldsymbol{c}\colon\nabla\boldsymbol{u})-4a^3\boldsymbol{q}^{\mathrm{T}}\colon\nabla\boldsymbol{\theta} &= \boldsymbol{0} \\ \boldsymbol{I}\cdot\ddot{\boldsymbol{\theta}}+4a^3\boldsymbol{q}\colon\nabla\boldsymbol{u}4-a^3\boldsymbol{d}\cdot\boldsymbol{\theta} &= \boldsymbol{0}, \end{aligned} \tag{3.14}$$

where

$$
\begin{aligned}
\boldsymbol{c} &= \sum_{\gamma}\left\{\frac{k}{a}\boldsymbol{n}^{\gamma+}\otimes\boldsymbol{n}^{\gamma+}\otimes\boldsymbol{n}^{\gamma+}\otimes\boldsymbol{n}^{\gamma+}+\frac{h}{a}\left(\boldsymbol{n}^{\gamma+}\otimes\boldsymbol{t}^{\gamma+}\otimes\boldsymbol{n}^{\gamma+}\otimes\boldsymbol{t}^{\gamma+}+\boldsymbol{n}^{\gamma+}\otimes\boldsymbol{s}^{\gamma+}\otimes\boldsymbol{n}^{\gamma+}\otimes\boldsymbol{s}^{\gamma+}\right)\right\}\\
\boldsymbol{q} &= \frac{h}{a}\sum_{\gamma}\left(h\boldsymbol{t}^{\gamma+}\otimes\boldsymbol{n}^{\gamma+}\otimes\boldsymbol{s}^{\gamma+}-h\boldsymbol{s}^{\gamma+}\otimes\boldsymbol{n}^{\gamma+}\otimes\boldsymbol{t}^{\gamma+}\right)\\
\boldsymbol{d} &= \frac{h}{a}\sum_{\gamma}\left(h\boldsymbol{s}^{\gamma+}\otimes\boldsymbol{s}^{\gamma+}+h\boldsymbol{t}^{\gamma+}\otimes\boldsymbol{t}^{\gamma+}\right)
\end{aligned}
\tag{3.15}
$$

We call the above set of equations in Eq. 3.14 governing equations of continuumnization (GEC). The tensors $\boldsymbol{c}$, $\boldsymbol{q}$ and $\boldsymbol{d}$ depends only on the radius of spheres, spring constants and unit vectors which are defined by the particle arrangement. In Eq. 3.14, $m\ddot{\boldsymbol{u}}-4a^3\nabla\cdot(\boldsymbol{c}\colon\nabla\boldsymbol{u})$ corresponds to wave equations in the continuum mechanics. The tensor $\boldsymbol{q}$ couples the two sets of equations in Eq. 3.14; note that $q^{\mathrm{T}}_{ijk}=q_{kji}$.

3.2.2 Continuum form based on second order Taylor expansion (CFSTE)

As mentioned at the start of this chapter, a continuum form for our discrete system can be derived based on a Taylor series approach. Based on homogenization techniques, Stefanou et al. have proposed a similar technique in reference [22]. While they have considered only the case of first order approximation for $\boldsymbol{\theta}$, here we consider a second order approximation. For the sake of brevity, we use the abbreviation CFSTE for this method.

In the Taylor expansion approach, as described in section 3.2, it is assumed that there exist smooth fields $\boldsymbol{u}(\boldsymbol{x})$ and $\boldsymbol{\theta}(\boldsymbol{x})$ which satisfy $\boldsymbol{u}(\boldsymbol{x}^{\mu})=\boldsymbol{u}^{\mu}$ and $\boldsymbol{\theta}(\boldsymbol{x}^{\mu})=\boldsymbol{\theta}^{\mu}$ (see Figure 3.3).Provided $\boldsymbol{u}(\boldsymbol{x})$ and $\boldsymbol{\theta}(\boldsymbol{x})$ are sufficiently smooth, we can obtain the following relations for $\boldsymbol{u}(\boldsymbol{x}\pm 2a\boldsymbol{n}^{\gamma+})$ considering Taylor expansion up to second order terms.

$$
\boldsymbol{u}(\boldsymbol{x}+2a\boldsymbol{n}^{\gamma+})-\boldsymbol{u}(\boldsymbol{x})\approx-2a\frac{\partial\boldsymbol{u}(\boldsymbol{x})}{\partial x_i}n_i^{\gamma+}+\frac{(2a)^2}{2!}\frac{\partial^2\boldsymbol{u}(\boldsymbol{x})}{\partial x_i\partial x_j}n_i^{\gamma+}n_j^{\gamma+} \tag{3.16}
$$

$$
\boldsymbol{u}(\boldsymbol{x}-2a\boldsymbol{n}^{\gamma+})-\boldsymbol{u}(\boldsymbol{x})\approx-2a\frac{\partial\boldsymbol{u}(\boldsymbol{x})}{\partial x_i}n_i^{\gamma+}+\frac{(2a)^2}{2!}\frac{\partial^2\boldsymbol{u}(\boldsymbol{x})}{\partial x_i\partial x_j}n_i^{\gamma+}n_j^{\gamma+}. \tag{3.17}
$$

Combining Eq. 3.16 and Eq. 3.17, we can approximate the following discrete vector expressions of translations as

$$\begin{aligned}
\boldsymbol{u}^{\gamma+}-2\boldsymbol{u}^{\mu}+\boldsymbol{u}^{\gamma-} &\approx \boldsymbol{u}(\boldsymbol{x}+2a\boldsymbol{n}^{\gamma+})-2\boldsymbol{u}(\boldsymbol{x})+\boldsymbol{u}(\boldsymbol{x}-2a\boldsymbol{n}^{\gamma+}) \\
&\approx 4a^2 n_i^{\gamma+} n_j^{\gamma+} \frac{\partial^2 \boldsymbol{u}}{\partial x_i \partial x_j} \qquad (3.18) \\
\boldsymbol{u}^{\gamma+}-\boldsymbol{u}^{\gamma-} &\approx \boldsymbol{u}(\boldsymbol{x}+2a\boldsymbol{n}^{\gamma+})-\boldsymbol{u}(\boldsymbol{x}-2a\boldsymbol{n}^{\gamma+}) \\
&\approx 4a n_i^{\gamma+} \frac{\partial \boldsymbol{u}}{\partial x_i}. \qquad (3.19)
\end{aligned}$$

Similarly, we can approximate discrete vector expressions of rotations as

$$\begin{aligned}
\boldsymbol{\theta}^{\gamma+}-\boldsymbol{\theta}^{\gamma-} &\approx \boldsymbol{\theta}(\boldsymbol{x}+2a\boldsymbol{n}^{\gamma+})-\boldsymbol{\theta}(\boldsymbol{x}-2a\boldsymbol{n}^{\gamma+}) \\
&\approx 4a n_i^{\gamma+} \frac{\partial \boldsymbol{\theta}}{\partial x_i} \qquad (3.20) \\
\boldsymbol{\theta}^{\gamma+}+2\boldsymbol{\theta}^{\mu}+\boldsymbol{\theta}^{\gamma-} &\approx \boldsymbol{\theta}(\boldsymbol{x}+2a\boldsymbol{n}^{\gamma+})+2\boldsymbol{\theta}(\boldsymbol{x})+\boldsymbol{\theta}(\boldsymbol{x}-2a\boldsymbol{n}^{\gamma+}) \\
&\approx 4\boldsymbol{\theta}+4a^2 n_i^{\gamma+} n_j^{\gamma+} \frac{\partial^2 \boldsymbol{\theta}}{\partial x_i \partial x_j} \qquad (3.21)
\end{aligned}$$

As it seen, the approximations in Eq. 3.18, 3.19, 3.20 and Eq. 3.21 are the same as those of continuumnization, except that the last contains a second order term.

Substitute Eq. 3.18, 3.19 into Eq. 3.7, we obtain

$$\begin{aligned}
I\ddot{\theta}_j &= a^2 \sum_{\gamma} h\left(t_j^{\gamma+} n_k^{\gamma+} s_l^{\gamma+} - s_j^{\gamma+} n_k^{\gamma+} t_l^{\gamma+}\right)\left(\frac{\partial}{\partial x_k} u_l\right) - 4a^2 \sum_{\gamma} h\left(t_j^{\gamma+} t_l^{\gamma+} + s_j^{\gamma+} s_l^{\gamma+}\right)(\theta_l) \\
&\quad -4a^4 \sum_{\gamma} h \frac{\partial}{\partial x_i}\left(n_i^{\gamma+} t_j^{\gamma+} n_k^{\gamma+} t_l^{\gamma+} + n_i^{\gamma+} s_j^{\gamma+} n_k^{\gamma+} s_l^{\gamma+}\right)\left(\frac{\partial}{\partial x_k}\theta_l\right)
\end{aligned}$$

Thus, the continuumnized equation of motion of the regularly packed spherical system for SOC can be written as

$$\begin{aligned}
m\ddot{\boldsymbol{u}} - 4a^3 \nabla\cdot(\boldsymbol{c}\colon \nabla \boldsymbol{u}) - 4a^3 \boldsymbol{q}^{\mathrm{T}}\colon \nabla\boldsymbol{\theta} &= \mathbf{0} \\
\boldsymbol{I}\cdot\ddot{\boldsymbol{\theta}} + 4a^3 \boldsymbol{q}\colon \nabla\boldsymbol{u} - 4a^3 \boldsymbol{d}\cdot\boldsymbol{\theta} - 4a^5 \nabla\cdot(\boldsymbol{v}\colon \nabla\boldsymbol{\theta}) &= \mathbf{0} \qquad (3.22)
\end{aligned}$$

where

$$\boldsymbol{v} = \sum_{\gamma} \frac{h}{a}\left(\boldsymbol{n}^{\gamma+}\otimes\boldsymbol{t}^{\gamma+}\otimes\boldsymbol{n}^{\gamma+}\otimes\boldsymbol{t}^{\gamma+} + \boldsymbol{n}^{\gamma+}\otimes\boldsymbol{s}^{\gamma+}\otimes\boldsymbol{n}^{\gamma+}\otimes\boldsymbol{s}^{\gamma+}\right). \qquad (3.23)$$

As seen, the above continuum form based on second order Taylor expansion is identical to that of continuumnization, except the second order term $\nabla\cdot(\boldsymbol{v}\colon\nabla\boldsymbol{\theta})$ in the former. . Unlike continuumnization, the Taylor series approach does not involve the limiting process, $\lim_{a\longrightarrow 0}$, in approximating the difference of discrete variables in terms of derivatives of continuous vector fields. Although both approaches produces exactly the same governing equations, there is a fundamental difference; continuumnization idealizes the discrete particle system as a hypothetical continuum while the Taylor series approach approximates the discrete vector fields with a sufficiently smooth continuous vector fields.

3.3 Analytical solution to the characteristic equation

Unlike the governing equations of discrete vector fields, the continuum forms allows one to study the characteristics of the system analytically. In this section, the analytical relations between wave speeds and wave numbers are obtained by solving characteristic equations of two continuum forms we obtained in section 3.2. In addition to those two, we study the characteristics of one additional continuum form obtained considering all the infinite terms in Taylor series; follows the same steps as in section 3.2.2 with whole Taylor series. Characteristic equations of continuum forms

The characteristic equations of the continuum forms are obtained taking the Fourier transform,$\mathcal{F}$, with the kernel of $e^{\imath(\boldsymbol{\xi}\cdot\boldsymbol{x}-\omega t)}$. The Fourier transform of the derivatives appearing in the continuum forms can be expressed as

$$\begin{aligned}
-\mathcal{F}\Big(\nabla\cdot(\boldsymbol{c}\colon\nabla\boldsymbol{u})_j\Big) &= \xi_i\xi_k c_{ijkl}U_l \\
\mathcal{F}\big((\boldsymbol{q}\colon\nabla\boldsymbol{\theta})_i\big) &= \imath\xi_j q_{ijk}\Theta_k \\
-\mathcal{F}\big(\big(\boldsymbol{q}^{\mathrm{T}}\colon\nabla\boldsymbol{u}\big)_i\big) &= -\imath\xi_j q_{kji}U_k \\
\mathcal{F}\big((\boldsymbol{d}\cdot\boldsymbol{\theta})_i\big) &= d_{ij}\Theta_j \\
\mathcal{F}\Big((\nabla\cdot(\boldsymbol{v}\colon\nabla\boldsymbol{\theta}))_j\Big) &= -\xi_i\xi_k v_{ijkl}\Theta_l,
\end{aligned} \tag{3.24}$$

where Fourier transform of a function $f(\boldsymbol{x},t)$ is denoted as $\mathcal{F}(f(\boldsymbol{x},t))$, and $U_i{=}\mathcal{F}(u_i)$ and $\Theta_i{=}\mathcal{F}(\theta_i)$.

For 2D settings being considered, let vector $\boldsymbol{\xi}{=}\{\xi_1,\xi_2\}$ in Fourier domain be expressed as $\boldsymbol{\xi}{=}\xi\{\cos\theta_\xi,\sin\theta_\xi\}$, where ξ is the magnitude of the wave number (i.e. $\xi{=}\frac{1}{\lambda}$ where λ is the wave length) and θ_ξ is the direction of the propagation of the wave (Figure 3.4).

substituting Eq. 3.24 into Eq. 3.22 the characteristic equation for continnumnization can be obtained as

$$\det\begin{bmatrix}
\big(\frac{9k}{8a}{+}\frac{3h}{8a}\big)\xi^2{-}\frac{\pi\rho}{3}\omega^2 & \big(\frac{3k}{8a}{-}\frac{3h}{8a}\big)\xi^2\sin2\theta_\xi & -\frac{3h\xi\imath}{2a}\sin2\theta_\xi \\
\big(\frac{3k}{8a}{-}\frac{3h}{8a}\big)\xi^2\sin2\theta_\xi & \big(\frac{9k}{8a}{+}\frac{3h}{8a}\big)\xi^2{-}\frac{\pi\rho}{3}\omega^2 & \frac{3h\xi\imath}{2a}\cos2\theta_\xi \\
\frac{3h\xi\imath}{2a}\sin2\theta_\xi & -\frac{3h\xi\imath}{2a}\cos2\theta_\xi & \frac{3h}{a}{-}\frac{2\pi a^2\rho\omega^2}{15}
\end{bmatrix} = 0 \tag{3.25}$$

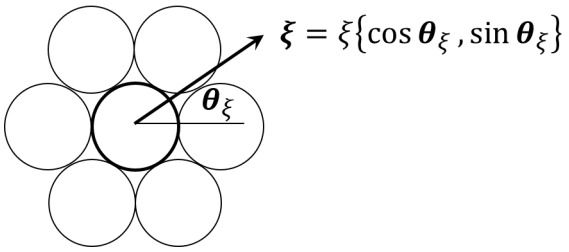

Figure 3.4: Wave number and direction of the propagating wave

while that for the second order Taylor expansion obtained from Eq. 3.22 is

$$\det\begin{bmatrix} \left(\frac{9k}{8a}+\frac{3h}{8a}\right)\xi^2-\frac{\pi\rho}{3}\omega^2 & \left(\frac{3k}{8a}-\frac{3h}{8a}\right)\xi^2\sin 2\theta_\xi & -\frac{3h\xi\imath}{2a}\sin 2\theta_\xi \\ \left(\frac{3k}{8a}-\frac{3h}{8a}\right)\xi^2\sin 2\theta_\xi & \left(\frac{9k}{8a}+\frac{3h}{8a}\right)\xi^2-\frac{\pi\rho}{3}\omega^2 & \frac{3h\xi\imath}{2a}\cos 2\theta_\xi \\ \frac{3h\xi\imath}{2a}\sin 2\theta_\xi & -\frac{3h\xi\imath}{2a}\cos 2\theta_\xi & \frac{3h}{a}-\frac{3ha}{2}\xi^2-\frac{2\pi a^2\rho\omega^2}{15} \end{bmatrix}=0 \tag{3.26}$$

3.3.1 Characteristic equations based on infinite Taylor series

In section 3.2.2, Taylor series up to the second order terms are considered in deriving continuum form. Unlike in that second order approach, here we consider another continuum form taking all the infinite terms of Taylor series into account. We use the abbreviation CFITE for this method. While the process is the same as that of section 3.2.2, the resulting continuum form is of no practice use. Interestingly, the presence of some series solutions makes it possible analytically study the characteristic equations of this continuum form with infinite terms. The characteristic equations from this infinite Taylor series approach is (see Appendix C for details of the derivation)

$$\det\begin{bmatrix} 4\sum_\gamma K_{11}^\gamma \sin^2(a\boldsymbol{\xi}\cdot\boldsymbol{n}^\gamma)-m\omega^2 & 4\sum_\gamma K_{12}^\gamma \sin^2(a\boldsymbol{\xi}\cdot\boldsymbol{n}^\gamma) & 2\sum_\gamma e^{\imath\pi/2}\hat{K}_{13}^\gamma \sin(2a\boldsymbol{\xi}\cdot\boldsymbol{n}^\gamma) \\ 4\sum_\gamma K_{21}^\gamma \sin^2(a\boldsymbol{\xi}\cdot\boldsymbol{n}^\gamma) & 4\sum_\gamma K_{22}^\gamma \sin^2(a\boldsymbol{\xi}\cdot\boldsymbol{n}^\gamma)-m\omega^2 & 2\sum_\gamma e^{\imath\pi/2}\hat{K}_{23}^\gamma \sin(2a\boldsymbol{\xi}\cdot\boldsymbol{n}^\gamma) \\ 2\sum_\gamma e^{\imath\pi/2}\hat{K}_{31}^\gamma \sin(2a\boldsymbol{\xi}\cdot\boldsymbol{n}^\gamma) & 2\sum_\gamma e^{\imath\pi/2}\hat{K}_{32}^\gamma \sin(2a\boldsymbol{\xi}\cdot\boldsymbol{n}^\gamma) & 4\sum_\gamma \bar{K}_{33}^\gamma \cos^2(a\boldsymbol{\xi}\cdot\boldsymbol{n}^\gamma)-I_{33}\omega^2 \end{bmatrix}=0 \tag{3.27}$$

For the sake of brevity, we call this Taylor series approch with infinite terms as ISC.

3.3.2 Relation between frequency and wavenumber

Solving the Eq. 3.25, we can obtain the following $\omega-\xi$ relations for the continuum form obtained with continuumnization

$$\omega^2=\begin{cases} \frac{3}{2m}(3k+h)(\xi a)^2 \\ \frac{3}{4m}\left\{(\xi a)^2(3h+k)-20h-a\sqrt{A}\right\} \\ \frac{3}{4m}\left\{(\xi a)^2(3h+k)-20h+a\sqrt{A}\right\} \end{cases} \tag{3.28}$$

Table 3.1: Wave speeds and corresponding modes $\{u_1, u_2, \theta_3\}$

wave	speed	mode shape
p	$a\sqrt{\frac{3}{2}}\sqrt{\frac{3k+h}{m}}$	$\{\cos\theta_\xi, \sin\theta_\xi, 0\}$
s	$a\sqrt{\frac{3}{2}}\sqrt{\frac{k+h}{m}}$	$\left\{-\sin\theta_\xi, \cos\theta_\xi, \frac{\imath\xi}{2}\right\}$
r	-	$\left\{-\sin\theta_\xi, \cos\theta_\xi, \frac{3\imath}{4h}(k+3h)\xi\right\}$

where $A=\left(\frac{k}{a}\right)^2(\xi a)^4+2\frac{k}{a}\frac{h}{a}(\xi a)^2\left\{3(\xi a)^2-20\right\}+\left(\frac{h}{a}\right)^2\left\{400-40(\xi a)^2+9(\xi a)^4\right\}$, and m is the mass of a particle.

Similarly, solving Eq. 3.26, we can obtain following $\omega-\xi$ relations for the continuum from from second order Taylor approximation (CFSTE)

$$\omega^2=\begin{cases} \frac{3}{2m}(3k+h)(\xi a)^2 \\ \frac{3}{4m}\left\{(\xi a)^2 k+\left\{20-7(\xi a)^2\right\}h-a\sqrt{B}\right\} \\ \frac{3}{4m}\left\{(\xi a)^2 k+\left\{20-7(\xi a)^2\right\}h+a\sqrt{B}\right\} \end{cases} \tag{3.29}$$

where $B=\left(\frac{k}{a}\right)^2(\xi a)^4+2\frac{k}{a}\frac{h}{a}(\xi a)^2\left\{13-20(\xi a)^2\right\}+\left(\frac{h}{a}\right)^2\left\{400-360(\xi a)^2+169(\xi a)^4\right\}$.

As seen, it is predicted that the frequency, ω, does not depend on the direction of propagation,θ_ξ. The $\omega-\xi$ relations for continuum from from infinite Taylor series approach (CFITE) are too complicated and long to write. Instead, plots of $\omega-\xi$ relations are shown in section 3.4.

3.3.3 Wave speed estimation

From the above obtained $\omega-\xi$ it is straight forward to analytically estimate the wave speed, ω/ξ. Further, it is straight forward to find the mode shapes of each wave from the characteristic equations.. The corresponding wave speeds and the modes of each wave are given in Table 3.1. The first mode corresponds to primary wave (p-wave) since the movements are parallel to the direction of wave propagation. In the case of the second and third modes, the movements are perpendicular to the direction of wave propagation. As the translation is dominant for the second mode, this mode is considered to be secondary-wave (s-wave). Finally, the third mode represents rotational-wave (r-wave), because the rotation is dominant.

These analytical predictions have several advantages. As an example, these are useful in

- understanding dynamic characteristics of systems idealized as mass spring systems
- verification of numerical codes
- design purposes, as it will be shown in the next chapter
- etc.

3.4 Verification of the predictions made with continuum forms

Prior to any applications of the above derived analytical $\omega-\xi$ relations with the continuum forms (i.e. Eq. 3.28 and Eq. 3.29), it is essential to verify their accuracy and the range of applicability. To that end, in this section, we compare the predicted wave speeds given in Table 3.1 and the $\omega-\xi$ relations from Eq. 3.28 and Eq. 3.29 with those obtained from numerical simulations of a mass-spring system. To make it more precise, the comparison of $\omega-\xi$ relations is done in Fourier domain. On the otherhand, comparisons of wave speeds is relatively low in accuracy due to the simple technique used in estimating wave speeds.

3.4.1 Problem setting

A circular domain of radius 72m shown in Figure 3.5 is considered. The circular domain is filled with hexagonally packed spheres of radius a=0.1m and density ρ=1800kg/m^3. Spring constants, k and h, are 7×10^5 N/m and 3×10^5 N/m, respectively.

The center particle in the domain is excited with three different boundary conditions as shown in Figure 3.7. In cases (a) and (b), the center particle is excited in horizontal and vertical translations, while in case (c) it is excited with in-plane rotational motion. In all the cases, the profile of the excitation is set to be $f(t)$

$$f(t)=\frac{4}{3\sqrt{3}}A\left(\sin\frac{\hat{\omega}t}{2}-\frac{1}{2}\sin\hat{\omega}t\right), \tag{3.30}$$

where A is the amplitude of the input and $\hat{\omega}$ is input frequency. The amplitude,A, of translation and rotation are set to be 0.002m and 0.035rad, respectively (Figure 3.7). To obtain the wavelength 20 times longer than particle size but short enough to observe propagating waves, $\hat{\omega}$ is set to be 62.8 rad/s and 1088 rad/s for translation and rotation excitation, respectively.

3.4.2 Comparison of analytical and numerical wave speeds

Figure 3.8 shows the numerically simulated wavefronts at t=1s. For the sake of convenience the wave amplitudes are normalized dividing by the largest amplitude (i.e. u/u_{max}). In both horizontal and vertical excitations, shown in Figure 3.8, the p- and s-waves are clearly visible. The pair of closely located parallel semicircular narrow bands close to letter A and B are the p and s-waves. The semicircular wave fronts indicates that the hexagonnlly packed spherical mass-spring system is isotropic, which proves the analytical predictions.

P- and s-wave speed from numerical results are roughly estimated by measuring the distance traveled by a selected wave crest between t=0.2s and t=1.0s. Figure 4.7 and 3.10 show the p- and s-wave profiles used for speed estimations. According to this rough estimations, the numerically obtained p-and s-wave speeds are 69m/s and 45 m/s, respectively, while the analytically predicted speeds are 69 m/s and 45 m/s, to the nearest 1m accuracy. . It is seen that the numerical and analytical results are in good agreement.

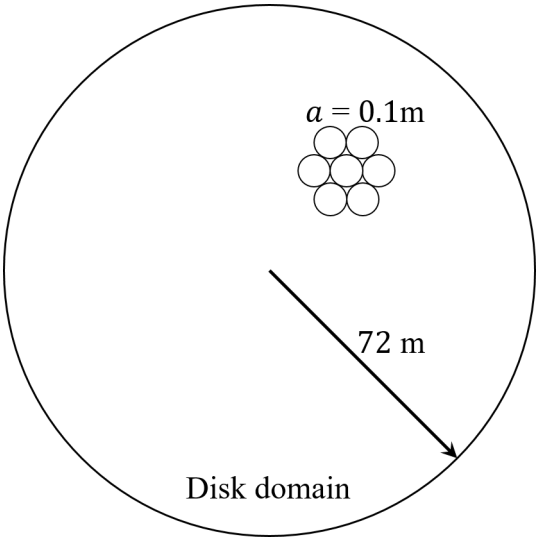

Figure 3.5: Domain setting.

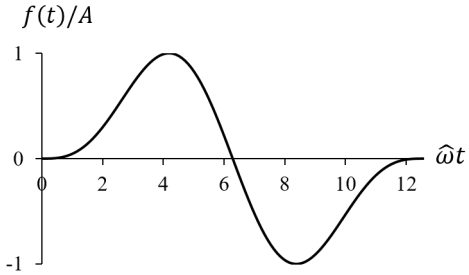

Figure 3.6: Input excitation function.

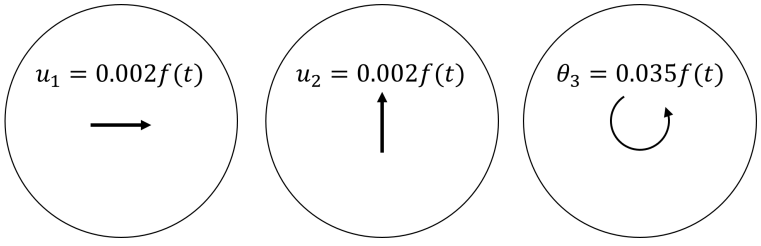

(a) horizontal excitation (b) verticle excitation (c) rotational excitation

Figure 3.7: Input boundary conditions

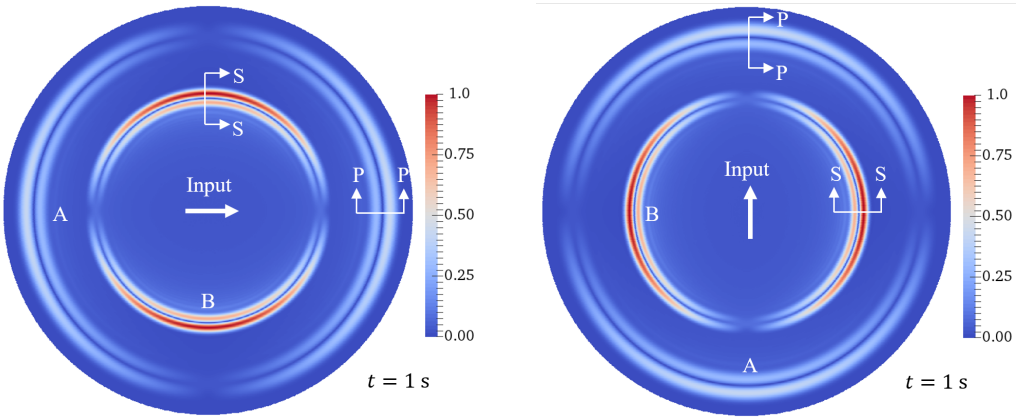

(a) horizontal excitation (b) verticle excitation

Figure 3.8: Wave field due to translational excitations at t=1s.

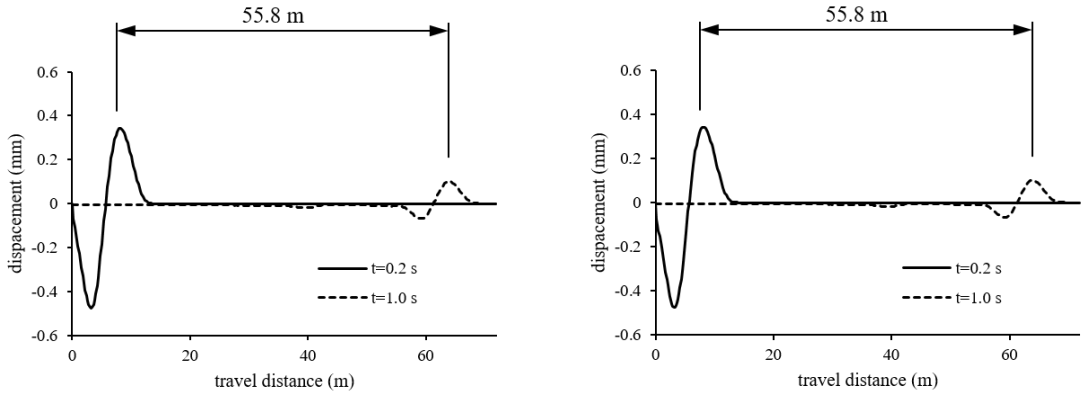

(a) horizontal excitation (b) verticle excitation

Figure 3.9: Cross sections along P-P of Figure 3.8 showing p-wave profiles at t=0.2s and t=1s .

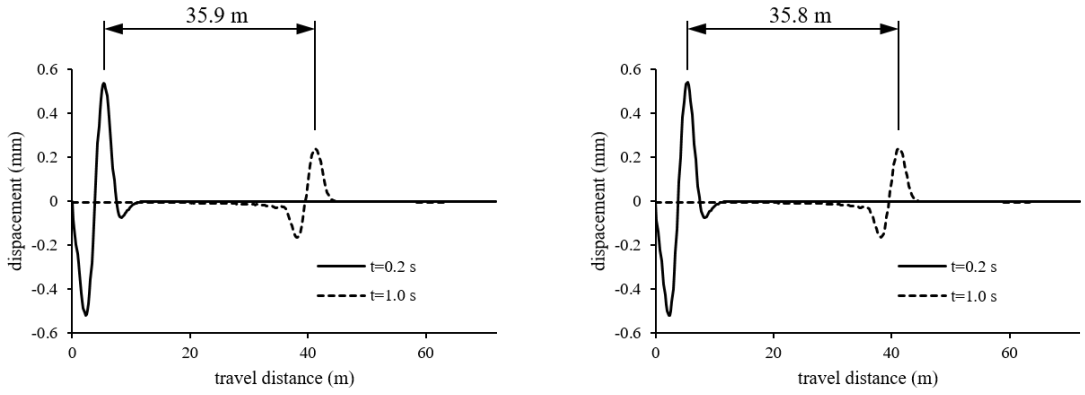

(a) horizontal excitation (b) verticle excitation

Figure 3.10: Cross sections along S-S of Figure 3.8 showing s-wave profiles at t=0.2s and t=1s .

3.4.3 Comparison of the relation between wave frequency and wave number

Figure 3.11 shows the numerically obtained r-wave field at $t=1$s; the wave field is normalized θ_3/θ_{max}. Unlike the p- and s-wave fields, the r-wave field is complicated, even thought the input wave is simple. Although isotropic behavior is predicted by continuumnization and the continuum model second order Taylor expansion, the hexagonal wave front indicates that the numerically obtained wave field is anisotrpoic. Though the outer most wave front is clearly hexagonal, it is nearly circular, indicating the analytical predictions can be considered sufficiently accurate for some engineering applications.

More precise measurement is taken to verify the results of rotational input. $\omega-\xi a$ relation from the numerical results are extracted taking Fast Fourier Transform (FFT) with respect to time and space, and compared with the analytical predictions. Specifically, the two slender domains shown with straight white lines in Figure 3.11 are considered for FFT analysis of normalized rotation obtained from numerical simulations.

Figure 3.12, 3.13, and 3.14 compare the analytically predicted $\omega-\xi a$ relations with those from numerical results. Note that the white areas indicate the amplitude above the scale. In these figures red and green line represent the analytical $\omega-\xi a$ relations for s-wave and r-wave based on continuumnization and the continuum form from second order and infinite Taylor expansions. Noted that the amplitude of p-waves are negligibly small in this simulation.

3.4.3.1 Prediction with continuumnization

According Figure 3.12, the analytical prediction of s-wave has a perfect match with the numerical results in the range $\xi a<0.6$ (or $\lambda>10a$), while they are in reasonable agreement even up to $\xi a=1.5$ (or $\lambda=4a$). However, the analytical and numerical $\omega-\xi$ relations for r-wave have a good agreement only within a small neighborhood of $\xi a=0$. This good agreement in s-wave but bad agreement in r-wave indicate that the predictions based on continuumnization is useful for the cases when translational wave is considered.

3.4.3.2 Prediction with continuum form based on second order Taylor expansion

As seen in Figure 3.12, the predictions based on the second order Taylor expansion has a better agreement for r-waves, compared to the above case. However, this reduce applicable range of s-wave. The s-waves are in good agreement in the range $0<\xi a<0.5$, while that of r-waves is $0<\xi a<0.6$. Outsize these regions, both the s- and r-wave predictions rapidly diverge form the numerical simulations. Compared to predictions with continuumnization, this model is suitable for most engineering applications since both s- and r-wave charanterristics can be accurately predicted in the range $\xi a<0.5$ or ($\lambda>13a$).

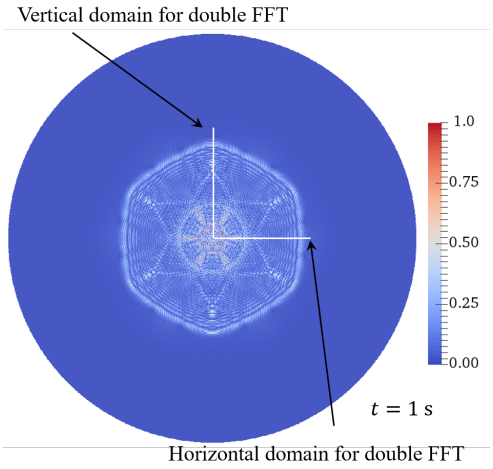

Figure 3.11: Normalized wave field at t=1s due to rotational input; θ_3/θ_{max} .

3.4.3.3 Prediction with continuum form based on infinite Taylor series

Surely, the analytical predictions with CFSTE is sufficient for most engineering applications. The motivation to derive the continuum form based on infinite Taylor series (CFIS) was our sheer curiosity to find an analytical form to predicting dynamic characteristics in much wider range. As seen in Figure 3.14, the numerical solution and CFIS predictions are in excellent match in the range $\xi a < 0.5\pi$ or $\lambda > 4a$, which is the shortest possible wavelength of the discrete particle systems. CFIS is a useful in scientific applications demanding higher accuracy even in short wavelengths, or verification of general RBSM codes. However, it is difficult to implement in FEM since continuum form contains trigonometric functions (Appendix C).

3.5 Summary

In this chapter, the concepts of continuumnization for spherical mass spring system for different approximation are explained. Based on the continuumnization, the 2d hexagonally packed spherical mass spring system are predicted as an isotropic system as frequency-wavenumber relations are independent of direction of wave propagation. The predicted dynamic characteristic are verified with numerical RBSM simulation.

For p-and s-waves, translational wave velocities are compared and shows that the numerical and predicted analytical wave velocities are in good agreement.

For r-wave, frequency-wavenumber relations for different continuuumnzation methods are verified using double fast Fourier transform with respect to length and time. As the results, Each method have show advantage and disadvantaged.

Original continuumnization (OC) provides a fairly good applicable range for s-wave. However, it is not applicable to verify r-wave. This is suitable for simulation which rotational wave is not considerd

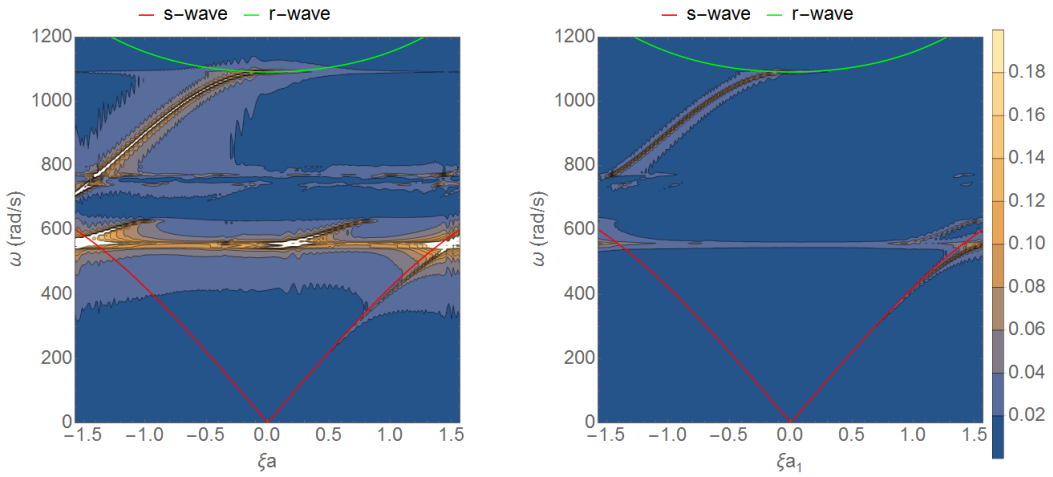

(a) Along the vertical domain (b) Along the horizontal domain

Figure 3.12: Comparison of numerical results and the analytical predictions with continnumnization . Contour plots show the numerically obtained amplitude of ω vs. ξa relation. The curved lines show the analytical prediction for s- and rotational waves

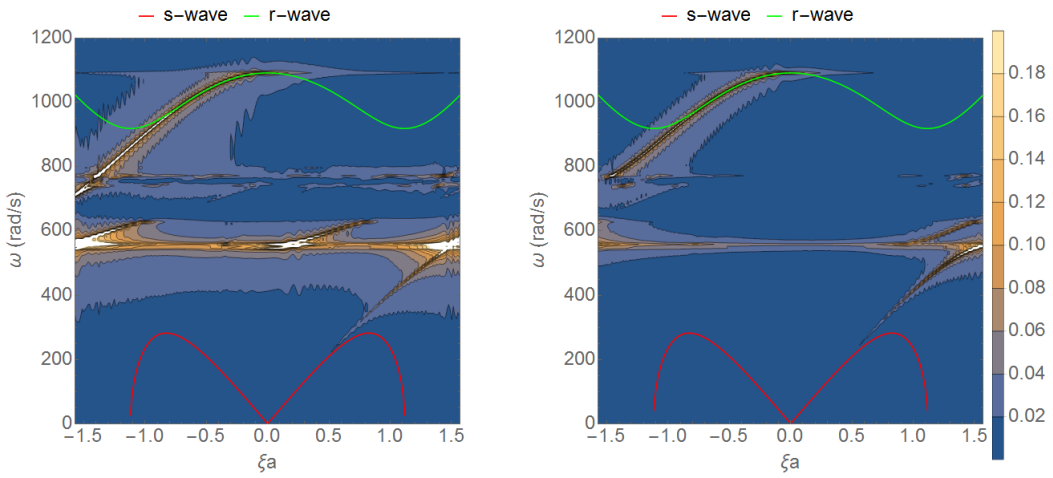

(a) Along the vertical domain (b) Along the horizontal domain

Figure 3.13: Comparison of numerical results and the analytical predictions with the continnum model based on second order Taylor expansion (CFSTE). . Contour plots show the numerically obtained amplitude of ω vs. ξa_i relation. The curved lines show the analytical prediction for p-, s- and rotational waves.

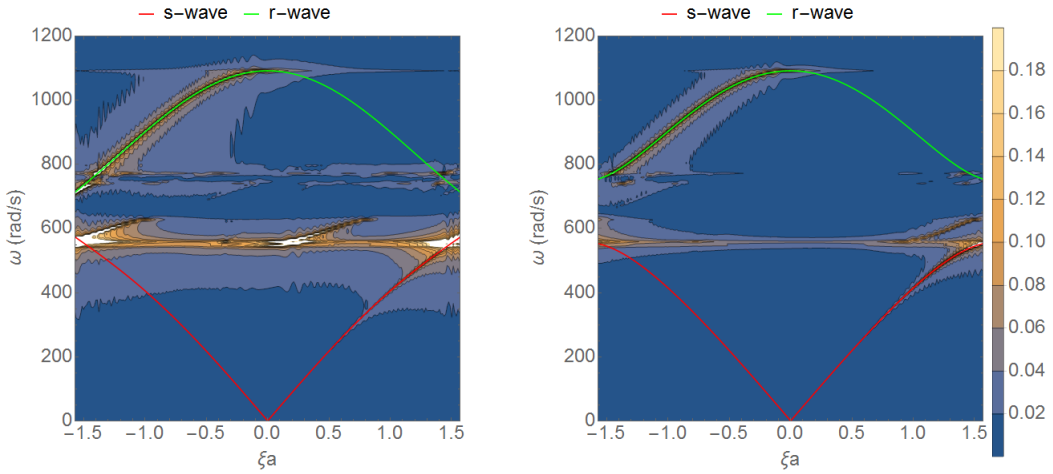

(a) Along the vertical domain

(b) Along the horizontal domain

Figure 3.14: Comparison of numerical results and the analytical predictions with the continuum form based on the infinite Taylor series expansion (CFIS). Contour plots show the numerically obtained amplitude of ω vs. ξa_i relation. The curved lines show the analytical prediction for p-, s- and rotational waves

Second order Taylor's expansion (CFSTE) provides a fairly good applicable range for s-wave and r-wave. The range of applicable is where the wavelength is 13 time longer than the radius of particle which is useful for typical discrete simulations

Infinite series (CFIS) shows the widest range of applicable for verification propose. This verification tool is useful for some scientific fields which relatively short wavelength compared to particle size appears However, it is difficult to construct numerical model since it contents sine and cosine terms.

Chapter 4

Continuumn forms of brick mass-spring systems

In this chapter, three equivalent continuum forms for brick mortar systems are developed following the similar steps of spherical particles presented in section 3.2. These continuum forms have two major practical applications; analytically predict the dynamic characteristics of the discrete system, and make it possible to use numerical tools of continuum mechanics like FEM to analyses brick mortar systems. The analytical predictions can be used to verify numerical simulations of brick mortar systems, find rational elastic properties based on dynamic experiments like sonic or ultrasonic test, and rationally choose brick-mortar properties for desired dynamic characteristics in structural designs.

The first half presents the formulations of continuumnization and CFSTE and CFIFT and predictions of wave characteristics. In the latter half, these predicted wave characteristics are verified comparing with numerical results.

4.1 Equations of motion of idealized brick mortar system

We idealize a regularly arranged brick-mortar system as a network of rigid rectangular blocks, with mass m and size of $2a_1 \times 2a_2 \times 2a_3$, connected with elastic springs at the interfaces (Figure 4.1 shows a 2D example). In the idealized model, the domain is completely tessellated with rectangular blocks such that each block includes the space occupied by a brick and portion of the space occupied by mortar layer. The elastic springs represent elasticity of both the bricks and cement layers, and we restrict our models to linear elastic springs; it is straight forward to extend to nonlinear elastic springs. This idealized model is a reasonable representation of brick mortar systems consists of bricks with higher rigidity compared to that of mortar.

As shown in Figure 4.1, the pair of neighbors in γ^{th}-direction are denoted by $\gamma+$ and $\gamma-$. $\boldsymbol{r}^{\gamma+}$ denotes the relative position of the centroid of the contact area with the neighbor γ. The tangential and shear spring constants per unit area are set to be k and h, respectively. When there is no confusion, we omit $\pm$ and use γ to denote any neighboring block.

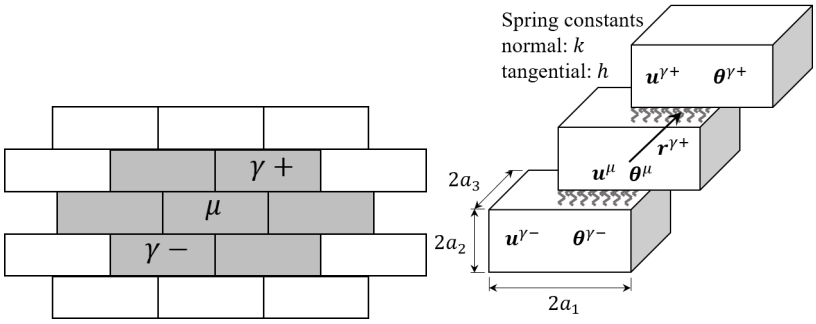

Figure 4.1: Idealized 2D block-spring model.

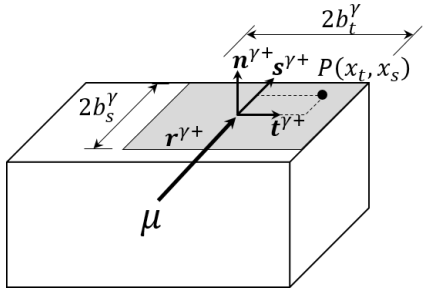

Figure 4.2: Contact surface.

4.1.1 Lagrangian of the idealized block-spring system

Let $\boldsymbol{u}^{\mu}$ and $\boldsymbol{\theta}^{\mu}$ denote three dimensional translation and rotation of μ^{th} block. The contact area is assumed to be of size $2b_t^{\gamma}\times 2b_s^{\gamma}$ (see Figure 4.2)., and unit vectors $\boldsymbol{n}^{\gamma}$, $\boldsymbol{t}^{\gamma}$, and $\boldsymbol{s}^{\gamma}$ denote the orthonormal coordinate systems on contact surfaces with any neighboring block γ as shown in Figure4.1. For given set of infinitesimal displacements and rotations, the relative displacement $\boldsymbol{L}^{\mu\gamma+}$ at the a point (x_t,x_s) on the contact surface with the neighbor $\gamma+$ can be expressed as

$$\boldsymbol{L}^{\mu\gamma+}(x_t,x_s) \;=\; \big(\boldsymbol{u}^{\gamma+}-\boldsymbol{u}^{\mu}\big)-\big(\boldsymbol{\theta}^{\gamma+}+\boldsymbol{\theta}^{\mu}\big)\times\boldsymbol{r}^{\gamma+}+\big(\boldsymbol{\theta}^{\gamma+}-\boldsymbol{\theta}^{\mu}\big)\times\big(x_t\boldsymbol{t}^{\gamma+}+x_s\boldsymbol{s}^{\gamma+}\big). \tag{4.1}$$

Here, the origin of (x_t,x_s) is located at the centroid of the contact area. The corresponding total elastic energy contribution from the contact surface is

$$V^{\mu\gamma+} \;=\; \frac{1}{2}\int_{-b_s^{\gamma}}^{b_s^{\gamma}}\int_{-b_t^{\gamma}}^{b_t^{\gamma}} k\big(\boldsymbol{n}^{\gamma+}\cdot\boldsymbol{L}^{\mu\gamma+}\big)^2+h\Big\{\big(t^{\gamma+}\cdot\boldsymbol{L}^{\mu\gamma+}\big)^2+\big(\boldsymbol{s}^{\gamma+}\cdot\boldsymbol{L}^{\mu\gamma+}\big)^2\Big\}\mathrm{d}x_t\mathrm{d}x_s. \tag{4.2}$$

Similarly, the elastic energy $V^{\mu\gamma-}$ can be obtained using $-\boldsymbol{n}^{\gamma}$, $-\boldsymbol{t}^{\gamma}$**,** $\boldsymbol{s}^{\gamma}$**,** $-\boldsymbol{r}^{\gamma}$**.** The Lagrangian for the whole discrete system is

$$\mathcal{L} = \sum_{\mu}\left(\frac{1}{2}m\dot{\boldsymbol{u}}^{\mu}\cdot\dot{\boldsymbol{u}}^{\mu}+\frac{1}{2}\dot{\boldsymbol{\theta}}^{\mu}\cdot\boldsymbol{I}\cdot\dot{\boldsymbol{\theta}}^{\mu}-V^{\mu}\right), \tag{4.3}$$

where $V^{\mu}=\sum_{\gamma}\frac{1}{2}(V^{\mu\gamma+}+V^{\mu\gamma-})$, and $\boldsymbol{I}$ is the inertia tensor of a block.

4.1.2 Governing equations for the discrete system

According to the Hamilton's principle , the discrete governing equations of block spring system is given by

$$\begin{aligned}
\int_{t_1}^{t_2}\delta\mathcal{L}\mathrm{d}t &= 0\\
0 &= -\sum_{\mu}\int_{t_1}^{t_2}(m\ddot{\boldsymbol{u}}^{\mu}\cdot\delta\boldsymbol{u}^{\mu}+\ddot{\boldsymbol{\theta}}^{\mu}\cdot\boldsymbol{I}\cdot\delta\boldsymbol{\theta}^{\mu})\mathrm{d}t\\
&\quad -\sum_{\mu}\sum_{\gamma}\int_{t_1}^{t_2}\Big\{-\boldsymbol{K}^{\gamma}:\big(\boldsymbol{u}^{\gamma+}-2\boldsymbol{u}^{\mu}+\boldsymbol{u}^{\gamma-}\big)\otimes\delta\boldsymbol{u}^{\mu}+\hat{\boldsymbol{K}}^{\gamma}:\big(\boldsymbol{\theta}^{\gamma+}-\boldsymbol{\theta}^{\gamma-}\big)\otimes\delta\boldsymbol{u}^{\mu}\\
&\quad -\Big(\hat{\boldsymbol{K}}^{\gamma}\Big)^{T}:\big(\boldsymbol{u}^{\gamma+}-\boldsymbol{u}^{\gamma-}\big)\otimes\delta\boldsymbol{\theta}^{\mu}+\bar{\boldsymbol{K}}^{\gamma}:\big(\boldsymbol{\theta}^{\gamma+}+2\boldsymbol{\theta}^{\mu}+\boldsymbol{\theta}^{\gamma-}\big)\otimes\delta\boldsymbol{\theta}^{\mu}\\
&\quad -\bar{\bar{\boldsymbol{K}}}^{\gamma}:\big(\boldsymbol{\theta}^{\gamma+}-2\boldsymbol{\theta}^{\mu}+\boldsymbol{\theta}^{\gamma-}\big)\otimes\delta\boldsymbol{\theta}^{\mu}\Big\}\mathrm{d}t
\end{aligned} \tag{4.4}$$

where

$$\begin{aligned}
\boldsymbol{K}^{\gamma} &= 4b_t^{\gamma}b_s^{\gamma}\big(k\boldsymbol{n}^{\gamma+}\otimes\boldsymbol{n}^{\gamma+}+h\boldsymbol{t}^{\gamma+}\otimes\boldsymbol{t}^{\gamma+}+h\boldsymbol{s}^{\gamma+}\otimes\boldsymbol{s}^{\gamma+}\big)\\
\hat{\boldsymbol{K}}^{\gamma} &= 4b_t^{\gamma}b_s^{\gamma}\big\{k\boldsymbol{n}^{\gamma+}\otimes\big(\boldsymbol{r}^{\gamma+}\times\boldsymbol{n}^{\gamma+}\big)+h\boldsymbol{t}^{\gamma+}\otimes\big(\boldsymbol{r}^{\gamma+}\times\boldsymbol{t}^{\gamma+}\big)+h\boldsymbol{s}^{\gamma+}\otimes\big(\boldsymbol{r}^{\gamma+}\times\boldsymbol{s}^{\gamma+}\big)\big\}\\
\overline{\boldsymbol{K}}^{\gamma} &= 4b_t^{\gamma}b_s^{\gamma}\big\{k\big(\boldsymbol{r}^{\gamma+}\times\boldsymbol{n}^{\gamma+}\big)\otimes\big(\boldsymbol{r}^{\gamma+}\times\boldsymbol{n}^{\gamma+}\big)+h\big(\boldsymbol{r}^{\gamma+}\times\boldsymbol{t}^{\gamma+}\big)\otimes\big(\boldsymbol{r}^{\gamma+}\times\boldsymbol{t}^{\gamma+}\big)\\
&\quad +h\big(\boldsymbol{r}^{\gamma+}\times\boldsymbol{s}^{\gamma+}\big)\otimes\big(\boldsymbol{r}^{\gamma+}\times\boldsymbol{s}^{\gamma+}\big)\big\}\\
\overline{\bar{\boldsymbol{K}}}^{\gamma} &= 4\frac{b_t^{\gamma}b_s^{\gamma}}{3}\big\{h\big(b_s^{\gamma 2}+b_t^{\gamma 2}\big)\boldsymbol{n}^{\gamma+}\otimes\boldsymbol{n}^{\gamma+}+kb_s^{\gamma 2}\boldsymbol{t}^{\gamma+}\otimes\boldsymbol{t}^{\gamma+}+kb_t^{\gamma 2}\boldsymbol{s}^{\gamma+}\otimes\boldsymbol{s}^{\gamma+}\big\}
\end{aligned} \tag{4.5}$$

Since $\int_{t_1}^{t_2}\delta\mathcal{L}\mathrm{d}t=0$ should hold for arbitrary $\delta\boldsymbol{u}^{\mu}$ and $\delta\boldsymbol{\theta}^{\mu}$, which are admissible variations of $\boldsymbol{u}^{\mu}$ and $\boldsymbol{\theta}^{\mu}$, Eq. 4.4 holds when

$$\begin{aligned}
m\ddot{\boldsymbol{u}}^{\mu} &= \sum_{\gamma}\Big\{\boldsymbol{K}^{\gamma}\cdot\big(\boldsymbol{u}^{\gamma+}-2\boldsymbol{u}^{\mu}+\boldsymbol{u}^{\gamma-}\big)-\hat{\boldsymbol{K}}^{\gamma}\cdot\big(\boldsymbol{\theta}^{\gamma+}-\boldsymbol{\theta}^{\gamma-}\big)\Big\}\\
\boldsymbol{I}\cdot\ddot{\boldsymbol{\theta}}^{\mu} &= \sum_{\gamma}\Big\{\Big(\hat{\boldsymbol{K}}^{\gamma}\Big)^{\mathrm{T}}\cdot\big(\boldsymbol{u}^{\gamma+}-\boldsymbol{u}^{\gamma-}\big)-\overline{\boldsymbol{K}}^{\gamma}\cdot\big(\boldsymbol{\theta}^{\gamma+}+2\boldsymbol{\theta}^{\mu}+\boldsymbol{\theta}^{\gamma-}\big)+\overline{\overline{\boldsymbol{K}}}^{\gamma}\cdot\big(\boldsymbol{\theta}^{\gamma+}-2\boldsymbol{\theta}^{\mu}+\boldsymbol{\theta}^{\gamma-}\big)\Big\}
\end{aligned} \tag{4.6}$$

The above set is the equation of motions for idealized brick mortar system. Like the governing equation of the spherical systems, $\hat{\boldsymbol{K}}^{\gamma}$ couples translations and rotations. The above obtained equations of motion for the discrete system can be used to simulate a brick structure as a mass spring system, in which the $\boldsymbol{K}^{\gamma}$,$\hat{\boldsymbol{K}}^{\gamma}$, $\overline{\boldsymbol{K}}^{\gamma}$, and, $\overline{\overline{\boldsymbol{K}}}^{\gamma}$ are determined in Eq. 4.5 by given brick arrangement, geometry, and spring constants.

4.2 Equivalent continuum forms

As we did with the mass spring system in section 3.2, we obtain two equivalent continuum forms for the idealized brick-mortar system; continnumnization and CFSTE. Just as in section 3.2, we assume that there exists two vector fields $\boldsymbol{u}(\boldsymbol{x})$ and $\boldsymbol{\theta}(\boldsymbol{x})$ which satisfy $\boldsymbol{u}(\boldsymbol{x}^{\mu})=\boldsymbol{u}^{\mu}$ and $\boldsymbol{\theta}(\boldsymbol{x}^{\mu})=\boldsymbol{\theta}^{\mu}$ in deriving equivalent continuum forms. As mentioned at the beginning of this chapter, these continuum forms have multiple advantages; analytical prediction of dynamic characteristics, application of numerical tools in continuum mechanics, etc.

4.2.1 Continuumnization

As presented in the section 3.2.1, continuumnization assumes the blocks are negligibly small small compared to the dimensions of the considered domain or the wave lengths of interest, and idealizes the particle system as a continuum considering the limit of particle size going to zero. With this assumption, continuumnization approximates relative discrete displacement gradients of discrete vector field as a directional derivative of a continuous vector field. As an example, we can make the following approximations where $2\boldsymbol{r}^{\gamma\pm}$ is the relative positions of neighbor $\gamma\pm$ of brick μ.

$$\begin{aligned}\lim_{a\longrightarrow 0}\frac{\boldsymbol{u}^{\gamma\pm}-\boldsymbol{u}^{\mu}}{2r^{\gamma+}} &\approx \pm\hat{\boldsymbol{r}}^{\gamma+}\cdot\nabla\boldsymbol{u} &(4.7)\\ \lim_{a\longrightarrow 0}\frac{\boldsymbol{u}^{\gamma+}-2\boldsymbol{u}^{\mu}+\boldsymbol{u}^{\gamma-}}{4r^{\gamma+}} &\approx \hat{\boldsymbol{r}}^{\gamma+}\cdot\nabla\left(\boldsymbol{n}^{\gamma+}\cdot\nabla\boldsymbol{u}\right) &(4.8)\end{aligned}$$

Here, $r^{\gamma+}$ and $\hat{\boldsymbol{r}}^{\gamma+}$ are the magnitude and corresponding unit vector of $\boldsymbol{r}^{\gamma+}$, respectively. Based on the above approximations, the relative rotation and translation are approximated as

$$\begin{aligned}\boldsymbol{u}^{\gamma+}-2\boldsymbol{u}^{\mu}+\boldsymbol{u}^{\gamma-} &\approx 4\boldsymbol{r}^{\gamma+}\cdot\nabla\left(\boldsymbol{r}^{\gamma+}\cdot\nabla\boldsymbol{u}\right)\\ \boldsymbol{u}^{\gamma+}-\boldsymbol{u}^{\gamma-} &\approx 4\boldsymbol{r}^{\gamma+}\cdot\nabla\boldsymbol{u}\\ \boldsymbol{\theta}^{\gamma+}+2\boldsymbol{\theta}^{\mu}+\boldsymbol{\theta}^{\gamma-} &\approx 4\boldsymbol{\theta} &(4.9)\end{aligned}$$

Substituting the above approximated relative translation and rotation in to Eq. 4.6, the following continuum forms of governing equations can be obtained

$$\begin{aligned}\frac{m}{V_{\rm b}}\ddot{\boldsymbol{u}} &= \nabla\cdot(\boldsymbol{c}:\nabla\boldsymbol{u})-\boldsymbol{q}:\nabla\boldsymbol{\theta}\\ \frac{1}{V_{\rm b}}\boldsymbol{I}\cdot\ddot{\boldsymbol{\theta}} &= \boldsymbol{q}^{\rm T}:\nabla\boldsymbol{u}-\boldsymbol{d}\cdot\boldsymbol{\theta},\end{aligned} \tag{4.10}$$

where

$$\begin{aligned}\boldsymbol{c} &= \sum_{\gamma}\frac{16b_t^{\gamma}b_s^{\gamma}}{V_{\rm b}}\left(k\boldsymbol{r}^{\gamma+}\otimes\boldsymbol{n}^{\gamma}\otimes\boldsymbol{r}^{\gamma+}\otimes\boldsymbol{n}^{\gamma}+h\boldsymbol{r}^{\gamma+}\otimes\boldsymbol{t}^{\gamma+}\otimes\boldsymbol{r}^{\gamma+}\otimes\boldsymbol{t}^{\gamma+}+h\boldsymbol{r}^{\gamma+}\otimes\boldsymbol{s}^{\gamma+}\otimes\boldsymbol{r}^{\gamma+}\otimes\boldsymbol{s}^{\gamma+}\right)\\ \boldsymbol{q} &= \sum_{\gamma}\frac{16b_t^{\gamma}b_s^{\gamma}}{V_{\rm b}}\left\{k\boldsymbol{n}^{\gamma}\otimes\boldsymbol{r}^{\gamma+}\otimes\left(\boldsymbol{r}^{\gamma+}\times\boldsymbol{n}^{\gamma}\right)+h\boldsymbol{t}^{\gamma+}\otimes\boldsymbol{r}^{\gamma+}\otimes\left(\boldsymbol{r}^{\gamma+}\times\boldsymbol{t}^{\gamma+}\right)\right.\\ &\quad\left.+h\boldsymbol{s}^{\gamma+}\otimes\boldsymbol{r}^{\gamma+}\otimes\left(\boldsymbol{r}^{\gamma+}\times\boldsymbol{s}^{\gamma+}\right)\right\}\\ \boldsymbol{d} &= \sum_{\gamma}\frac{16b_t^{\gamma}b_s^{\gamma}}{V_{\rm b}}\left\{k\left(\boldsymbol{r}^{\gamma+}\times\boldsymbol{n}^{\gamma}\right)\otimes\left(\boldsymbol{r}^{\gamma+}\times\boldsymbol{n}^{\gamma}\right)+h\left(\boldsymbol{r}^{\gamma+}\times\boldsymbol{t}^{\gamma+}\right)\otimes\left(\boldsymbol{r}^{\gamma+}\times\boldsymbol{t}^{\gamma+}\right)\right.\\ &\quad\left.+h\left(\boldsymbol{r}^{\gamma+}\times\boldsymbol{s}^{\gamma+}\right)\otimes\left(\boldsymbol{r}^{\gamma+}\times\boldsymbol{s}^{\gamma+}\right)\right\},\end{aligned} \tag{4.11}$$

and $V_{\rm b}$ is the volume of a block.

4.2.2 Continuum form based on second order Taylor expansion (CFSTE)

In developing continuum forms based on Taylor expansion, it is assumed that there exists sufficiently smooth vector fields $\boldsymbol{u}(\boldsymbol{x},t)$ and $\boldsymbol{\theta}(\boldsymbol{x},t)$ which can approximate the discrete fields $\boldsymbol{u}^{\mu}$ and $\boldsymbol{\theta}^{\mu}$ for a sufficiently large wave lengths. Under this assumption, the translation of neighbor $\boldsymbol{u}^{\gamma\pm}$ = $\boldsymbol{u}(\boldsymbol{x}\pm\boldsymbol{r},t)$ and we can approximate $\boldsymbol{u}(\boldsymbol{x}\pm\boldsymbol{r},t)$ using Taylor series expansion as

$$\begin{aligned}u(\boldsymbol{x}+2\boldsymbol{r}^{\gamma+}) &= u(\boldsymbol{x})+2\frac{\partial u(\boldsymbol{x})}{\partial x_i}r_i^{\gamma+}+\frac{2^2}{2!}\frac{\partial^2 u(\boldsymbol{x})}{\partial x_i\partial x_j}r_i^{\gamma+}r_j^{\gamma+}+\ldots\\ u(\boldsymbol{x}-2\boldsymbol{r}^{\gamma+}) &= u(\boldsymbol{x})-2\frac{\partial u(\boldsymbol{x})}{\partial x_i}r_i^{\gamma+}+\frac{2^2}{2!}\frac{\partial^2 u(\boldsymbol{x})}{\partial x_i\partial x_j}r_i^{\gamma+}r_j^{\gamma+}-\ldots\end{aligned}$$

Addition and subtraction of the above two provide

$$u(\boldsymbol{x}+2\boldsymbol{r}^{\gamma+})+u(\boldsymbol{x}-2\boldsymbol{r}^{\gamma+}) = 2\left\{u(\boldsymbol{x})+\frac{2^2}{2!}\frac{\partial^2 u(\boldsymbol{x})}{\partial x_i\partial x_j}r_i^{\gamma+}r_j^{\gamma+}+\ldots\right\} \tag{4.12}$$

$$u(\boldsymbol{x}+2\boldsymbol{r}^{\gamma+})-u(\boldsymbol{x}-2\boldsymbol{r}^{\gamma+}) = 2\left\{2\frac{\partial u(\boldsymbol{x})}{\partial x_i}r_i^{\gamma+}+\frac{2^3}{3!}\frac{\partial^3 u(\boldsymbol{x})}{\partial x_i\partial x_j\partial x_k}r_i^{\gamma+}r_j^{\gamma+}r_k^{\gamma+}+\ldots\right\}. \tag{4.13}$$

In developing a second order continuum form, we assume that the vector fields $\boldsymbol{u}(\boldsymbol{x},t)$ and $\boldsymbol{\theta}(\boldsymbol{x},t)$ to be at least twice differentiable and obtain the following second order approximations based on the above Taylor series expansions.

$$
\begin{aligned}
u_i^+ - 2u_i + u_i^- &\approx 4\frac{\partial^2 u_i(\boldsymbol{x})}{\partial x_j \partial x_k} r_j^{\gamma+} r_k^{\gamma+} && (4.14)\\
u_i^+ - u_i^- &\approx 4\frac{\partial u_i(\boldsymbol{x})}{\partial x_j} r_j^{\gamma+} && (4.15)\\
\theta_i^+ - \theta_i^- &\approx 4\frac{\partial \theta_i(\boldsymbol{x})}{\partial x_j} r_j^{\gamma+} && (4.16)\\
\theta_i^+ - 2\theta_i + \theta_i^- &\approx 4\frac{\partial^2 \theta_i(\boldsymbol{x})}{\partial x_j \partial x_k} r_j^{\gamma+} r_k^{\gamma+} && (4.17)\\
\theta_i^+ + 2\theta_i + \theta_i^- &\approx 4\theta_i + 4\frac{\partial^2 \theta_i(\boldsymbol{x})}{\partial x_j \partial x_k} r_j^{\gamma+} r_k^{\gamma+}. && (4.18)
\end{aligned}
$$

Substituting the above second order approximations to Eq. 4.6 , we can obtain the following second order continuum form of governing equations.

$$
\begin{aligned}
\frac{m}{V_{\mathrm{b}}}\ddot{\boldsymbol{u}} &= \nabla\cdot(\boldsymbol{c}:\nabla\boldsymbol{u}) - \boldsymbol{q}:\nabla\boldsymbol{\theta}\\
\frac{1}{V_{\mathrm{b}}}\boldsymbol{I}\cdot\ddot{\boldsymbol{\theta}} &= \boldsymbol{q}^{\mathrm{T}}:\nabla\boldsymbol{u} - \boldsymbol{d}\cdot\boldsymbol{\theta} + \nabla\cdot(\boldsymbol{v}:\nabla\boldsymbol{\theta}), && (4.19)
\end{aligned}
$$

where $\boldsymbol{v}$ is the following 4^{th}-order tensor introduced by the the additional second order term of $\boldsymbol{\theta}$.

$$
\begin{aligned}
\boldsymbol{v} = \sum_{\gamma} & \frac{16}{V_{\mathrm{b}}}\frac{b_t^\gamma b_s^\gamma}{3}\Big\{h\left((b_s^\gamma)^2 + (b_t^\gamma)^2\right)\boldsymbol{r}^{\gamma+}\otimes\boldsymbol{n}^\gamma\otimes\boldsymbol{r}^{\gamma+}\otimes\boldsymbol{n}^\gamma\\
&+k(b_s^\gamma)^2\boldsymbol{r}^{\gamma+}\otimes\boldsymbol{t}^{\gamma+}\otimes\boldsymbol{r}^{\gamma+}\otimes\boldsymbol{t}^{\gamma+} + k(b_t^\gamma)^2\boldsymbol{r}^{\gamma+}\otimes\boldsymbol{s}^{\gamma+}\otimes\boldsymbol{r}^{\gamma+}\otimes\boldsymbol{s}^{\gamma+}\Big\}\\
&-\frac{16 b_t^\gamma b_s^\gamma}{V_{\mathrm{b}}}\Big\{k\boldsymbol{r}^{\gamma+}\otimes\left(\boldsymbol{r}^{\gamma+}\times\boldsymbol{n}^{\gamma+}\right)\otimes\boldsymbol{r}^{\gamma+}\otimes\left(\boldsymbol{r}^{\gamma+}\times\boldsymbol{n}^{\gamma}\right)\\
&+h\boldsymbol{r}^{\gamma+}\otimes\left(\boldsymbol{r}^{\gamma+}\times\boldsymbol{t}^{\gamma+}\right)\otimes\boldsymbol{r}^{\gamma+}\otimes\left(\boldsymbol{r}^{\gamma+}\times\boldsymbol{t}^{\gamma+}\right)\\
&+h\boldsymbol{r}^{\gamma+}\otimes\left(\boldsymbol{r}^{\gamma+}\times\boldsymbol{s}^{\gamma+}\right)\otimes\boldsymbol{r}^{\gamma+}\otimes\left(\boldsymbol{r}^{\gamma+}\times\boldsymbol{s}^{\gamma+}\right)\Big\}. \qquad (4.20)
\end{aligned}
$$

The constants $\boldsymbol{c}$, $\boldsymbol{q}$, $\boldsymbol{d}$, and $\boldsymbol{v}$ are 4^{th}, 3^{rd}, 2^{nd}, and 4^{th}-order tensors comprise of material and geometric (i.e. block geometry and packing) properties.

4.3 Analytical solution to the characteristic equation in 2D

With the aim of predicting the dynamic characteristics of the idealized brick mortar system, we analyze the characteristic equations of the above obtained two continuum forms. All the above derived equations are valid for 3D regular packing. For the sake on simplicity, we restrict our discussion to 2D brick walls with the brick arrangement shown in Figure 4.3.

4.3.1 Characteristic equations of continuum forms

Evaluating the four tensors $\boldsymbol{c}$, $\boldsymbol{q}$, $\boldsymbol{d}$, and $\boldsymbol{v}$ for the 2D packing shown in Figure4.3and taking Fourier transform with the kernel $e^{\imath(\boldsymbol{\xi}\cdot\boldsymbol{x}-\omega t)}$, we can obtain the characteristic equations for each continuum form. As we did in section 3.3, we express the vector $\boldsymbol{\xi}$ as $\boldsymbol{\xi}=\xi\{\cos\theta_\xi,\sin\theta_\xi\}$, where ξ is the magnitude of the wave number (i.e. $\xi=\frac{2\pi}{\lambda}$ where λ is the wave length) and θ_ξ is the direction of the wave propagation as shown in Figure 4.3.

For continuumnization, , characteristic equation is

$$\det\begin{bmatrix} A_{11}-\frac{m}{V_\mathrm{b}}\omega^2 & 0 & -2\imath a_2 h\xi\sin\theta_\xi \\ 0 & A_{22}-\frac{m}{V_\mathrm{b}}\omega^2 & \frac{a_1\imath}{2}\left(4h+\frac{a_1 k}{a_2}\right)\xi\cos\theta_\xi \\ 2\imath a_2 h\xi\sin\theta_\xi & -\frac{a_1\imath}{2}\left(4h+\frac{a_1 k}{a_2}\right)\xi\cos\theta_\xi & A_{33}-\frac{I_{33}}{V_\mathrm{b}}\omega^2 \end{bmatrix} = 0$$

where

$$\begin{aligned} A_{11} &= \frac{a_1}{2}\left(\frac{a_1 h}{a_2}+4k\right)\xi^2\cos^2\theta_\xi+2a_2 h\xi^2\sin^2\theta_\xi \\ A_{22} &= \frac{a_1}{2}\left(4h+\frac{a_1 k}{a_2}\right)\xi^2\cos^2\theta_\xi+2a_2 k\xi^2\sin^2\theta_\xi \\ A_{33} &= 2a_1 h+2a_2 h+\frac{a_1^2}{2a_2}k+\frac{a_1(a_1^3+16a_2^3)k}{24a_2}\xi^2\cos^2\theta_\xi-\frac{a_1^2 a_2}{6}k\xi^2\sin^2\theta_\xi \end{aligned}$$

For CFSTE, characteristic equation is

$$\det\begin{bmatrix} A_{11}-\frac{m}{V_\mathrm{b}}\omega^2 & 0 & -2\imath a_2 h\xi\sin\theta_\xi \\ 0 & A_{22}-\frac{m}{V_\mathrm{b}}\omega^2 & \frac{a_1\imath}{2}\left(4h+\frac{a_1 k}{a_2}\right)\xi\cos\theta_\xi \\ 2\imath a_2 h\xi\sin\theta_\xi & -\frac{a_1\imath}{2}\left(4h+\frac{a_1 k}{a_2}\right)\xi\cos\theta_\xi & A_{33}-\frac{I_{33}}{V_\mathrm{b}}\omega^2 \end{bmatrix} = 0$$

where

$$
\begin{aligned}
A_{11} &= \frac{a_1}{2}\left(\frac{a_1 h}{a_2}+4k\right)\xi^2\cos^2\theta_\xi+2a_2 h\xi^2\sin^2\theta_\xi \\
A_{22} &= \frac{a_1}{2}\left(4h+\frac{a_1 k}{a_2}\right)\xi^2\cos^2\theta_\xi+2a_2 k\xi^2\sin^2\theta_\xi \\
A_{33} &= 2a_1 h+2a_2 h+\frac{a_1^2}{2a_2}k+\left\{\frac{a_1(a_1^3+16a_2^3)k}{24a_2}-\frac{1}{8}a_1^2\left(16a_1 h+4a_2 h+\frac{a_1^2 k}{a_2}\right)\right\}\xi^2\cos^2\theta_\xi \\
&\quad +(-2a_2^3 h-\frac{a_1^2 a_2}{3}k)\xi^2\sin^2\theta_\xi.
\end{aligned}
$$

Solving these characteristic equations, the relations between the wave frequencies and wave number (i.e. $\omega-\xi$ relation) can be obtained. The obtained $\omega-\xi$ relation are not included in this thesis due to space limitations.

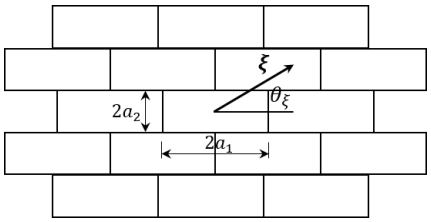

Figure 4.3: A single layered 2 dimensional brick arrangement.

4.3.2 Characteristic equations based on infinite Taylor series

With a little bit of mathematical manipulations, the following two relations for the Fourier transform of Eq. 4.12 and Eq. 4.13 can be established.

$$
\begin{aligned}
\int \left(\boldsymbol{u}^{\gamma+}+\boldsymbol{u}^{\gamma-}\right)e^{\imath(\boldsymbol{\xi}\cdot\boldsymbol{x}-\omega t)}\mathrm{d}\boldsymbol{x}\mathrm{d}t &\approx 2\left(1-2\sin^2(\boldsymbol{\xi}\cdot\boldsymbol{r}^\gamma)\right)\hat{\boldsymbol{u}} \\
\int (\boldsymbol{u}^{\gamma+}-\boldsymbol{u}^{\gamma-})e^{\imath(\boldsymbol{\xi}\cdot\boldsymbol{x}-\omega t)}\mathrm{d}\boldsymbol{x}\mathrm{d}t &\approx 2\imath\{\sin(2\boldsymbol{\xi}\cdot\boldsymbol{r}^\gamma)\}\hat{\boldsymbol{u}}
\end{aligned}
\tag{4.21}
$$

Note that all the terms in the infinite series are included, and $\hat{\boldsymbol{u}}$ and $\hat{\boldsymbol{\theta}}$ are the Fourier transform of $\boldsymbol{u}$ and $\boldsymbol{\theta}$ with respect to the kernel $e^{\imath(\boldsymbol{\xi}\cdot\boldsymbol{x}-\omega t)}$. Substituting Eq. 4.12and Eq. 4.13 to Eq. 4.6 and taking the Fourier transform, we can obtain the following charateristic equations.

$$
\det\begin{bmatrix}
4\sum_\gamma K_{11}^\gamma\sin^2(\boldsymbol{\xi}\cdot\boldsymbol{r}^\gamma)-m\omega^2 & 4\sum_\gamma K_{12}^\gamma\sin^2(\boldsymbol{\xi}\cdot\boldsymbol{r}^\gamma) & 2\imath\sum_\gamma \hat{K}_{13}^\gamma\sin(2\boldsymbol{\xi}\cdot\boldsymbol{r}^\gamma) \\
4\sum_\gamma K_{21}^\gamma\sin^2(\boldsymbol{\xi}\cdot\boldsymbol{r}^\gamma) & 4\sum_\gamma K_{22}^\gamma\sin^2(\boldsymbol{\xi}\cdot\boldsymbol{r}^\gamma)-m\omega^2 & 2\imath\sum_\gamma \hat{K}_{23}^\gamma\sin(2\boldsymbol{\xi}\cdot\boldsymbol{r}^\gamma) \\
-2\imath\sum_\gamma \hat{K}_{31}^\gamma\sin(2\boldsymbol{\xi}\cdot\boldsymbol{r}^\gamma) & -2\imath\sum_\gamma \hat{K}_{32}^\gamma\sin(2\boldsymbol{\xi}\cdot\boldsymbol{r}^\gamma) & A-I_{33}\omega^2
\end{bmatrix}=0 \tag{4.22}
$$

Table 4.1: Predicted wave speeds and corresponding modes. $\zeta=a_2/a_1$ and $\eta=h/k$.

wave	$\theta_\xi=90°$		$\theta_\xi=0°$	
	phase speed	mode shape	phase speed	mode shape
p	$\sqrt{\frac{2ka_2}{\rho}}$	$\{0,1,0\}$	$\sqrt{\frac{ka_2(\eta+4\zeta)}{2\rho\zeta^2}}$	$\{1,0,0\}$
s	$\sqrt{\frac{2ka_2\eta(1+4\eta\zeta)}{\rho(1+4\eta\zeta+4\eta\zeta^2)}}$	$\left\{1,0,-\frac{4\eta\zeta^2\xi\mathrm{i}}{1+4\eta\zeta+4\eta\zeta^2}\right\}$	$\sqrt{\frac{2ka_2\eta(1+4\eta\zeta)}{\rho(1+4\eta\zeta+4\eta\zeta^2)}}$	$\left\{0,1,-\frac{(1+4\eta\zeta)\xi\mathrm{i}}{1+4\eta\zeta+4\eta\zeta^2}\right\}$
r	-	$\{0,0,1\}$	-	$\{0,0,1\}$

where $A=4\sum_\gamma \bar{K}^\gamma_{33}\cos^2(\boldsymbol{\xi}\cdot\boldsymbol{r}^\gamma)+4\sum_\gamma \bar{\bar{K}}^\gamma_{33}\sin^2(\boldsymbol{\xi}\cdot\boldsymbol{r}^\gamma)$

$\boldsymbol{I}$ is the moment of inertia tensor of a brick and $\mathbf{1}$ is the identity matrix. The details of the derivation is given in Appendix C.

The resulting set of characteristic equations are complicated and cannot be solved to obtain simple analytical expressions for wave properties. However, we can numerically solve it to find relation between frequencies and wave numbers; i.e. ω and $\boldsymbol{\xi}$.

4.3.3 The estimation of wave velocities

Like the spherical system, the frequency-wave number relations of primary, shear and rotational waves due to in-plane deformation are obtained. Unlike the the brick-wall has anisotropic wave characteristics (i.e. wave velocities depend on the direction of wave propagation). Table 4.1 shows the wave speeds estimated by $\lim_{\xi\to 0}\omega/\xi$, for the two cases with $\theta_\xi=0°$ and $\theta_\xi=90°$ where $\rho=m/V_\mathrm{b}$. Note that all the three continuum models produce the same p- and s-wave speeds in the neighborhood of $\xi=0$; i.e. $\lim_{\xi\to 0}\omega/\xi$ estimated with all the three models are equal. This is clearly visible in the ω vs. ξ graphs shown in the latter half of this chapter.

4.3.4 The estimation of rotational wave frequency

According to the continuum forms, the speed of rotational waves are undefined; i.e. $\lim_{\xi\to 0}\omega/\xi\to\infty$ for both $i=1,2$. This indicates that the rotational waves for the case $\xi\to 0$ (i.e. ${}^{2\pi}/_{\lambda}\to 0$, where λ is the wave length) are stationary waves. However, for this $\xi\to 0$ case, a finite wave frequency for rotational waves can be estimated as.

$$\omega_{\mathrm{spin}}=\sqrt{\frac{3ka_1^2+12ha_1a_2+12ha_2^2}{2\rho a_1^2a_2+2\rho a_2^3}}. \tag{4.23}$$

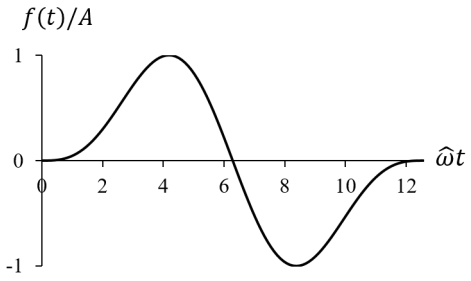

Figure 4.4: Input function.

4.4 Verification of the predictions made with continuum forms

Like with the spherical mass spring model, in order to verify the analytically predicted $\omega-\boldsymbol{\xi}$ relations for brick mortar system, we compare the predicted wave speeds given in Table 4.1 and the $\omega-\boldsymbol{\xi}$ relations from the characteristic equations of section 4.2 with those obtained from numerical simulations.

4.4.1 Basic problem settings

A single layered brick wall model with the width and height of $20.3\mathrm{m}$ and $13.0\mathrm{m}$, shown in Figure5.2, was used for the simulations. The dimensions of the bricks is $60\mathrm{mm}$ in width, $30\mathrm{mm}$ in height and $40\mathrm{mm}$ in thickness[11]. The density of each block is assumed to be $1850\mathrm{kg/m^3}$. The average elastic properties of the brick mortar system are approximately evaluated to be $k{=}5.12{\times}10^{11}\mathrm{N/m^3}$ and $h{=}2.22{\times}10^{11}\mathrm{N/m^3}$ [11].

The brick at the center of the domain is subjected to three different in-plane displacement boundary conditions. First and second cases are with transnational waves of vertical and horizontal excitation. The third case is with a rotational wave input. In all the cases, following smooth input function is used (Fig 4.4).

$$f(t){=}\frac{4}{3\sqrt{3}}A\left(\sin\frac{\hat{\omega}t}{2}-\frac{1}{2}\sin\hat{\omega}t\right), \tag{4.24}$$

where A is the amplitude of the input, $\hat{\omega}$ is the input circular frequency. The amplitude is set to be $2\mathrm{mm}$ for vertical and horizontal inputs, while amplitude of $0.035\mathrm{rad}$ is used for rotational input. To obtain a narrow waves such that peaks and valleys of waves are clearly visible, input circular frequency, $\hat{\omega}$, is set to be $1.57{\times}10^4\mathrm{rad/s}$ for vertical and horizontal input, and $2.11{\times}10^5\mathrm{rad/s}$ for rotational input.

To obtain accurate numerical results, second order velocity Verlet algorithm with $1\mu s$ time increments is used for time integration. It is observed that the energy and momentum of the whole system remain constant through ot the simulation. These indirect measures indicate that the simulations results have a high accuracy.

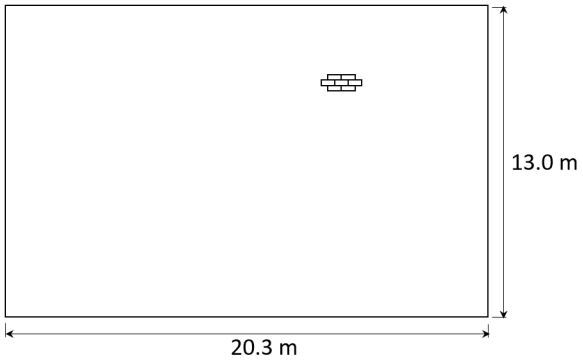

Figure 4.5: Domain for the numerical experiments.

4.4.2 Comparison of translational waves

Figure 4.6(a) and (b) compare the locations analytically predicted p- and s-wave front locations with that of numerically obtained. The color contours shows the distribution of numerically obtained translational wave amplitudes at t=2ms. Note that the amplitudes are normalized dividing with maximum amplitude (u/u_{max}). The two black curves are the predicted location of p- and s-wavefronts at t=2ms; the outermost indicates the p-wavefront, while the innermost indicates the s-wavefront. Analytic wave front locations are estimated with the wave speeds of Table 4.1. Primary or pressure wave

In Figure4.6(a), red color regions farthest above (region A) and below the point of input excitation are the p-wave fronts. The wave profiles along section P-P shown in Figure4.7 clearly indicates that the analytic predictions are in good agreement with the numerical results. Since the input excitation is vertically oriented, region A of Figure4.6(a) has high p-wave amplitudes, while p-wave amplitudes are negligibly small in all the other directions. This is why no p-wave front is present in the numerical results except farthest up and down (or left and right) in Figure 4.6a (Figure 4.6b). For the region C, the nearly straight wavefronts are the shear shock waves generated by the p-wave front in region A. Being an anisotropic medium, deformation due to p-, s- or rotational waves generates each other. s-waves generated by the p-wave front forms a shockwave, since p-wave speed is higher than s-wave.

4.4.2.1 Shear-wave

The red color stripes in the region B of Figure 4.6 show the major s-wave front. The amplitude of this main s-wave is weak in most directions, except in the directions orthogonal to the direction of input excitation. Especially, the shear wave in the directions of excitation have extremely small amplitudes. As shown in Figure4.8, in regions marked with B (or along section S-S), the theoretically predicated s-wavefronts are in good agreement with that of numerical results.

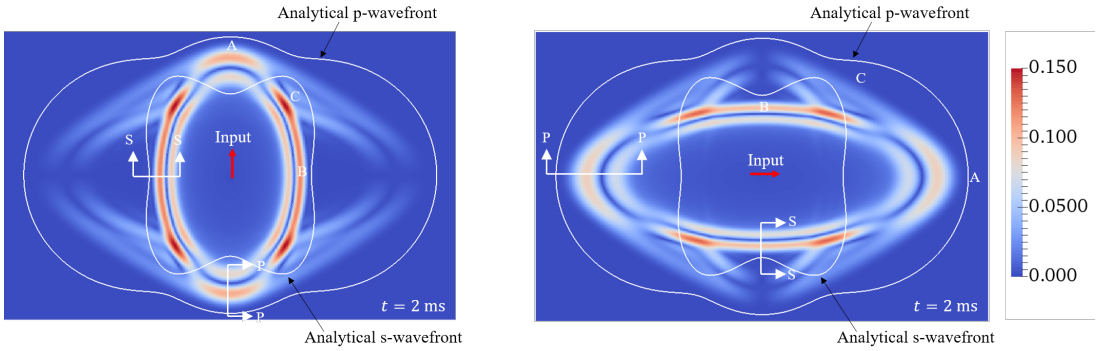

(a) with vertical input (b) with horizontal input

Figure 4.6: Comparison of predicted p- and s-wave fronts with those of numerical results, at t=2 ms. The colors indicates the amplitude of translational waves.

(a) Vertical input (b) Horizontal input

Figure 4.7: Translational wave profiles, along sections P-P, in the vicinity of p-wave front at t=2 ms. The arrows indicates the analytically predicted wave front location.

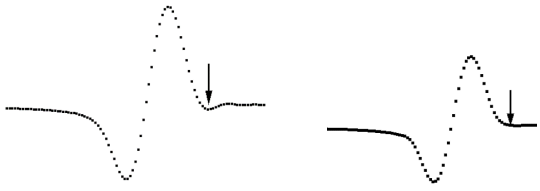

(a) Vertical input (b) Horizontal input

Figure 4.8: Translational wave profiles, along sections S-S, in the vicinity of s-wave front at t=2ms. The arrows indicates the analytically predicted wave front location.

4.4.3 Comparison of rotational-waves

Figure 5.5 shows the distribution of the normalized amplitudes of rotational waves generated by the rotational wave input at time t=2ms. Unlike the translational wave, the dispersion of the rotational wave is observed. To verify the analytical predicted dynamic characteristic of the rotational wave, double Fast Fourier Transform (FFT) with respect to length and time was conducted. FFT was conducted for two sets of narrow domains oriented horizontally and vertically; shown with white lines in Figure5.5.

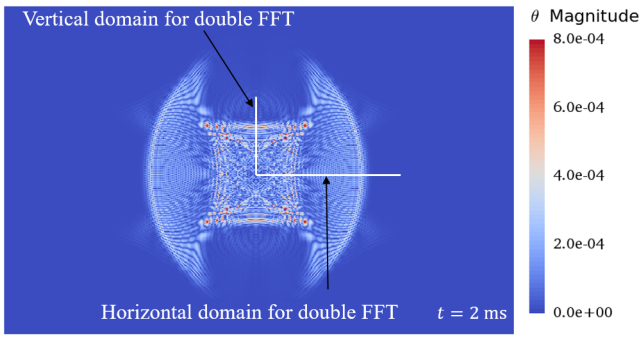

Figure 4.9: Magnitude of the rotational waves at 2 ms, generated by rotational wave input. Two white lines indicates the thins domains used for double FFT.

The color contours in Figure4.10 to 4.12 show the results of the double FFT and analytical solutions of $\omega-\xi$ relation obtained from the three continuum models. The vertical axis is circular frequency and the horizontal axis is the normalized wave number. Recall that a_1 and a_2 are the half of the length and height of a brick (see Figure4.3). The red, green, and yellow color curves are the the analytical solutions for p-, s- and r-waves, respectively. The orange lines in each figures indicate the numerical relation. The numerical results include not only the r-wave, but also s-wave. Though the p-wave also present, it's amplitude is very weak. This gives us another opportunity to check the accuracy of the predicted s-wave properties.

One interesting observation is that the the rotational waves have strong frequency dispersion behavior (i.e. waves of different speeds travels at different phase speeds). As a future study, it would be interesting to check whether rotational waves also have amplitude dispersion characteristics (i.e. waves of different amplitudes have different phase speeds).

4.4.3.1 Continuumnization

In Figure4.10, analytical solutions obtained from the continuumnization proposed by Hori et al.[1] is compared. It is seen that the rotational frequency matches the analytical results only within a small neighborhood of $|\xi a_1|=|\xi a_2|=0$, and rapidly diverge when moving away from $|\xi a_1|=|\xi a_2|=0$. The s-wave prediction also start to diverge when $|\xi a_1|<0.5$.

4.4.3.2 Continuum form from the second order Taylor expansion (CFSTE)

The analytical result from CFSTEis shown in Figure4.11. As is seen, the increase in the order of approximation for $\boldsymbol{\theta}$ has significantly increased the accuracy r-wave predictions producing a good agreement in the ranges $|\xi a_1|<0.5$ and $|\xi a_2|<0.5$. In other words, these predictions are valid for wavelengths grater than 7 times of the size of bricks ($\lambda>14a_i$). One unexpected observation is that s-wave predictions start to diverge rapidly outside the ranges $|\xi a_1|<0.5$ and $|\xi a_2|<0.5$. As mentioned above, the s-wave prediction of continuumnization also diverge beyond $|\xi a_1|=0.5$.

4.4.3.3 Continuum form from the infinite series approximation (CFIS)

The advantage of this continuum form is clearly seen in Figure4.12. Analytical predictions for s- and rotational waves are in near perfect agreement with the numerical results for the range $0<\xi a_i\leq 1.5$. Note that $\xi a_i=1.5$ is the the shortest meaningful wavelength which is twice the respective dimension of a brick (i.e. $\lambda\approx 2a_i$).

Obviously, Figure4.12 indicates that this continuum form can accurately reproduce the the strong frequency dispersion characteristics of r-waves. Thought the amplitudes of p- and s-waves are quite weak, except the s-wave in horizontal domain, still it is possible to identify the p- and s-wave signals with the help of analytic predictions. In Figure4.12 a, we can observe strong dispersion characteristics of p-wave in the range $1.0<\xi a_i\leq 1.5$. Also, Figure4.12 b, shows weak dispersion characteristics of s-wave in the same range. Though the analytic prediction shows strong dispersion of s-waves in the range $1.0<\xi a_i\leq 1.5$, this cannot be verified since s-wave amplitudes of the numerical results are extremely weak. However, this $1.0<\xi a_i\leq 1.5$ range may not be of importance for engineering applications.

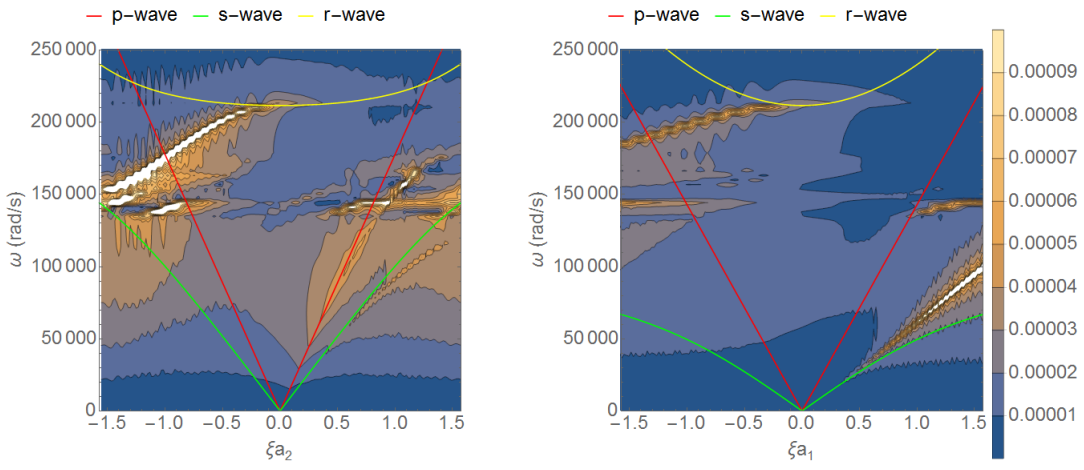

(a) Along the vertical domain

(b) Along the horizontal domain

Figure 4.10: Comparison of numerical results and the analytical predictions from original continuumnization model. Contour plots show the numerically obtained amplitude of ω vs. ξa_i relation. The curves shows the analytical prediction for p-, s- and rotational waves.

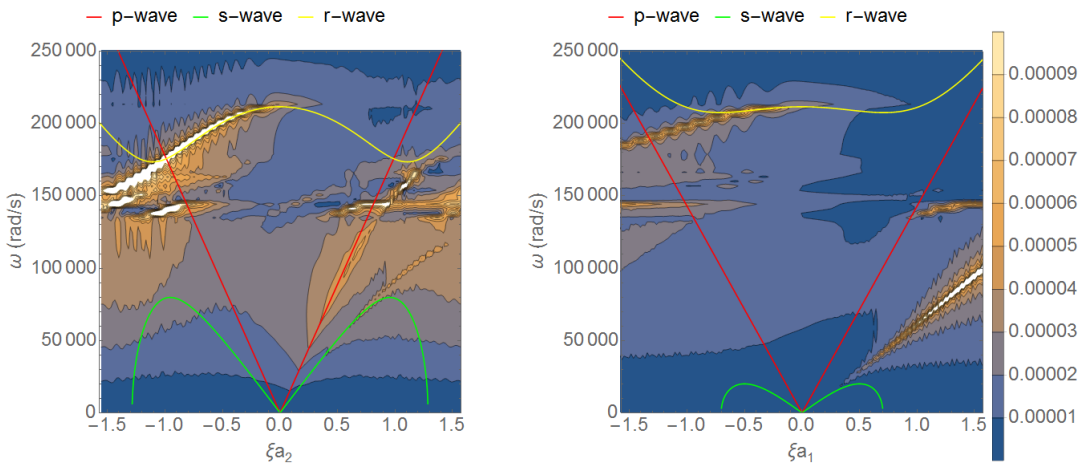

(a) Along the vertical domain

(b) Along the horizontal domain

Figure 4.11: Comparison of numerical results and the analytical predictions from the second order Taylor expansion. Contour plots show the numerically obtained amplitude of ω vs. ξa_i relation. The curves shows the analytical prediction for p-, s- and rotational waves.

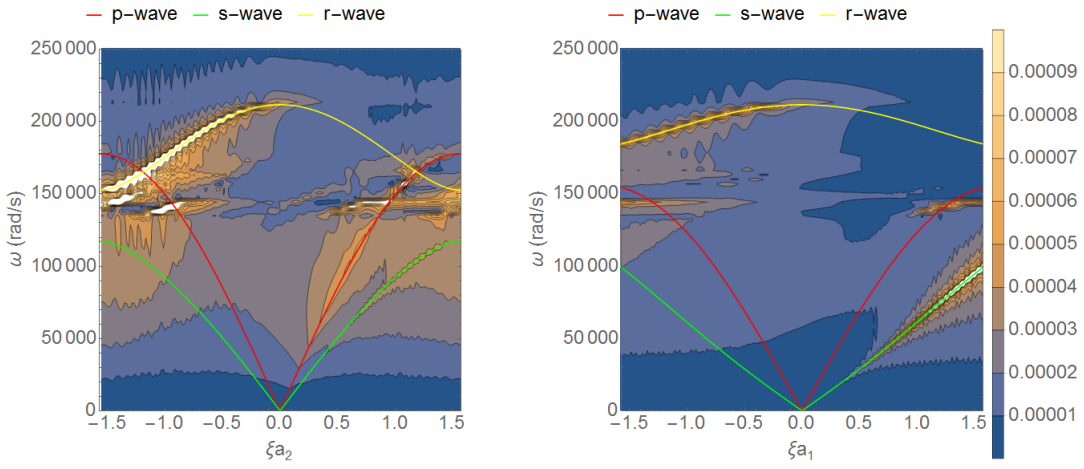

(a) Along the vertical domain

(b) Along the horizontal domain

Figure 4.12: Comparison of numerical results and the analytical predictions from inifinite series ((CFIS). Contour plots show the numerically obtained amplitude of ω vs. ξa_i relation. The curves shows the analytical prediction for p-, s- and rotational waves.

4.5 The estimation of spring constants based on experiment

One advantage of the continuumnization is that for known wave velocities, the equivalent normal spring constants, k and h can be accurately estimated using Table 4.1 . Note that although the spring constants, k and h, can be simply obtained by experiments like compression test or shear test[41, 42, 43], the obtained properties may not be suitable for studying dynamic behavior in brick structures. This is because the elastic properties obtained from static experiments may be different from the corresponding dynamic properties. Based on the above wave speed predictions, an accurate estimation of k and h for any given regular brick packing can be made with a several experimental measurements of wave speeds[16, 17, 18].

To demonstrate the application, consider the wave speed measurements by Schullerl et al.[40]. In their experiments, they used a horizontal input on the left side of a brick wall, with the packing shown in Figure4.3, and measured the arrival time at the right side edge at different locations. In this approach, wave velocity can be obtained for different propagation directions as shown in Figure4.13 where θ_ξ denotes the direction of propagation in Figure4.3. Brick size is about $250\mathrm{mm}\times33\mathrm{mm}\times63\mathrm{mm}$ and the density is assumed to be $1850\mathrm{kg/m^3}$. Based their experimental results and roughly approximated size and density, and our analytical predictions of wave speeds, the spring constants k and h are estimated to be $15.5\mathrm{N/mm^3}$ and $1.16\mathrm{N/mm^3}$. Only the experimental results at $\theta_\xi{=}0^\circ$ and the highest angle are used for this estimation. As seen in Figure4.13, when we use these estimated k and h our analytically predicted wave speeds are in a good agreement with the observations. There is a mismatch at the two points between $\theta_\xi{=}30^\circ$ to 60°range. This is probably due to the measurement errors; according to the simulations in the next section, p-wave amplitude at these angles are quite weak.

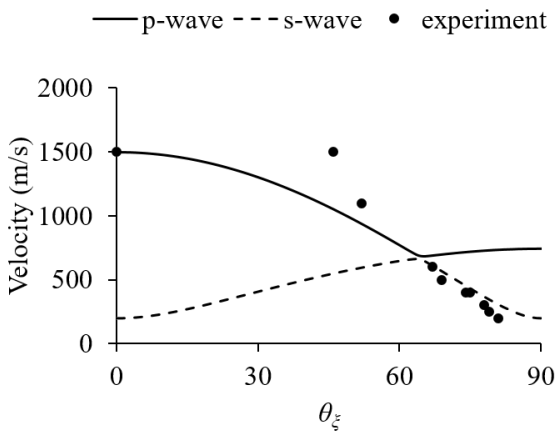

Figure 4.13: Experimentally obtained wave speeds by Schullerl et al.[40], and predicted wave speeds based on the estimated k and h.

4.6 Summary

The continuumnization for brick structures is formulated in this chapter. By solving characteristic equation of the continuumnizaed governing equations, frequency-wavenumber relations of for p-, s-, and r waves of brick wall are predicted. Further, analytical p-and s-wave speeds are analytically predicted. Based on these predictions, it is simple to learn the dynamic characteristic of brick systems for given packing and brick-mortar properties without the requirement of numerical simulation. Also, for known dynamic characteristic like wave velocity obtained by dynamic experiments, continuumnization allows us to rationally estimate equivalent dynamic elastic properties.

To verify the predicted dynamic characteristics based on the continuumnization, the predicted dynamic characteristics are compared with numerical RBSM simulation. For translational wave, the numerical and analytical predicted wavefront at a given travel time are compared. It is found that both numerical p- and s- wave are in good agreement with the corresponding predicted wavefronts' positions.

For r-wave, frequency-wavenumber relations for different approach are verified using double fast Fourior transform with respect to length and time domain. In this verification, the analytical relation based on the second order Taylor expansion (CFSTE) is also predicted.

For the comparison, continuumnization can predict wave properties accurately especially for s-wave while CFSTE approximation provides better prediction of r-wave dynamic characteristic.

Since CFSTE is applicable for wavelength 7 times longer than brick size, it is suitable for most of civil engineering application. Further, for the applications involving low relative wavelength, the analytical predictions based on the infinite series (CFIS) is recommended.

Chapter 5

PDS-FEM of brick mass-spring systems

An advantage of the developed continuum forms is that those allow us to use numerical methods in continuum mechanics like Finite Element Method (FEM) to simulate brick structures. This eliminates the need of coupling particle type simulators with FEM in simulating strutures made of bricks, steel, concrete, etc.; we can use FEM to simulate everything seamlessly. Futher, we can develop simplified models like plates and beams for simulating brick walls or columns. Such advantages would be attacrtive in structural designs. In this section, we implement PDS-FEM[2] extension for simulating brick structures based on the second order continuum model developed in section 4.2.2.

We chose PDS-FEM due to three main reasons: the particle nature of the PDS-FEM allows to consider brick arrangement itself as the tessellation for function approximation; straight forward to include moment of inertia of bricks, which are treated as rigid blocks in the starting discrete model; PDS-FEM provides a simple and efficient numerical treatment for modeling cracks. The formulation of PDS-FEM for brick structures and its verification are presented in this chapter. For the sake of simplicity, we only consider the 2D settings; straight forward to extend to 3D.

5.1 Particle Discretization Scheme (PDS)

A unique feature of PDS-FEM[2] that it uses characteristic functions of conjugate tessellations, $\{\Phi^\alpha\}$ and $\{\Psi^\beta\}$, for approximating functions and its derivatives, respectively. Originally, PDS-FEM uses characteristic functions of Voronoi and Delaunay tessellations. However, in this study,

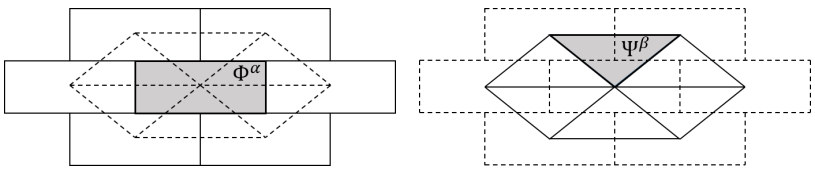

Figure 5.1: Dual tessellations used for PDS-FEM.

we uses the bricks themselves as the tessellation elements Φ^a; to be exact, each Φ^a includes half thickness of the cement layer along the perimeter of the brick (see Figure 5.1(a)). The conjugate tessellation$\{\Psi^\beta\}$ is formed with the triangles connecting the centroids of neighboring blocks; see Figure 5.1(b). Characteristic functions of Φ^a, denoted by $\phi^\alpha(\boldsymbol{x})$, is defined as

$$\phi^\alpha(\boldsymbol{x})=\begin{cases} 1 \text{ if } \boldsymbol{x}\in\Phi^\alpha \\ 0 \text{ if } \boldsymbol{x}\notin\Phi^\alpha \end{cases}.$$

The characteristict function of Ψ^β, denoted by $\psi^\beta(\boldsymbol{x})$, is defined as

$$\psi^\beta(\boldsymbol{x})=\begin{cases} 1 \text{ if } \boldsymbol{x}\in\Psi^\beta \\ 0 \text{ if } \boldsymbol{x}\notin\Psi^\beta \end{cases}.$$

According to PDS, an a vector field, $\boldsymbol{f}$, and its gradient,$\nabla\boldsymbol{f}$, are approximated as

$$f_i(\boldsymbol{x},t)\approx f_i^d(\boldsymbol{x}) = \sum_\alpha f_i^\alpha(t)\phi^\alpha(\boldsymbol{x}), \tag{5.1}$$

$$\frac{\partial f_i(\boldsymbol{x},t)}{\partial x_j}\approx g_{ij}^d(\boldsymbol{x}) = \sum_\beta f_{ij}^\beta(t)\psi^\beta(\boldsymbol{x}). \tag{5.2}$$

The unknown coefficients f_i^α's are determined by minimizing the error $E^f=\int(f_i-f_i^d)^2\mathrm{d}s$. Setting $\frac{\partial E^f}{\partial f_i^\alpha}=0$, we can evaluate f_i^α's as

$$f_i^\alpha=\frac{1}{\Phi^\alpha}\int_{\Phi^\alpha} f_i(\boldsymbol{x},t)\,\mathrm{d}s. \tag{5.3}$$

where Φ^α is the area of the tessellation elements,Φ^α.
The use of characteristic functions $\{\phi^\alpha\}$ introduces discontinuities to the approximation, f_i^d. However, PDS defines bounded approximation for the derivatives of f_i^d using the characteristic functions of conjugate tessellation Ψ^β to approximate the derivatives (Figure 5.1(a)). Minimizing the error $E^g=\int\left(g_{ij}^d(\boldsymbol{x})-\frac{\partial}{\partial x_j}f_i^d(\boldsymbol{x})\right)^2\mathrm{d}s$ by setting $\frac{\partial E^g}{\partial g_i^\beta}=0$, PDS defines the unknown coefficients u_{ij}^β's of $f_{ij}^d(\boldsymbol{x})$ as

$$f_{ij}^\beta=\sum_{a'}^{3} A_i^{\beta\alpha'} f_i^{\alpha'}, \tag{5.4}$$

where $\alpha'\in\{\alpha|\Psi^\beta\cap\Phi^\alpha\neq\emptyset\}$ denotes thee Φ^α's occupying the domain of , Ψ^β. Further,

$$A_i^{\beta\alpha}=\frac{1}{\Psi^\beta}\int_{\partial\Psi^\beta\cap\partial\Phi^\alpha} n_i^\alpha\mathrm{d}s.$$

Ψ^β is the area of the element Ψ^β . Analytical expression for $A_i^{\beta\alpha}$ are given in the Appendix D.

5.2 PDS-FEM based equations of motion of brick structures

We use the following Lagrangian as the starting point of PDS-FEM implementation of the continnum form of section 4.2.2.

$$J = \frac{1}{2V_{\mathrm{b}}}\int\left(m\dot{u}_j\dot{u}_j+\dot{\theta}_i I_{ij}\dot{\theta}_j\right)\mathrm{d}s-\frac{1}{2}\int u_{j,i}c_{ijkl}u_{l,k}-2\theta_j q_{lkj}u_{l,k}+\theta_i d_{ij}\theta_j+\theta_{j,i}c_{ijkl}\theta_{l,k}\mathrm{d}s \quad (5.5)$$

It is straight forward to show that $\delta\int J\,\mathrm{d}t=0$ produces the continuum form obtained with the second order Taylor expansion, Eq. 4.19.

According to PDS, the unknown displacement fields $\boldsymbol{u}$ and $\boldsymbol{\theta}$ are approximated using the tessellation, $\{\Phi^\alpha\}$, as

$$u_i \approx u_i^d = \sum_\alpha^{N^\alpha} u_i^\alpha \phi^\alpha \quad (5.6)$$

$$\theta_i \approx \theta_i^d = \sum_\alpha^{N^a} \theta_i^\alpha \phi^\alpha. \quad (5.7)$$

Recall that, we treated bricks as rigid blocks in deriving Eq. 4.6, which was the starting point in deriving the continuum forms. The use of characteristic functions of Φ^α to approximate $\boldsymbol{u}$ and $\boldsymbol{\theta}$ makes it possible to treat bricks as rigid blocks, making PDS-FEM an ideal tool to analyse brick structures. As it would be clear in the later formulation, no special treatments are necessary to include the intertia tensor of each brick, $\boldsymbol{I}$, in PDS-FEM.

The derivative of $u_{i,j}$ and $\theta_{i,j}$ approximated using $\{\Psi^\beta\}$ as $u_{i,j}\approx\sum_\beta u_{ij}^\beta\psi^\beta$ and $\theta_{i,j}\approx\sum_\beta\theta_{ij}^\beta\psi^\beta$. Based on the Eq. 5.4, the unknown coefficients can be expressed as

$$u_{ij}^\beta = \sum_{a'} A_j^{\beta\alpha'} u_i^{\alpha'} \quad (5.8)$$

$$\theta_{ij}^\beta = \sum_{a'} A_j^{\beta\alpha'} \theta_i^{\alpha'}. \quad (5.9)$$

Substituting Eq. 5.1 to 5.9 into Eq. 5.5, the discretized weak form, $J^d(\approx J)$, can be obtained as

$$
\begin{aligned}
J^d &= \int \frac{1}{2V_{\rm b}} \sum_{\alpha} \Big(m \dot{u}_i^{\alpha} \dot{u}_i^{\alpha} + \dot{\theta}_i^{\alpha} I_{ij} \dot{\theta}_j^{\alpha} \Big) \mathrm{d}s \\
&\quad - \sum_{\beta} \int_{\Psi^{\beta}} \left(\frac{1}{2} u_j^{\alpha} A_i^{\beta\alpha} c_{ijkl}^{\beta} A_k^{\beta\alpha'} u_l^{\alpha'} - \theta_j^{\alpha} \phi^{\alpha} q_{lkj}^{\beta} A_k^{\beta\alpha'} u_l^{\alpha'} + \frac{1}{2} \theta_j^{\alpha} \phi^{\alpha} d_{jl}^{\beta} \phi^{\alpha'} \theta_l^{\alpha'} + \frac{1}{2} \theta_j^{\alpha} A_i^{\beta\alpha} v_{ijkl}^{\beta} A_k^{\beta\alpha'} \theta_l^{\alpha'} \right) \mathrm{d}s \\
&= \frac{1}{2} \sum_{\alpha} \Big(m \dot{u}_i^{\alpha} \dot{u}_i^{\alpha} + \dot{\theta}_i^{\alpha} I_{ij} \dot{\theta}_j^{\alpha} \Big) - \sum_{\beta} \left(\frac{1}{2} u_j^{\alpha} K_{jl}^{\beta\alpha\alpha'} u_l^{\alpha'} - \theta_j^{\alpha} \check{K}_{jl}^{\beta\alpha\alpha'} u_l^{\alpha'} + \frac{1}{2} \theta_j^{\alpha} \tilde{K}_{jl}^{\beta\alpha\alpha'} \theta_l^{\alpha'} + \frac{1}{2} \theta_j^{\alpha} \grave{K}_{jl}^{\beta\alpha\alpha'} \theta_l^{\alpha'} \right),
\end{aligned}
$$

where

$$
\begin{aligned}
K_{jl}^{\beta\alpha\alpha'} &= \int_{\Psi^{\beta}} A_i^{\beta\alpha} c_{ijkl}^{\beta} A_k^{\beta\alpha'} \mathrm{d}s \\
\check{K}_{jl}^{\beta\alpha\alpha'} &= \int_{\Psi^{\beta}} \phi^{\alpha} q_{lkj}^{\beta} A_k^{\beta\alpha'} \mathrm{d}s \\
\tilde{K}_{jl}^{\beta\alpha\alpha'} &= \int_{\Psi^{\beta}} \phi^{\alpha} d_{jl}^{\beta} \phi^{\alpha'} \mathrm{d}s \\
\grave{K}_{jl}^{\beta\alpha\alpha'} &= \int_{\Psi^{\beta}} A_i^{\beta\alpha} v_{ijkl}^{\beta} A_k^{\beta\alpha'} \mathrm{d}s
\end{aligned}
$$

The explicit expression for these, in matrix form, are given in Appendix D. Setting $\delta \int J^d \boldsymbol{d}t = 0$

$$
\begin{aligned}
\delta \int_{t_1}^{t_2} J^d \mathrm{d}t &= \Big[m \dot{u}_j^{\alpha} \delta u_j^{\alpha} + \dot{\theta}_i^{\alpha} I_{ij} \delta u_j^{\alpha} \Big]_{t_1}^{t_2} - \int_{t_1}^{t_2} \Big(m \ddot{u}_j^{\alpha} \delta u_j^{\alpha} + I_{ij} \ddot{\theta}_i^{\alpha} \delta \theta_j^{\alpha} \Big) \mathrm{d}t \\
&\quad - \int_{t_1}^{t_2} \Big(u_j^{\alpha} K_{jl}^{\beta\alpha\alpha'} \delta u_l^{\alpha'} - \theta_j^{\alpha} \check{K}_{jl}^{\beta\alpha\alpha'} \delta u_l^{\alpha'} \\
&\quad - \delta \theta_j^{\alpha} \check{K}_{jl}^{\beta\alpha\alpha'} u_l^{\alpha'} + \delta \theta_j^{\alpha} \Big(\tilde{K}_{jl}^{\beta\alpha\alpha'} + \grave{K}_{jl}^{\beta\alpha\alpha'} \Big) \theta_l^{\alpha'} \Big) \mathrm{d}t \\
0 &= - \int_{t_1}^{t_2} \Big(m^{\alpha} \ddot{u}_j^{\alpha} + K_{jl}^{\beta\alpha\alpha'} u_l^{\alpha'} - \check{K}_{lj}^{\beta\alpha'\alpha} \theta_l^{\alpha'} \Big) \delta u_j \mathrm{d}s \mathrm{d}t \\
&\quad - \int_{t_1}^{t_2} \int_{\Omega} \Big(I_{jl}^{\alpha} \ddot{\theta}_l^{\alpha} - \check{K}_{jl}^{\beta\alpha\alpha'} u_l^{\alpha'} + \Big(\tilde{K}_{jl}^{\beta\alpha\alpha'} + \grave{K}_{jl}^{\beta\alpha\alpha'} \Big) \theta_l^{\alpha'} \Big) \delta \theta_j \mathrm{d}s \mathrm{d}t
\end{aligned}
$$

Since the above should hold for arbitrary δu_i^{α} and $\delta \theta_i^{\alpha}$, we can obtain the following set of equations. With a suitable time integrator, we can use this linear set of equations to study the transient wave propagation in brick structures.

$$m^{\alpha}\ddot{u}_j^{\alpha} = \sum_{\beta}\left(-K_{jl}^{\beta\alpha\alpha'}u_l^{\alpha'}+\check{K}_{lj}^{\beta\alpha'\alpha}\theta_l^{\alpha'}\right) \tag{5.10}$$

$$I_{jl}^{\alpha}\ddot{\theta}_l^{\alpha} = \sum_{\alpha}\left\{\check{K}_{jl}^{\beta\alpha\alpha'}u_l^{\alpha'}-\left(\tilde{K}_{jl}^{\beta\alpha\alpha'}+\grave{K}_{jl}^{\beta\alpha\alpha'}\right)\theta_l^{\alpha'}\right\}. \tag{5.11}$$

5.3 Verification of PDS-FEM with analytical solution

To verify the developed PDS-FEM code, a brick wall PDS-FEM model is constructed. Numerical result of the propagation of waves will be compared with the analytical result in chapter 4. The problem setting and verification method are the same as that of chapter 4. A brick wall of width $20.3\mathrm{m}$ and height $13.0\mathrm{m}$ shown in Figure5.2 was used for the simulations. The domain consists of bricks with $60\mathrm{mm}$ width, $30\mathrm{mm}$ high,$40\mathrm{mm}$ thickness, and $5\mathrm{mm}$ mortar thickness[11] simulation. The density of each block is assumed to be $1850\mathrm{kg/m^3}$. Averaging brick-mortar material properties[11], k and h, are determined as $512\mathrm{N/mm^3}$ and $222\mathrm{N/mm^3}$, respectively.

The domain is subjected to in-plane one wave input at center of the domain. In this numerical experiment, 3 input cases. First and second cases are with vertical and horizontal transnational wave inputs. The third case is with a rotational wave input. In all the cases, following wave form is used.

$$f(t)=\frac{4}{3\sqrt{3}}A\left(\sin\frac{\omega t}{2}-\frac{1}{2}\sin\hat{\omega}t\right), \tag{5.12}$$

where A is the amplitude of the input, $\hat{\omega}$ is the input circular frequency. The amplitude is set to be $2\mathrm{mm}$ for vertical and horizontal input. For rotational input, the amplitude is $0.035\mathrm{rad}$. To obtain a narrow waves, so that peaks and valleys of waves are clearly visible, input circular frequency $\hat{\omega}$ is set to be $1.57\times10^4\mathrm{rad/s}$ for vertical and horizontal input, and $2.11\times10^5\mathrm{rad/s}$ for rotational input.

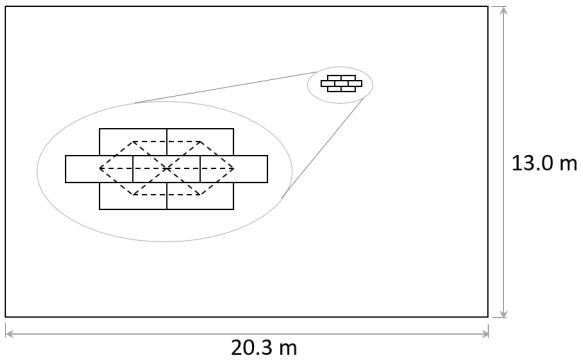

Figure 5.2: Domain for the numerical experiment

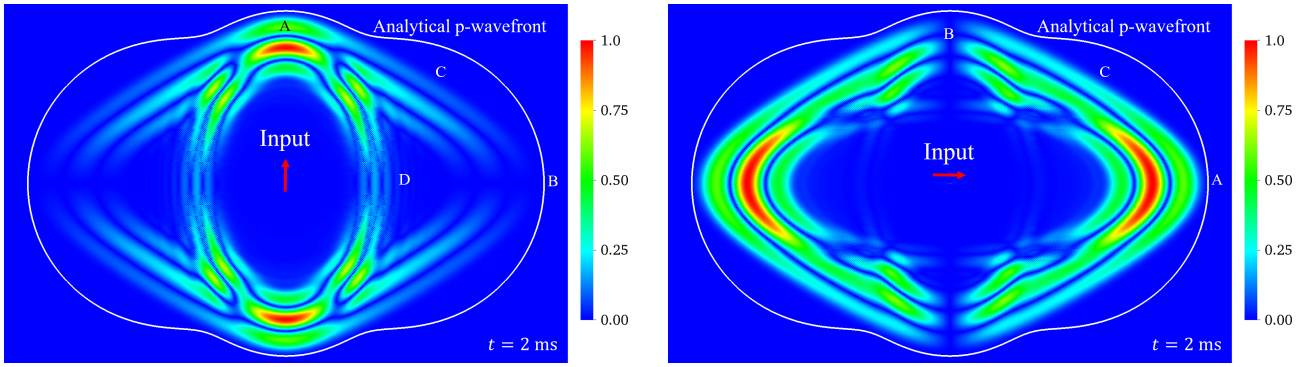

Figure 5.3: Hydrostatic strain and analytical p-wave front (white line) at 2ms travel time: (a) vertical input, (b) horizontal input.

5.3.1 Primary or pressure-wave

Like the RBSM model, the numeical result of RBSM can be verified with analytical prediction on continuum forms. Figure5.3 shows the distribution of hydrostatic strain, which indicates the amplitude of p-wave, at time 2 ms. The thin white line is the theoretically predicted p-wave front.

As is seen, the analytical prediction is in good agreement with numerical results in the regions indicated with letter A. In Figure 5.3(a), since the input wave is oriented in vertical direction, the p-wave amplitude is strong in up and down directions, while it is weak in other directions. This is why no wavefront is present in the directions except up and down, in the numerical results. The nearly straight wavefronts in the region C are the shear shock waves generated by the p-wavefront in region A; being an anisotropic medium, deformation due to p-, s- or rotational waves generates each other.

5.3.2 Shear-wave

Figure 5.3 shows the distribution of maximum shear strain, which indicates the amplitude of S-wave, at time 2 ms. The thin white line is the theoretically predicted s-wave fronts.

High amplitude s-wave can be observe in the area A. As seen there is a good agreement with the analytical prediction in these regions. High amplitude shear waves propagate in normal directions to the direction of excitation, and amplitudes in other directions are weak. Especially, shear waves in the directions of excitation have extremely small amplitudes. This is why there seems to be a mismatch between numerical and analytical wave fronts in regions except A. Further, the p-wave generated shear deformation is clearly visible in regions C and D. The near straight stripes in region D are the shear shock waves corresponding to those of region C in Figure 5.3.

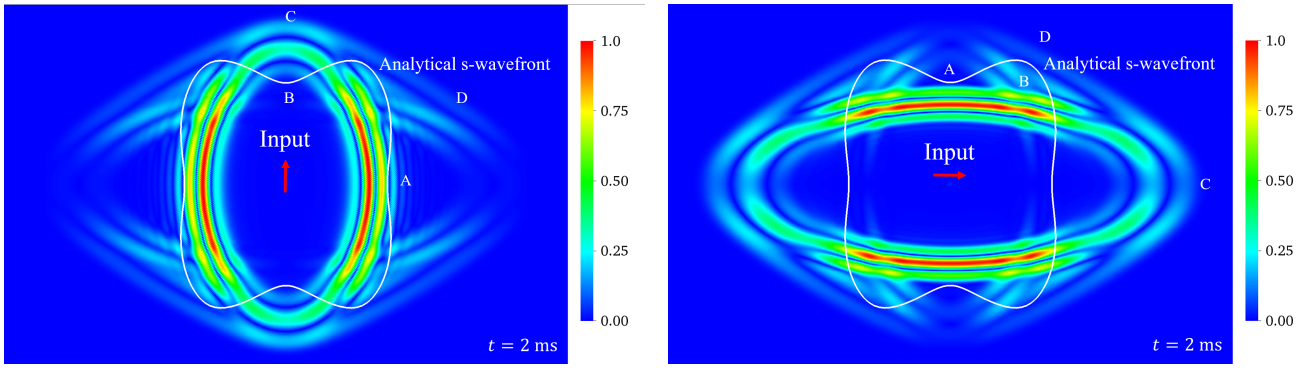

(a) (b)

Figure 5.4: Maximum shear strain and analytical s-wave front (white line) at 2ms travel time: (a) vertical input, (b) horizontal input.

5.3.3 Rotational-wave

Figure 5.5 shows the distribution of the amplitudes of rotational waves generated by the rotational wave input. Unlike the single wave input, the dispersion of the rotational wave occurs. Due to the difficultly of analytically estimate the rotational wave velocity, the double Fast Fourier Transform (FFT) with respect to spatial and time domain is applied. FFT is conducted for two sets of narrow domains oriented horizontally and vertically; shown with yellow lines in Figure5.5.

The double FFT result is shown in Figure5.6. The vertical axis is circular frequency and the horizontal axis is the normalized wave number, where a_1 and a_2 are the half of the length and height of a brick (Figure4.3). The numerical result is represented by the orange area. Note that the white indicates that the amplitude is beyond the color scale. Red, green, and yellow lines represented the analytical solutions from the Eq. 4.19 for p-, s- and r-waves, respectively. It is observed that there is not only r-wave, but also small amplitude p- and s-wave. It is seen that the numerical solution is in good agreement when $|\xi a_1|<0.5$ and $|\xi a_2|<0.5$. In other words, the PDS-FEM is valid for the wavelength is grater than 7 times of the size of bricks.

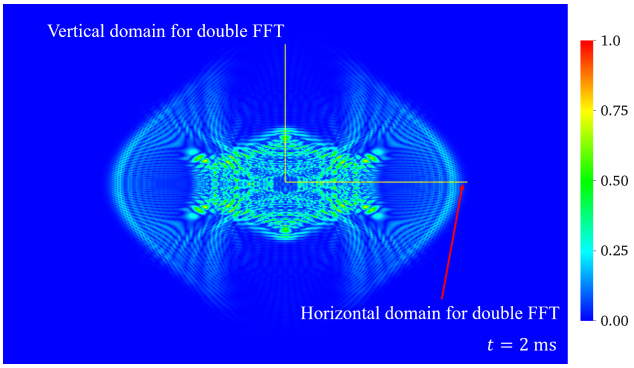

Figure 5.5: Numerical rotational magnitude and domain setting form double FFT.

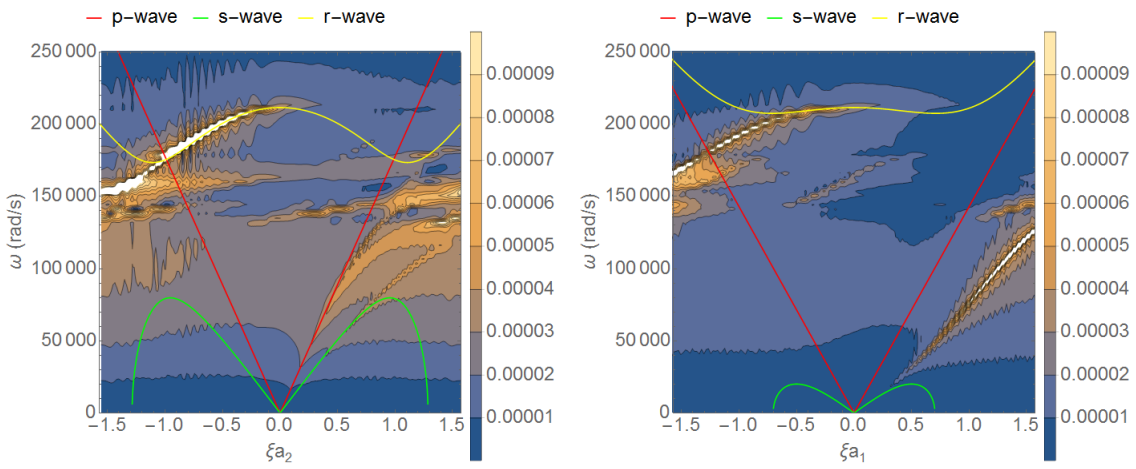

(a) vertical domain

(b) horizontal domain

Figure 5.6: Contour plot of the numerical rotational magnitude and the analytical relation between wave circular frequency and and normalized wave number based on second order Taylor's expansion.

Though verification of PDS-FEM is restricted by the applicable range of the continuum form based on second order Taylor's expansion (section 4.2.2), PDS-FEM can be verified with the continuum form based on infinite series expansion. As shown in Figure 5.7, it is seen that PDS-FEM can provide better range of applicability.

5.4 Verification of PDS-FEM with RBSM

Though the numerical simulation of PDS-FEM can be verified with analytical solutions, it is not convenient to verify amplitude of movement in the numerical simulation. Alternatively, PDS-FEM is verified RBSM simulation with the same problem setting. Contour colors in Figure 5.8 represents the error of the PDS determined by the following equation

$$Error = \frac{|\boldsymbol{u}^{\mathrm{PDS}} - \boldsymbol{u}^{\mathrm{RBSM}}|}{\mathrm{Input amplitude}} \times 100\%$$

where $\boldsymbol{u}^{\mathrm{PDS}}$ and $\boldsymbol{u}^{\mathrm{RBSM}}$ are the translation of the wave propagation based on the PDS-FEM and RBSM, respectively. It is found that the maximum error occurs in the high amplitude area of s-wave indecated by the red area in for vertical input case (see Figure 5.8(a)) which is about 4%.

5.5 Summary

In this chapter, the continuumnization based discretization scheme finite element model (PDS-FEM) for 2d brick wall is formulated. The PDS-FEM can represent the movement of the brick as

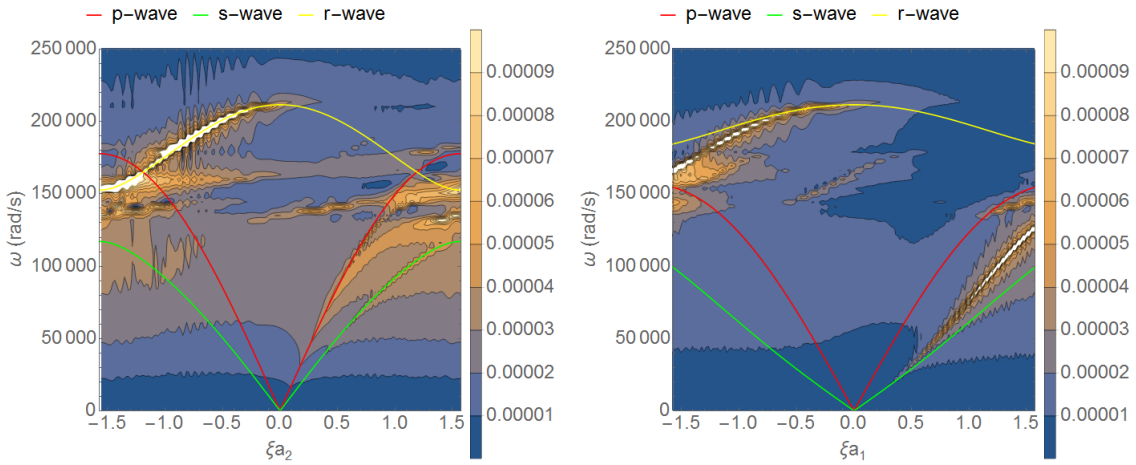

(a) vertical domain (b) horizontal domain

Figure 5.7: Contour plot of the numerical rotational magnitude and the analytical relation between wave circular frequency and and normalized wave number based on infinite series expansion.

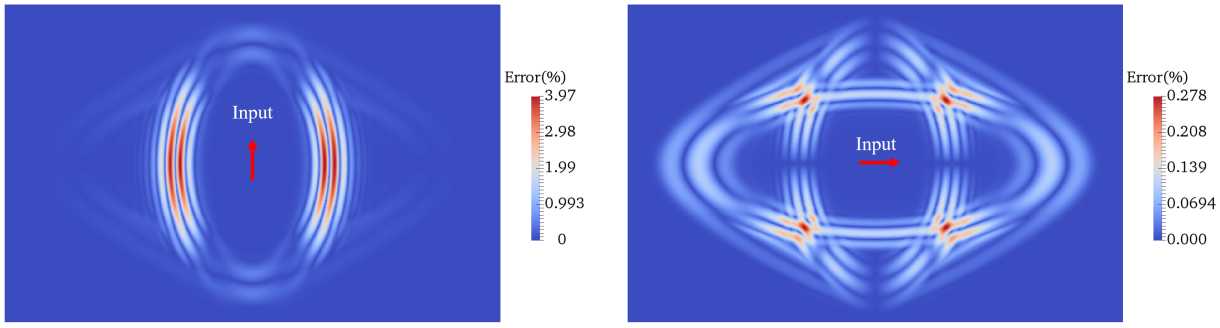

(a) (b)

Figure 5.8: Error of translation in PDS compared to RBSM: (a) vertical input, (b) horizontal input.

brick wall systems is the set of particles. The verification of the PDS-FEM shows that the numerical results are in good agreement with analytical solution for both time and frequency domain. According to the verification, the range of applicability is wavelength 7 times longer than the size of bricks which is sufficient for civil engineering applications. Further, this PDS-FEM of brick structures can be further developed for non-linear systems or cracking simulation.

Chapter 6

Role of rotation on the damping of brick structures

According to both the analytic solutions and numerical simulations presented in previous chapters, the frequency of rotational DOF is significantly high to be physically feasible. As an example, according to Eq. 4.23 the rotational frequency for the brick wall considered in section 6 is about 2×10^5 rad/s. Such high frequency rotational motion is physically unfeasible and should rapidly decay due to interface friction, non-linear properties of mortar, etc. Further, some energy from transnational modes to rotational mode since these two modes are coupled via the third order tensor $\boldsymbol{q}$. Consequently, this rapid decay and coupling make the system to continuously loose energy producing a damping effect. This could be one possible damping mechanism in systems made up of stiff interacting particles like sand, brick -mortar, etc.

In this section, we investigate this hypothesized damping mechanism of stiff interacting particle systems. We focus on brick mortar systems due to the potential applications in the vibration resistance design of brick structures.

6.1 Rotation induced damping of brick structures: formulation

For the sake of simplicity, let's consider a regularly arranged 2D brick mortar system, and the method of continuumnization (see section 4.2.1). Based on Eq. 4.10, the governing equation of the equivalent continuum form for this 2D system can be expressed as

$$\frac{m}{V_b}\ddot{u}_i = c_{ijkl}\frac{\partial^2 u_j(\boldsymbol{x})}{\partial x_k \partial x_l} - q_{i3k}\frac{\partial \theta_3(\boldsymbol{x})}{\partial x_k} \tag{6.1}$$

$$\frac{I_{33}}{V_b}\ddot{\theta}_3 = q_{p3k}\frac{\partial u_p(\boldsymbol{x})}{\partial x_k} - \upsilon_{33}\theta_3(\boldsymbol{x}). \tag{6.2}$$

As discussed at the introduction of this chapter, the rotational motion should damp rapidly. To model the loss of energy transferred into the rotational mode, we eliminate the rotational DOF θ_3 from the above system of equations expressing $\theta_3{=}\theta_3(u_i)$. First, we express θ_3 in terms of u_i's based on Eq. 6.2; i.e. $\theta_3{=}\theta_3(u_i)$. Then, based on this relation, we eliminate θ_3 from Eq. 6.1. The resulting equations will be devoid of θ_3, but contains the effects of transferring energy from translation mode to rotational mode via the coupling term q_{i3k}, eventually producing a damping effect.

Taking Fourier or Laplace transform of Eq. 6.2 and solving the resulting equations, we can express θ_3 in terms of u_i. However, the resulting equation involves convolution of u_i's making it too complicated to be used (see Appendix ###). Instead, we use Fourier transform of Eq. 6.2, make a first order approximation in Fourier domain, and obtain an approximate expression for θ_3 in terms of u_i's. In the rest of this subsection, the details of this formulation are given.

6.1.1 Approximation of θ_3 in term of u_i

Taking Fourier transform of Eq. 6.2 with respect to time domain and re-arranging, we can obtain

$$\Theta_3(\omega){=}q_{lk3}G(\omega)U_{l,k}(\omega), \tag{6.3}$$

where $U_l(\omega){=}\mathcal{F}(u_l(t))$ and $\Theta_3{=}\mathcal{F}(\theta(t))$ are the Fourier transform of u_i and θ_3, and

$$G(\omega){=}\frac{1}{d_{33}{-}\omega^2 I_{33}/V_{\mathrm{b}}}, \tag{6.4}$$

Fourier transform of a function $f(t)$ is defined as $\mathcal{F}(f(t)){=}\int_{\infty}^{\infty} f(t)e^{-\imath\omega t}\mathrm{d}t$. Taking the inverse Fourier transform of Eq. 6.3, we can express θ_3 in terms of u_i's. However, the resulting expression becomes a convolution, due to the nature of the transfer function $G(\omega)$, making it difficult to use with Eq. 6.1. In order to simplify it, we consider a first order approximation of the transfer function $G(\omega)$ taking the Taylor series expansion around ω_0 as

$$G(\omega){\approx}G(\omega_0){+}G'(\omega_0)(\omega{-}\omega_0) \tag{6.5}$$

where $G'{=}{}^{\partial G}/_{\partial\omega}$. Substituting Eq. (6.5) into Eq. (6.3), $\Theta_3(\omega)$ is approximated as

$$\Theta_3(\omega) \;=\; q_{lk3}\{G(\omega_0){-}\omega_0 G'(\omega_0)\}U_{l,k}(\omega){+}\omega q_{lk3}G'(\omega_0)U_{l,k}(\omega) \tag{6.6}$$

Finally, taking inverse Fourier transform of Eq.6.6, an approximation for θ_3 can be obtained in term of $u_{l,k}$ and $\dot{u}_{l,k}$ as

$$\theta_3{=}q_{lk3}\{G(\omega_0){-}\omega_0 G'(\omega_0)\}u_{l,k}{-}\imath q_{lk3}G'(\omega_0)\dot{u}_{l,k} \tag{6.7}$$

The in-plane rotation, θ_3, is expressed in term of gradient of translation, $u_{l,k}$, and gradient of velocity, $\dot{u}_{l,k}$. The imaginary term indicates that $u_{l,k}$ and $\dot{u}_{l,k}$ are in opposite phases. This is a

sign that the term with $\dot{u}_{l,k}$ produces a damping effect by working against the real part. The real and imaginary parts of the Fourier transform corresponds to the Fourier transform of odd and even parts of a function (see Appendix G). Hence, we can express θ_3 as

$$\theta_3 = q_{lk3}\{G(\omega_0) - \omega_0 G'(\omega_0)\}u_{l,k} - q_{lk3}G'(\omega_0)\dot{u}_{l,k} \tag{6.8}$$

6.1.2 Equation of motion with the rotation induced damping

Substituting above obtained approximation of θ_3 to Eq. 6.1, we get

$$\rho\ddot{u}_j - C_{ijkl}(\omega_0)u_{l,ik} - \hat{C}_{ijkl}(\omega_0)\dot{u}_{l,ik} = 0 \tag{6.9}$$

where

$$\begin{aligned} C_{ijkl}(\omega_0) &= c_{ijkl} - q_{ji3}q_{lk3}G(\omega_0) + \omega_0 q_{ji3}q_{lk3}G'(\omega_0) \\ \hat{C}_{ijkl} &= q_{ji3}q_{lk3}G'(\omega_0) \end{aligned}$$

The of partial differential equations given by Eq. 6.9 is the equivalent continuum form for the system with hypothesized rotation induced damping. The elimination of θ_3 has made the Eq. 6.9 a function of ω_0. Specifically, C_{ijkl}, which is similar to the elasticity tensor in continuum mechanics is a function of ω_0; $C_{ijkl} = C_{klij}$. Note that the term $\hat{C}_{ijkl}\dot{u}_{l,ik}$ introduces damping to the system since it carries the effect of the imaginary term in Eq. 6.7.

6.2 PDS-FEM implementation of the damped system

As we did earlier in Chapter 5, we use PDS-FEM to solve the above partial differential equations of initial-boundary value problem. Compared to the target partial differential equations chapter 5, Eq. 6.9 has two major differences; it contains damping terms (i.e. models a non-conservative system) and includes a term with second order spatial derivatives and first order time derivative ($\dot{u}_{l,ik}$). Apart from the additional treatments to deal with these two differences, this PDS-FEM formulation involves the same steps as in chapter 5.

6.2.1 A weak form for the non-conservative system

Consider a system which is described by the following Lagrangian

$$\mathcal{L} = \int_\Omega \frac{1}{2}m\dot{u}_i\dot{u}_i - \frac{1}{2}C_{ijkl}\frac{\partial u_i}{\partial x_j}\frac{\partial u_k}{\partial x_l}\mathrm{d}s$$

and subjected to the non-conservative forces $-\hat{C}_{iljk}\dot{u}_{j,kl}(\boldsymbol{x},t)$. Let $\delta W = -\hat{C}_{iljk}\dot{u}_{j,kl}(\boldsymbol{x},t)\delta u_i$ be the virtual work done by these non-conservative forces due to compatible virtual displacement δu_i. Applying the Hamilton's principle, we can obtain the governing equations for this system as

$$\begin{aligned}
\delta\int\mathcal{L}\mathrm{d}t+\int\delta W\,\mathrm{d}t &= 0\\
\cancelto{0}{\left[\int_\Omega m\dot{u}_i\delta u_i\mathrm{d}s\right]_{t_1}^{t_2}}-\int\int_\Omega m\ddot{u}_i\delta u_i\mathrm{d}s\mathrm{d}t-\cancelto{0}{\int_{\partial\Omega}\int C_{ijkl}\delta u_i\frac{\partial u_k}{\partial x_l}n_j\mathrm{d}s\mathrm{d}t} &\\
+\int_\Omega\int\delta u_i\frac{\partial}{\partial x_j}\left(C_{ijkl}\frac{\partial u_k}{\partial x_l}\right)\mathrm{d}s\mathrm{d}t+\int\int_\Omega\hat{C}_{iljk}\dot{u}_{j,kl}\delta u_i\mathrm{d}s\mathrm{d}t &= 0\\
\int\int_\Omega\left(m\ddot{u}_i-\frac{\partial}{\partial x_j}\left(C_{ijkl}\frac{\partial u_k}{\partial x_l}\right)-\hat{C}_{iljk}\dot{u}_{j,kl}\right)\delta u_i\mathrm{d}s\mathrm{d}t &= 0
\end{aligned}$$

Note that we use the property $C_{ijkl}=C_{klij}$ in the above derivation. The above should hold for compatible arbitrary δu_i, hence producing the Eq. 6.9.

6.2.2 PDS-FEM implementation for the damped system

As shown above, we can use the above Lagrangian with the non-conservative force $-C_{iljk}\dot{u}_{j,kl}(\boldsymbol{x},t)$ as the starting point of PDS-FEM formulation. First, we approximate all the field variables involved using PDS. Just as we did in chapter 5, the unknown displacement field $\boldsymbol{u}$ is approximated using Voronoi tessellation, Φ^α, as

$$u_i \approx u_i^d = \sum_\alpha u_i^\alpha\phi^\alpha(\boldsymbol{x}), \tag{6.10}$$

and the derivative of $u_{i,j}$ is approximated using Delaunay tessellation, $\{\Psi^\beta\}$, as $u_{i,j}\approx\sum_\beta u_{ij}^\beta\psi^\beta(\boldsymbol{x})$, where the coefficients $\bar{u}_{ij}^\beta$ can be expressed as

$$u_{ij}^\beta = \sum_\alpha A_j^{\beta\alpha}u_i^\alpha. \tag{6.11}$$

As described in chapter 5, PDS uses conjugate tessellations to approximate function and it's derivatives. We make use of fundamental feature of PDS to approximate higher order derivatives. Specifically, in order to approximate the second order spatial derivative $u_{i,jk}$ we use the tessellation $\{\Phi^\alpha\}$, which is the conjugate of the tessellation used for approximating $u_{i,j}$.

$$u_{i,jk} \approx \sum_\alpha u_{ijk}^\alpha\phi^\alpha(\boldsymbol{x})$$

where the coefficients u_{ijk}^{α} can be found by minimizing the error $\int \left(u_{ijk}^{\alpha} \phi^{\alpha}(\boldsymbol{x}) - \left(u_{ij}^{\beta} \psi^{\beta}(\boldsymbol{x}) \right)_{,k} \right)^2 \mathrm{d}s$ as

$$\begin{aligned} u_{ijk}^{\alpha} &= \sum_{\beta} u_{ij}^{\beta} \left(\frac{1}{\Phi^{\alpha}} \int_{\partial \Phi^{\alpha}} \phi^{\alpha}(\boldsymbol{x}) n_k^{\beta} \mathrm{d}l \right) \\ &= \sum_{\beta} u_{ij}^{\beta} S_k^{\alpha\beta}. \qquad \{\beta \,|\, \Phi^{\alpha} \cap \Psi^{\beta} \neq \emptyset\} \end{aligned} \tag{6.12}$$

Analytic expression for $S_i^{\alpha\beta}$ are given in the Appendix D.

Substituting the above approximations to $\delta \int \mathcal{L} \mathrm{d}t + \int \delta W \, \mathrm{d}t = 0$, we can derive the governing linear set of equation of PDS-FEM as follows

$$\int \left(\delta \int_{\Omega} \frac{1}{2} \rho \dot{u}_i \dot{u}_i - \frac{1}{2} C_{ijkl} \frac{\partial u_i}{\partial x_j} \frac{\partial u_k}{\partial x_l} \mathrm{d}s + \int_{\Omega} \hat{C}_{iljk} \dot{u}_{j,kl} \delta u_i \mathrm{d}s \right) \mathrm{d}t = 0$$

$$\int \left(\sum_{\alpha} \frac{1}{2} \delta \int_{\Phi^{\alpha}} \rho^{\alpha} \dot{u}_i^{\alpha} \dot{u}_i^{\alpha} \phi^{\alpha}(\boldsymbol{x}) - \sum_{\beta} \frac{1}{2} \delta \int_{\Psi^{\beta}} C_{ijkl}^{\beta} u_{ij}^{\beta} u_{kl}^{\beta} \psi^{\beta}(\boldsymbol{x}) \mathrm{d}s \right.$$

$$\left. - \sum_{\alpha} \int_{\Phi^{\alpha}} \hat{C}_{iljk}^{\alpha} \dot{u}_{jkl}^{\alpha} \delta u_i^{\alpha} \phi^{\alpha}(\boldsymbol{x}) \mathrm{d}s \right) \mathrm{d}t = 0$$

$$\int \left(\sum_{\alpha} \frac{1}{2} m^{\alpha} \delta(\dot{u}_i^{\alpha} \dot{u}_i^{\alpha}) - \sum_{\beta} \frac{1}{2} \delta \left(u_{ij}^{\beta} u_{kl}^{\beta} \right) C_{ijkl}^{\beta} \Psi^{\beta} + \sum_{\alpha} \hat{C}_{iljk}^{\alpha} \dot{u}_{jkl}^{\alpha} \Phi^{\alpha} \delta u_i^{\alpha} \right) \mathrm{d}t = 0$$

$$\int \left(\sum_{\alpha} \frac{1}{2} m^{\alpha} \delta(\dot{u}_i^{\alpha} \dot{u}_i^{\alpha}) - \sum_{\beta} \frac{1}{2} \delta \left(\left(\sum_{\alpha} A_j^{\beta\alpha} u_i^{\alpha} \right) \left(\sum_{\alpha'} A_l^{\beta\alpha'} u_k^{\alpha'} \right) \right) C_{ijkl}^{\beta} \Psi^{\beta} \right.$$

$$\left. + \sum_{\alpha} \hat{C}_{iljk}^{\alpha} \left(\sum_{\beta} S_l^{\alpha\beta} \dot{u}_{jk}^{\beta} \right) \Phi^{\alpha} \delta u_i^{\alpha} \right) \mathrm{d}t = 0$$

$$\cancelto{0}{\int \sum_{\alpha} m^{\alpha} \frac{\mathrm{d}}{\mathrm{d}t} (\delta u_i^{\alpha} \dot{u}_i^{\alpha}) \mathrm{d}t} - \int \sum_{\alpha} m^{\alpha} \delta u_i^{\alpha} \ddot{u}_i^{\alpha} \mathrm{d}t$$

$$- \int \sum_{\beta} \delta u_i^{\alpha} \left(A_j^{\beta\alpha} C_{ijkl}^{\beta\alpha\alpha'} A_l^{\beta\alpha'} \right) \Psi^{\beta} u_k^{\alpha'} \mathrm{d}t$$

$$+ \int \sum_{\alpha} \hat{C}_{iljk}^{\alpha} \left(\sum_{\beta} S_l^{\alpha\beta} \dot{u}_{jk}^{\beta} \right) \Phi^{\alpha} \delta u_i^{\alpha} \mathrm{d}t = 0$$

$$\int \sum_{\alpha} \left(m^{\alpha} \ddot{u}_i^{\alpha} + \sum_{\beta} \left(A_j^{\beta\alpha} C_{ijkl}^{\beta\alpha\alpha'} A_l^{\beta\alpha'} \right) \Psi^{\beta} u_k^{\alpha'} - \hat{C}_{iljk}^{\alpha} \left(\sum_{\beta} S_l^{\alpha\beta} \dot{u}_{jk}^{\beta} \right) \Phi^{\alpha} \right) \delta u_i^{\alpha} \mathrm{d}t = 0$$

$$\int \sum_{\alpha} \left(m^{\alpha} \ddot{u}_i^{\alpha} + \sum_{\beta} \left(A_j^{\beta\alpha} C_{ijkl}^{\beta\alpha\alpha'} A_l^{\beta\alpha'} \right) \Psi^{\beta} u_k^{\alpha'} - \hat{C}_{iljk}^{\alpha} \left(\sum_{\beta} S_l^{\alpha\beta} \left(\sum_{\alpha'} A_k^{\beta\alpha'} \dot{u}_j^{\alpha'} \right) \right) \Phi^{\alpha} \right) \delta u_i^{\alpha} \mathrm{d}t = 0$$

The above should hold for compatible arbitrary variation of u_i^{α}, δu_i^{α}. Therefore, the following should hold.

$$m^{\alpha} \ddot{u}_i^{\alpha} + \sum_{\beta} \left(A_j^{\beta\alpha'} C_{ijkl}^{\beta\alpha'\alpha} A_l^{\beta\alpha} \Psi^{\beta} \right) u_k^{\alpha} - \sum_{\beta} \left(\hat{C}_{iljk}^{\alpha'} S_l^{\alpha'\beta} \sum_{\alpha} A_k^{\beta\alpha} \Phi^{\alpha'} \right) \dot{u}_j^{\alpha} = 0$$

This is the governing linear set of equation of PDS-FEM. Note that the last term includes the damping effect.

6.3 Numerical experiment for the rotational damping

To see the effect of the damping term, the a PDS-FEM based stone brick wall is constructed as shown in Figure 6.1. Brick wall is constructed following the experiments reported by Elmenshawi et al.[30]. However, the brick wall model in this research is regularly arranged unlike the stone brick wall tested by Elmenshawi et al.[30] which is irregular. The width, high and thickness of the bricks are 0.4m, 0.135m and 0.27m, respectively. Accoding to the experimental investigation, stiffness k and h are set to be $2.03\times10^{10}\mathrm{N/m^3}$ and $4.69\times10^{8}\mathrm{N/m^3}$, respectively. The block density is assumed to be $2650\mathrm{kg/m^3}$.

To see the effect of change in ω_0, the ω_0 is varied to be 0 to $0.8\omega_{\text{spin}}$ where the ω_{spin} is the rotational wave frequency for relatively long wavelength. ω_{spin} can be determined for given spring constants, brick size and brick density by Eq. 4.23. In this experiments ω_{spin} are determined as 12617 rad/s.

The wall is subjected to 9N static input to produce initial deformation. Once the static input is released, the wall will vibrate freely.

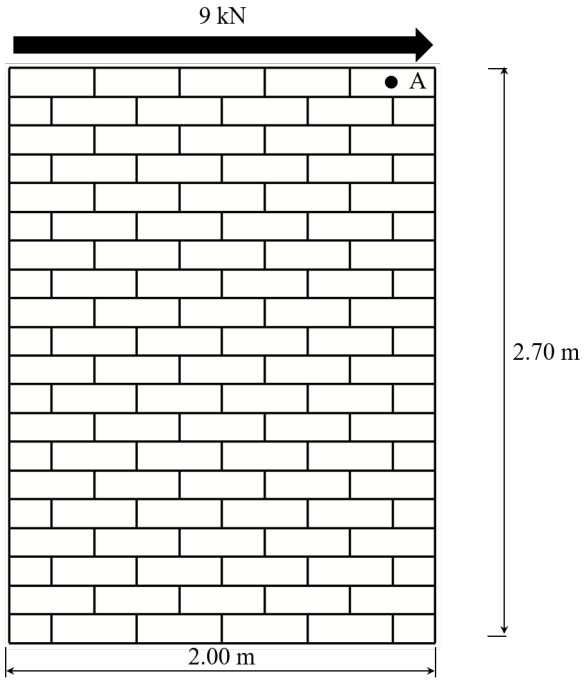

Figure 6.1: Brick wall model for rotational damped system.

6.3.1 Energy of the free vibrating wall

Figure 6.2 shows the energy of the free vibrating wall where for different ω_0. For $\omega_0=0$, the energy of the system conserved because the value of damping term of this case is zero. This conservation of the energy of the undamped system indirectly indicate the correctness of the numerical code. For the $\omega_0=0.2\omega_{\text{spin}}$ to $\omega_0=0.8\omega$, it is seen that the energies slowly dissipate due to the damping

term. Also, it is observed that the energy in the initial state are different for different ω_0. This is because the ω_0 also affects the stiffness of the system.

It is seen that the dissipation of the energy of the system is low. This might because rotational damping term may not fully damp the system. Note that the high frequency rotation is one of the many causes of the damping.

There are another possible reason for low dissipation. The approximation is based on the continuumnization which provide poor range of applicability since r-wave is applicable for $\xi a_i{=}0$ or $\omega{=}\omega_{\text{spin}}$ (see 4.4.3.1). However, ω_0 form 0 to 0.8ω which are not in the applicable range is used since $\omega_0{=}\omega_{\text{spin}}$ or nearly equal cannot be used since it makes G and G' undefined.

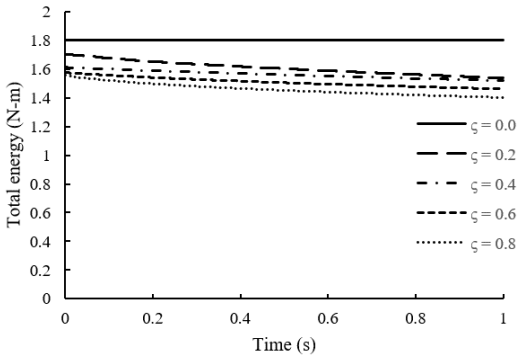

Figure 6.2: Total energy of the stone brick wall with different ω_0 where $\varsigma{=}\omega_0/\omega_{\text{spin}}$.

6.3.2 Vibration of the damped system

Figure 6.3 shows the acceleration of the brick and point A with different ω_0. Like the energy dissipation of the corresponding ω_0, it is seen that the decay of the amplitude is small although the ω_0 is up to $0.8\omega_{\text{spin}}$. Unlike the experimental observation reported by Elmenshawi et al.[30], the numerical result shows high frequency acceleration while the frequency of about 11 Hz recorded in the experimental observation. This may because the resolution of the accelerometer used in the experiment is low. However, according to the translation in the numerical experiment in Figure 6.4, frequency of translation is about 14 Hz which is a little bit higher than that of experimental observation reported by Elmenshawi et al.[30].

6.4 Summary

This chapter expresses role of rotation on damping mechanism of brick wall systems since there is the hypothesis that the high frequency rotation could be one of sources of damping in brick structures[1]. To obtain a rational damping term due rotation, the rotation in the continuumnized equation of translation is replaced by the approximated rotation in term of translation in the equation of rotation. With this approach, the equation of translation which include damping term is obtained.

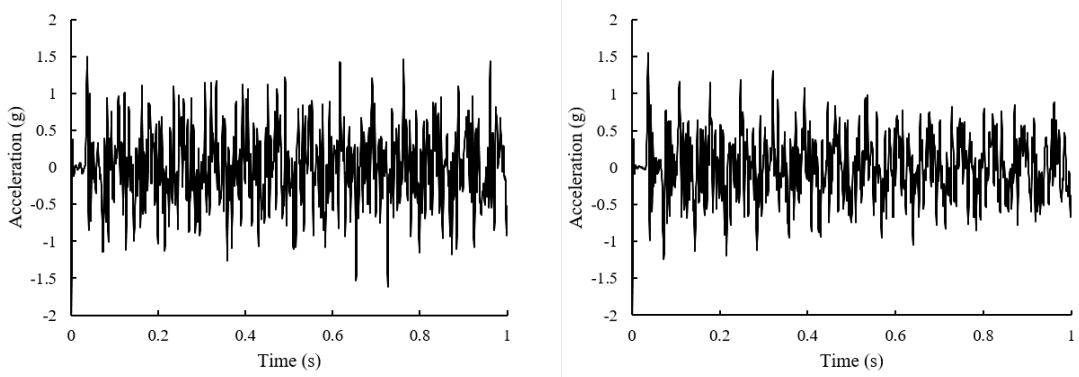

(a) $\omega_0 = 0$ (b) $\omega_0 = 0.2\omega_{\text{spin}}$

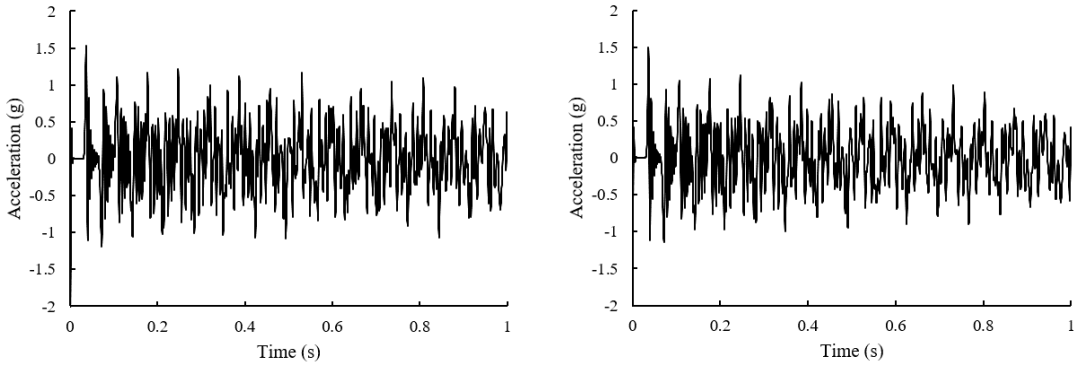

(c) $\omega_0 = 0.4\omega_{\text{spin}}$ (d) $\omega_0 = 0.6\omega_{\text{spin}}$

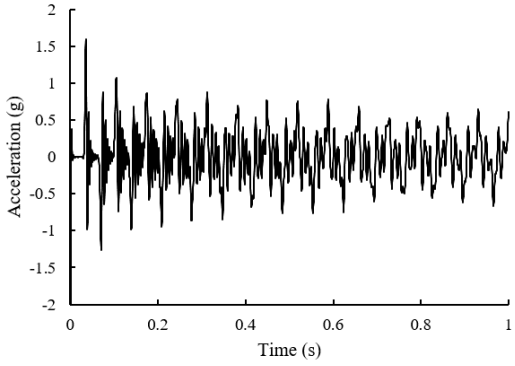

(e) $\omega_0 = 0.8\omega_{\text{spin}}$

Figure 6.3: Horizontal acceleration at point A with different ω_0.

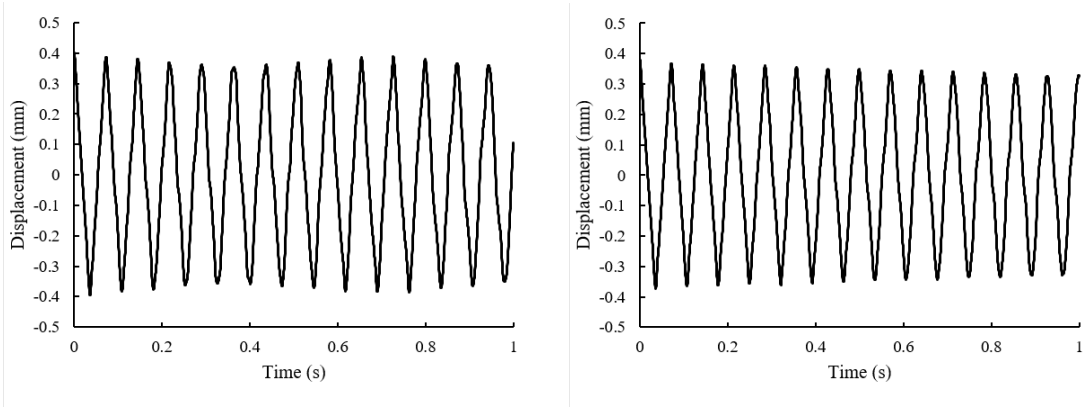

(a) $\omega_0 = 0$

(b) $\omega_0 = 0.2\omega_{\text{spin}}$

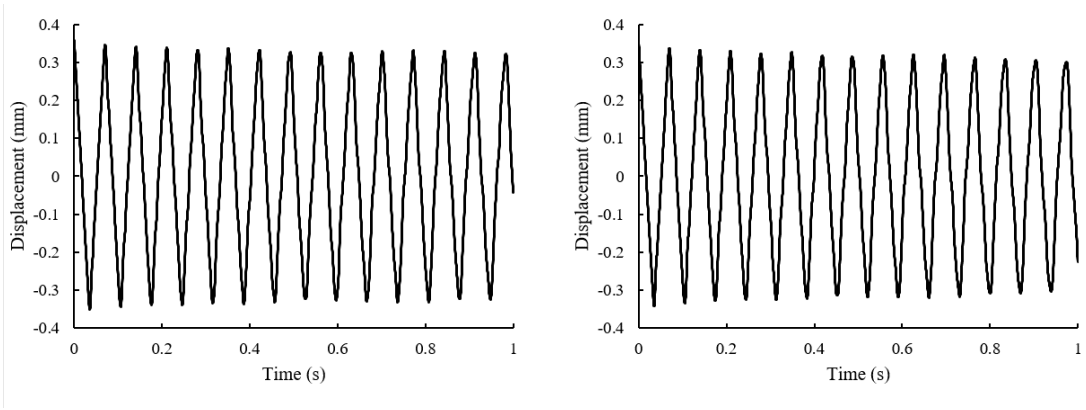

(c) $\omega_0 = 0.4\omega_{\text{spin}}$

(d) $\omega_0 = 0.6\omega_{\text{spin}}$

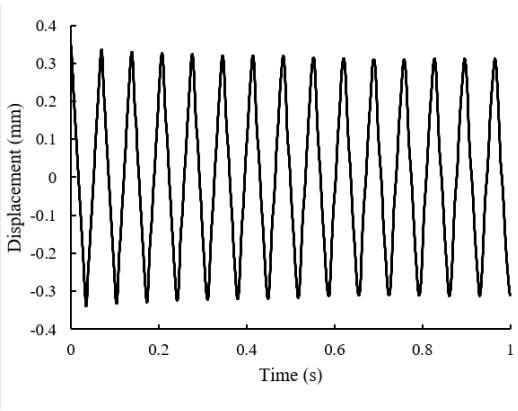

(e) $\omega_0 = 0.8\omega_{\text{spin}}$

Figure 6.4: Horizontal displacement at point A with different ω_0.

According to the numerical experiment free vibration brick wall with damping term described above, the dissipation of energy is observed. This can conclude that the high frequency rotation can be one of the sources of damping. However, large energy dissipation cannot be obtained although ω_0 is up to $0.8\omega_{\mathrm{spin}}$ are tested. This might because r-wave in continuumnization is applicable for $\omega_0 = \omega_{\mathrm{spin}}$. However, using $\omega_0 = \omega_{\mathrm{spin}}$ cause some variables undefined.

Chapter 7

Concluding remarks

7.1 Summary and conclusion

In this research, continuumnization of brick wall is developed for and applied for several applications. Based on the continuumnization, the governing equations of regularly brick mass-spring systems are approximated to be an equivalent continuum form assuming that wavelength is relatively long compared to brick size. The obtained continuum form based on the continuumnization is called continuuumnzied governing equations.

One of the benefits of the continuumnization the governing equations of rigid particle mass-spring systems can be analytically solved. In this research, analytical frequency-wavenumber relation of primary wave (p-wave), shear wave (s-wave), and rotational wave (r-wave) of in-plane single layer brick wall are obtained. Furthermore, we obtain analytical predicted p- and s- wave speeds. Note that regularity packed brick wall are predicts as anisotropic since the p- and s-wave speed depend on the direction of the wave propagation.

An advantaged of the predicted dynamic characteristics described above is that we can use them to verify simulations of discrete models. In this research, the predicted dynamic characteristics are verified with rigid body spring model (RBSM) to see their range of applicability. For time domain comparison, the numerical p-and s-wavefronts are in good agreement with their corresponding analytically predicted wavefronts. For frequency domain, the continuumnization provided good prediction for s-wave frequency. However, it is not suitable to compare rotational wave frequency as the numerical and analytical result are rapidly diverse for $|\xi a_i| > 0$ where ξ is the wave number and a_i is the half of brick sizes in i^{th} direction.

Apart from the continuumnization, the equivalent continuous governing equations and the dynamic characteristics can be analytically obtained by the second order Taylor's expansion (CFSTE). Unlike continuumnization, this approaches provides second order approximation of rotation. Thus, CFSTE provides better prediction of r-wave frequency. The predicted frequency-wavenumber relation based on CFSTE is applicable for wave length 7 times longer that brick sizes which is sufficient for civil engineering application.

Further, the range of applicability can be extended using continuum form based on infinite series (CFIS). Though it is inconvenient for finite element model (FEM) implementation, CFIS provides wider applicable range for verification propose than that of continuumnzation and CFSTE. CFIS is applicable for wave length 2 times longer that brick sizes which is the shortest meaningful of the wavelength in discrete particle systems.

One another application of the continuumnization is that we can formulated FEM for brick structures which is simple to use in commercial software. In this research, PDS-FEM is implemented as a brick-wall itself is a set of block particles. According to the verification of PDS-FEM with the analytical prediction, PDS-FEM is applicable for wavelength 7 times longer than the size of bricks which is sufficient for civil engineering applications.

According to the numerical results of PDS-FEM, high frequency is observed. As that such high frequency does not appear in practices, it is possible to be one of the source of damping. To see the invert force due to rotation, this research approximates rotation in term of translation in the equation of rotation and substituted into the equation of translation. With this approximation, equation of translation with damping term is obtained.

To see the effect of damping term, a PDS-FEM based brick wall is constructed and simulated. According to the simulation of free vibration brick wall, though the decay of vibration is not clearly seen, small dissipation of energy of the system is observed. This conclude that the high frequency vibration can cause damping in brick structure.

7.2 Future work

For the Continuumnization based, PDS-FEM, one can be expand into 3d for more general application, especially for historical structures. Also, with the continuumnization PDS-FEM, we can further study cracking and nonlinear behavior of brick structures.

Damping mechanism of brick structures should be further investigated since the energy dissipation is small and the decay of vibration amplitude is not clearly seen. There are some possible reason about this behavior. The damped governing equation is based on the continuumnzation which provides very narrow range of applicability for r-wave (Only for $|\xi a_i|$ very closes to 0) while the system might content wavelengths which are not in that range. Another possible reason is that the damping due to high frequency rotation may not be able to fully damp the system. It is important to note that there are other source of damping, such as friction in mortar or micro crack in brick or mortar.

Appendix A

Geometry of each vectors

Table A.1 and A.2 express the unit vectors $\boldsymbol{n}^{\gamma+}$,$\boldsymbol{t}^{\gamma+}$,$\boldsymbol{s}^{\gamma+}$, and $\boldsymbol{r}^{\gamma+}$ of spheral systems and brick systems expressed in chapter 3 and 4, respectively. $\boldsymbol{n}^{\gamma\pm}$ are shown in Figure A.1 and A.2.

Vector in $\gamma-$ can be determined as $\boldsymbol{n}^{\gamma-}=-\boldsymbol{n}^{\gamma+}$,$\boldsymbol{t}^{\gamma-}=-\boldsymbol{t}^{\gamma+}$,$\boldsymbol{s}^{\gamma-}=\boldsymbol{s}^{\gamma+}$, and $\boldsymbol{r}^{\gamma-}=-\boldsymbol{r}^{\gamma+}$.

A.1 Sphere

γ	1	2	3
$\boldsymbol{n}^{\gamma+}$	$\boldsymbol{e}_1$	$-\frac{1}{2}\boldsymbol{e}_1+\frac{\sqrt{3}}{2}\boldsymbol{e}_2$	$-\frac{1}{2}\boldsymbol{e}_1-\frac{\sqrt{3}}{2}\boldsymbol{e}_2$
$\boldsymbol{t}^{\gamma+}$	$\boldsymbol{e}_2$	$-\frac{\sqrt{3}}{2}\boldsymbol{e}_1-\frac{1}{2}\boldsymbol{e}_2$	$\frac{\sqrt{3}}{2}\boldsymbol{e}_1-\frac{1}{2}\boldsymbol{e}_2$
$\boldsymbol{s}^{\gamma+}$	$\boldsymbol{e}_3$	$\boldsymbol{e}_3$	$\boldsymbol{e}_3$

Table A.1: unit vecters of 2d sphrical system

A.2 Brick

	neighbor 1	neighbor 2	neighbor 3
$\boldsymbol{n}^{\gamma+}$	$\boldsymbol{e}_1$	$\boldsymbol{e}_2$	$\boldsymbol{e}_2$
$\boldsymbol{t}^{\gamma+}$	$\boldsymbol{e}_2$	$-\boldsymbol{e}_1$	$-\boldsymbol{e}_1$
$\boldsymbol{s}^{\gamma+}$	$\boldsymbol{e}_3$	$\boldsymbol{e}_3$	$\boldsymbol{e}_3$
$\boldsymbol{r}^{\gamma+}$	$a_1\boldsymbol{e}_1$	$\frac{a_1}{2}\boldsymbol{e}_1+a_2\boldsymbol{e}_2$	$-\frac{a_1}{2}\boldsymbol{e}_1+a_2\boldsymbol{e}_2$

Table A.2: unit vecters of 2d brick system

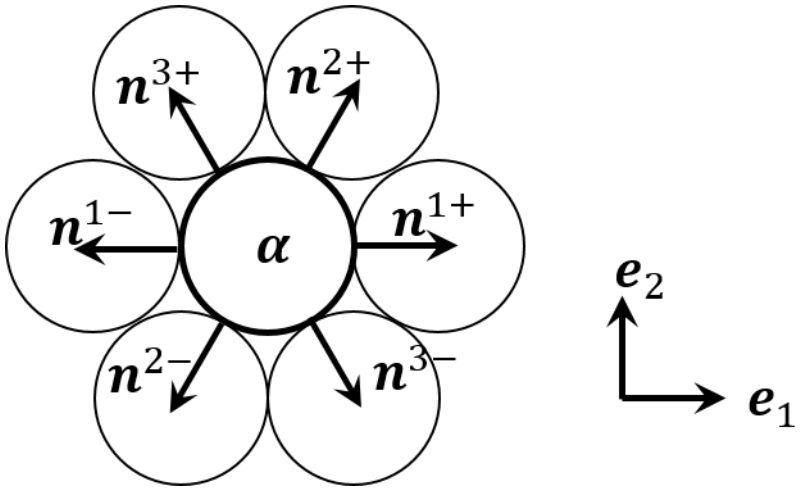

Figure A.1: $n^{\gamma\pm}$ vectors on the contact points of sphere α.

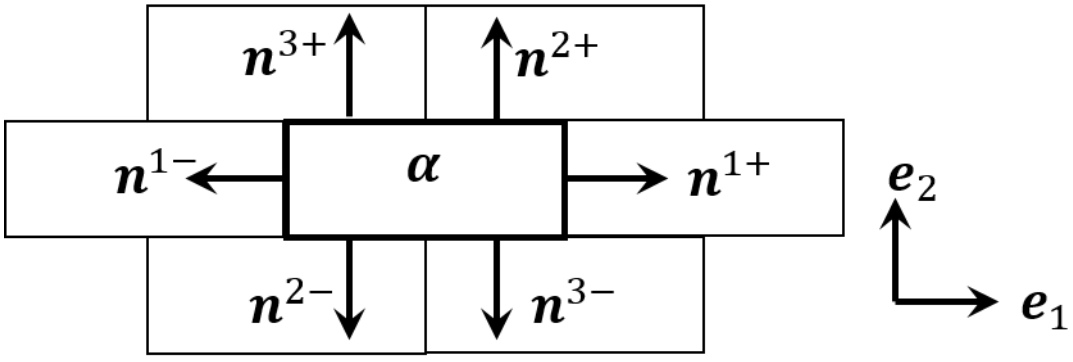

Figure A.2: $n^{\gamma\pm}$ vectors on the contact areas of brick α.

Appendix B

Non-zero components

This appendix consists of the non-zero components of tensors in continuous governing equations for hexagonally packed spherical mass spring systems Eq. 3.14

B.1 Sphere

The following contents are the component in Eq. 3.14 and 3.22.

$$
\begin{aligned}
c_{1111} &= c_{2222} = \frac{9k}{8a} + \frac{3h}{8a} \\
c_{1212} &= c_{2121} = \frac{3k}{8a} + \frac{9h}{8a} \\
c_{1122} &= c_{1221} = c_{2112} = c_{2121} = \frac{3k}{8a} - \frac{3h}{8a} \\
q_{123} &= -\frac{3h}{2a} \\
q_{213} &= \frac{3h}{2a} \\
d_{33} &= \frac{3h}{2a} \\
v_{1313} &= v_{2323} = -\frac{3h}{2a}
\end{aligned}
$$

B.2 Brick

The following contents are the component in Eq. 4.10 and 4.19

$$
\begin{aligned}
c_{1111} &= \frac{a_1}{2}\left(4k+\frac{ha_1}{a_2}\right) \\
c_{1212} &= \frac{a_1}{2}\left(4h+\frac{ka_1}{a_2}\right) \\
c_{2121} &= 2ha_2 \\
c_{2222} &= 2ka_2 \\
q_{123} &= -2ha_2 \\
q_{213} &= \frac{a_1}{2}\left(4h+\frac{ka_1}{a_2}\right) \\
d_{33} &= 2ha_1+\frac{ka_1^2}{2a_2}+2ha_2 \\
v_{1313} &= \frac{a_1^2}{8}\left(16ha_1+\frac{ka_1^2}{a_2}+4ha_2\right)-\frac{ka_1}{24a_2}\left(a_1^3+16a_2^3\right) \\
v_{2323} &= \frac{a_1}{3}ka_1^2a_2+2ha_2
\end{aligned}
$$

Appendix C

Characteristic equations based on infinite series

This appendix presents the formation of the characteristic equations based on infinite series Taylor's expansion (ISC) for spherical mass spring systems and brick mass spring systems.

C.1 Spherical mass-spring systems

Taylor expansion of a function $f(\boldsymbol{x})$ about a point $\boldsymbol{x}^0$; let $\boldsymbol{x}=\boldsymbol{x}^0+a\boldsymbol{n}^\gamma$.

$$f(\boldsymbol{x}) = f(\boldsymbol{x^0})+\frac{\partial f(\boldsymbol{x})}{\partial x_i}\bigg|_{\boldsymbol{x}^0} n_i^\gamma a+\frac{\partial^2 f(\boldsymbol{x})}{\partial x_i\partial x_j}\bigg|_{\boldsymbol{x}^0} n_i^\gamma n_j^\gamma \frac{a^2}{2!}+\ldots$$

Based on the above results, the following two expressions can be obtained.

$$\begin{aligned} f(\boldsymbol{x}+2\alpha\boldsymbol{n}^\gamma) &= f(\boldsymbol{x})+\frac{\partial f(\boldsymbol{x})}{\partial x_i}n_i^\gamma(2a)+\frac{\partial^2 f(\boldsymbol{x})}{\partial x_i\partial x_j}n_i^\gamma n_j^\gamma\frac{(2a)^2}{2!}+\frac{\partial^3 f(\boldsymbol{x})}{\partial x_i\partial x_j\partial x_k}n_i^\gamma n_j^\gamma n_k^\gamma\frac{(2a)^3}{3!}+\ldots \\ f(\boldsymbol{x}-2a\boldsymbol{n}^\gamma) &= f(\boldsymbol{x})+\frac{\partial f(\boldsymbol{x})}{\partial x_i}n_i^\gamma(-2a)+\frac{\partial^2 f(\boldsymbol{x})}{\partial x_i\partial x_j}n_i^\gamma n_j^\gamma\frac{(-2a)^2}{2!}+\frac{\partial^3 f(\boldsymbol{x})}{\partial x_i\partial x_j\partial x_k}n_i^\gamma n_j^\gamma n_k^\gamma\frac{(-2a)^3}{3!}+\ldots \end{aligned}$$

For the sake of brevity, let's use the notation $\boldsymbol{x}^{\gamma\pm}=\boldsymbol{x}\pm2\alpha\boldsymbol{n}^\gamma$. Addition and subtraction of the above two provide

$$f(\boldsymbol{x}^{\gamma+})+f(\boldsymbol{x}^{\gamma-}) = 2\left[f(\boldsymbol{x})+\frac{\partial^2 f(\boldsymbol{x})}{\partial x_i\partial x_j}n_i^\gamma n_j^\gamma\frac{(2a)^2}{2!}+\frac{\partial^4 f(\boldsymbol{x})}{\partial x_i\partial x_j\partial x_k\partial x_l}n_i^\gamma n_j^\gamma n_k^\gamma n_l^\gamma\frac{(2a)^4}{4!}+\ldots\right] \quad \text{(C.1)}$$

$$f(\boldsymbol{x}^{\gamma+})-f(\boldsymbol{x}^{\gamma-}) = 2\left[\frac{\partial f(\boldsymbol{x})}{\partial x_i}n_i^\gamma 2a+\frac{\partial^3 f(\boldsymbol{x})}{\partial x_i\partial x_j\partial x_k}n_i^\gamma n_j^\gamma n_k^\gamma\frac{(2a)^3}{3!}+\ldots\right]. \quad \text{(C.2)}$$

Fourier transforms of $f(\boldsymbol{x}+2a\boldsymbol{n}^\gamma)\pm f(\boldsymbol{x}-2a\boldsymbol{n}^\gamma)$

Let $\mathcal{F}(f(\boldsymbol{x},t))$ denote the Fourier transform of a function $f(\boldsymbol{x},t)$ with respect to space and time dimensions; i.e. $\mathcal{F}(f(\boldsymbol{x},t))=\int\cdots\int_\infty^\infty f(\boldsymbol{x},t)e^{\imath(\boldsymbol{\xi}\cdot\boldsymbol{x}-\omega t)}d\boldsymbol{x}dt$. Fourier transform of the Eq. C.1 gives

$$\begin{aligned}
\mathcal{F}\big(f(\boldsymbol{x}^{\gamma+},t)+f(\boldsymbol{x}^{\gamma-},t)\big) &= 2\mathcal{F}\left(f(\boldsymbol{x})+\frac{\partial^2 f(\boldsymbol{x})}{\partial x_i\partial x_j}n_i^\gamma n_j^\gamma\frac{(2a)^2}{2!}+\frac{\partial^4 f(\boldsymbol{x})}{\partial x_i\partial x_j\partial x_k\partial x_l}n_i^\gamma n_j^\gamma n_k^\gamma n_l^\gamma\frac{(2a)^4}{4!}+\ldots\right)\\
&= 2\left(1+\frac{(2a\imath\boldsymbol{\xi}\cdot\boldsymbol{n}^\gamma)^2}{2!}+\frac{(2a\imath\boldsymbol{\xi}\cdot\boldsymbol{n}^\gamma)^4}{4!}+\frac{(2a\imath\boldsymbol{\xi}\cdot\boldsymbol{n}^\gamma)^6}{6!}+\frac{(2a\imath\boldsymbol{\xi}\cdot\boldsymbol{n}^\gamma)^8}{8!}+\ldots\right)\tilde{f}(\boldsymbol{\xi},\omega)\\
&= 2\left(1-\frac{(2a\boldsymbol{\xi}\cdot\boldsymbol{n}^\gamma)^2}{2!}+\frac{(2a\boldsymbol{\xi}\cdot\boldsymbol{n}^\gamma)^4}{4!}-\frac{(2a\boldsymbol{\xi}\cdot\boldsymbol{n}^\gamma)^6}{6!}+\frac{(2a\boldsymbol{\xi}\cdot\boldsymbol{n}^\gamma)^8}{8!}-\ldots\right)\tilde{f}(\boldsymbol{\xi},\omega)\\
&= 2\cos(2a\boldsymbol{\xi}\cdot\boldsymbol{n}^\gamma)\tilde{f}(\boldsymbol{\xi},\omega) \qquad \text{(C.3)}\\
\mathcal{F}\big(f(\boldsymbol{x}^{\gamma+},t)+f(\boldsymbol{x}^{\gamma-},t)\big) &= \big(2-4\sin^2(a\boldsymbol{\xi}\cdot\boldsymbol{n}^\gamma)\big)\tilde{f}(\boldsymbol{\xi},\omega). \qquad \text{(C.4)}
\end{aligned}$$

Similarly, Fourier transform of the Eq. C.2 gives

$$\begin{aligned}
\mathcal{F}\big(f(\boldsymbol{x}^{\gamma+},t)-f(\boldsymbol{x}^{\gamma-},t)\big) &= 2\mathcal{F}\left(\frac{\partial f(\boldsymbol{x})}{\partial x_i}n_i^\gamma 2a+\frac{\partial^3 f(\boldsymbol{x})}{\partial x_i\partial x_j\partial x_k}n_i^\gamma n_j^\gamma n_k^\gamma\frac{(2a)^3}{3!}+\ldots\right)\\
&= 2\left(\frac{(2a\imath\boldsymbol{\xi}\cdot\boldsymbol{n}^\gamma)}{1!}+\frac{(2a\imath\boldsymbol{\xi}\cdot\boldsymbol{n}^\gamma)^3}{3!}+\frac{(2a\imath\boldsymbol{\xi}\cdot\boldsymbol{n}^\gamma)^5}{5!}+\frac{(2a\imath\boldsymbol{\xi}\cdot\boldsymbol{n}^\gamma)^7}{7!}+\ldots\right)\tilde{f}(\boldsymbol{\xi},\omega)\\
&= 2\imath\left(\frac{(2a\boldsymbol{\xi}\cdot\boldsymbol{n}^\gamma)}{1!}-\frac{(2a\boldsymbol{\xi}\cdot\boldsymbol{n}^\gamma)^3}{3!}+\frac{(2a\boldsymbol{\xi}\cdot\boldsymbol{n}^\gamma)^5}{5!}-\frac{(2a\boldsymbol{\xi}\cdot\boldsymbol{n}^\gamma)^7}{7!}+\ldots\right)\tilde{f}(\boldsymbol{\xi},\omega)\\
\mathcal{F}\big(f(\boldsymbol{x}^{\gamma+},t)-f(\boldsymbol{x}^{\gamma-},t)\big) &= 2e^{\imath\pi/2}\sin(2a\boldsymbol{\xi}\cdot\boldsymbol{n}^\gamma)\tilde{f}(\boldsymbol{\xi},\omega) \qquad \text{(C.5)}
\end{aligned}$$

For translational components

Governing equations of translational component u_i for the spherical-mass spring systems

$$m\ddot{u}_i^\mu=\sum_\gamma K_{ij}^\gamma\left(u_j^{\gamma+}-2u_j^\mu+u_j^{\gamma-}\right)-\sum_\gamma\hat{K}_{ij}^\gamma\left(\theta_j^{\gamma+}-\theta_j^{\gamma-}\right)$$

Taking the Fourier transform of the above equation, and using Eq. C.4 and Eq. C.5, we can obtain

$$-m\omega^2\tilde{u}_i(\boldsymbol{\xi},\omega)+\sum_\gamma K_{ij}^\gamma\left(4\sin^2(a\boldsymbol{\xi}\cdot\boldsymbol{n}^\gamma)\right)\tilde{u}_j(\boldsymbol{\xi},\omega)+\sum_\gamma\hat{K}_{ij}^\gamma\left(2e^{\imath\pi/2}\sin(2a\boldsymbol{\xi}\cdot\boldsymbol{n}^\gamma)\right)\tilde{\theta}_j(\boldsymbol{\xi},\omega)=0$$

For rotational components

Governing equations of rotational component θ_i for the spherical-mass spring system

$$I\ddot{\theta}_i^{\mu} = -\sum_{\gamma}\hat{K}_{ji}^{\gamma}\left(u_j^{\gamma+}-u_j^{\gamma-}\right)-\sum_{\gamma}\bar{K}_{ij}^{\gamma}\left(\theta_j^{\gamma+}+\theta_j^{\gamma-}+2\theta_j^{\mu}\right)$$

Just as the above, taking the Fourier transform and using Eq. C.4 and Eq. C.5, we get

$$-I\omega^2\tilde{\theta}_i(\boldsymbol{\xi},\omega)+\sum_{\gamma}\hat{K}_{ji}^{\gamma}\left(2e^{\imath\pi/2}\sin(2a\boldsymbol{\xi}\cdot\boldsymbol{n}^{\gamma})\right)\tilde{u}_j(\boldsymbol{\xi},\omega)+ha^2\sum_{\gamma}\bar{K}_{ij}^{\gamma}\left(4\cos^2(a\boldsymbol{\xi}\cdot\boldsymbol{n}^{\gamma})\right)\tilde{\theta}_j(\boldsymbol{\xi},\omega) = 0$$

Characteristic equation

The above set of equations in Fourier domain can be written in the follwoing matrix form

$$\begin{bmatrix} 4\sum_{\gamma}K_{ij}^{\gamma}\sin^2(a\boldsymbol{\xi}\cdot\boldsymbol{n}^{\gamma})-\boldsymbol{m}\omega^2 & 2e^{\imath\pi/2}\sum_{\gamma}\hat{K}_{ij}^{\gamma}\sin(2a\boldsymbol{\xi}\cdot\boldsymbol{n}^{\gamma}) \\ 2e^{\imath\pi/2}\sum_{\gamma}\hat{K}_{ji}^{\gamma}\sin(2a\boldsymbol{\xi}\cdot\boldsymbol{n}^{\gamma}) & 4\sum_{\gamma}\bar{K}_{ij}^{\gamma}\cos^2(a\boldsymbol{\xi}\cdot\boldsymbol{n}^{\gamma})-\boldsymbol{I}\omega^2 \end{bmatrix}\begin{Bmatrix} \tilde{u}_j \\ \tilde{\theta}_j \end{Bmatrix} = \begin{Bmatrix} 0 \\ 0 \end{Bmatrix}$$

The above have non-trivial solutions when following charateristic equation is satisfied.

$$\det\begin{bmatrix} 4\sum_{\gamma}K_{ij}^{\gamma}\sin^2(a\boldsymbol{\xi}\cdot\boldsymbol{n}^{\gamma})-\boldsymbol{m}\omega^2 & 2e^{\imath\pi/2}\sum_{\gamma}\hat{K}_{ij}^{\gamma}\sin(2a\boldsymbol{\xi}\cdot\boldsymbol{n}^{\gamma}) \\ 2e^{\imath\pi/2}\sum_{\gamma}\hat{K}_{ji}^{\gamma}\sin(2a\boldsymbol{\xi}\cdot\boldsymbol{n}^{\gamma}) & 4\sum_{\gamma}\bar{K}_{ij}^{\gamma}\cos^2(a\boldsymbol{\xi}\cdot\boldsymbol{n}^{\gamma})-\boldsymbol{I}\omega^2 \end{bmatrix}=0 \tag{C.6}$$

For 2D systems, Eq.(C.6) can be expanded as.

$$\det\begin{bmatrix} 4\sum_{\gamma}K_{11}^{\gamma}\sin^2(a\boldsymbol{\xi}\cdot\boldsymbol{n}^{\gamma})-m\omega^2 & 4\sum_{\gamma}K_{12}^{\gamma}\sin^2(a\boldsymbol{\xi}\cdot\boldsymbol{n}^{\gamma}) & 2\sum_{\gamma}e^{\imath\pi/2}\hat{K}_{13}^{\gamma}\sin(2a\boldsymbol{\xi}\cdot\boldsymbol{n}^{\gamma}) \\ 4\sum_{\gamma}K_{21}^{\gamma}\sin^2(a\boldsymbol{\xi}\cdot\boldsymbol{n}^{\gamma}) & 4\sum_{\gamma}K_{22}^{\gamma}\sin^2(a\boldsymbol{\xi}\cdot\boldsymbol{n}^{\gamma})-m\omega^2 & 2\sum_{\gamma}e^{\imath\pi/2}\hat{K}_{23}^{\gamma}\sin(2a\boldsymbol{\xi}\cdot\boldsymbol{n}^{\gamma}) \\ 2\sum_{\gamma}e^{\imath\pi/2}\hat{K}_{31}^{\gamma}\sin(2a\boldsymbol{\xi}\cdot\boldsymbol{n}^{\gamma}) & 2\sum_{\gamma}e^{\imath\pi/2}\hat{K}_{32}^{\gamma}\sin(2a\boldsymbol{\xi}\cdot\boldsymbol{n}^{\gamma}) & 4\sum_{\gamma}\bar{K}_{33}^{\gamma}\cos^2(a\boldsymbol{\xi}\cdot\boldsymbol{n}^{\gamma})-I_{33}\omega^2 \end{bmatrix}=0 \tag{C.7}$$

C.2 Brick mass-spring systems

The formulation for brick-sprig system is the same as that for the spherical particle system presented above. Taylor expansion of a function $f(\boldsymbol{x})$ about a point $\boldsymbol{x}^0$; let $\boldsymbol{x}=\boldsymbol{x}^0+\boldsymbol{r}^{\gamma+}$.

$$f(\boldsymbol{x}) = f(\boldsymbol{x^0})+\left.\frac{\partial f(\boldsymbol{x})}{\partial x_i}\right|_{\boldsymbol{x}^0} r_i^{\gamma}+\left.\frac{\partial^2 f(\boldsymbol{x})}{\partial x_i\partial x_j}\right|_{\boldsymbol{x}^0} r_i^{\gamma}r_j^{\gamma}+\ldots$$

Based on the above results, the following two expressions can be obtained.

$$\begin{aligned} f(\boldsymbol{x}+2\boldsymbol{r}^{\gamma+}) &= f(\boldsymbol{x})+\frac{\partial f(\boldsymbol{x})}{\partial x_i}r_i^{\gamma}(2)+\frac{\partial^2 f(\boldsymbol{x})}{\partial x_i\partial x_j}r_i^{\gamma}r_j^{\gamma}\frac{(2)^2}{2!}+\frac{\partial^3 f(\boldsymbol{x})}{\partial x_i\partial x_j\partial x_k}r_i^{\gamma}r_j^{\gamma}r_k^{\gamma}\frac{(2)^3}{3!}+\ldots \\ f(\boldsymbol{x}-2\boldsymbol{r}^{\gamma}) &= f(\boldsymbol{x})+\frac{\partial f(\boldsymbol{x})}{\partial x_i}r_i^{\gamma}(-2)+\frac{\partial^2 f(\boldsymbol{x})}{\partial x_i\partial x_j}r_i^{\gamma}r_j^{\gamma}\frac{(-2)^2}{2!}+\frac{\partial^3 f(\boldsymbol{x})}{\partial x_i\partial x_j\partial x_k}r_i^{\gamma}r_j^{\gamma}r_k^{\gamma}\frac{(-2)^3}{3!}+\ldots \end{aligned}$$

For the sake of brevity, let's use the notation $\boldsymbol{x}^{\gamma\pm}=\boldsymbol{x}\pm 2\boldsymbol{r}^{\gamma}$Addition and subtraction of the above two provide

$$f(\boldsymbol{x}^{\gamma+})+f(\boldsymbol{x}^{\gamma-}) = 2\left[f(\boldsymbol{x})+\frac{\partial^2 f(\boldsymbol{x})}{\partial x_i\partial x_j}r_i^{\gamma}r_j^{\gamma}\frac{(2)^2}{2!}+\frac{\partial^4 f(\boldsymbol{x})}{\partial x_i\partial x_j\partial x_k\partial x_l}r_i^{\gamma}r_j^{\gamma}r_k^{\gamma}r_l^{\gamma}\frac{(2)^4}{4!}+\ldots\right] \quad \text{(C.8)}$$

$$f(\boldsymbol{x}^{\gamma+})-f(\boldsymbol{x}^{\gamma-}) = 2\left[\frac{\partial f(\boldsymbol{x})}{\partial x_i}r_i^{\gamma}(2)+\frac{\partial^3 f(\boldsymbol{x})}{\partial x_i\partial x_j\partial x_k}r_i^{\gamma}r_j^{\gamma}r_k^{\gamma}\frac{(2)^3}{3!}+\ldots\right]. \quad \text{(C.9)}$$

Fourier transforms of $f(\boldsymbol{x}+2\boldsymbol{r}^{\gamma})\pm f(\boldsymbol{x}-2a\boldsymbol{r}^{\gamma})$

Fourier transform of the Eq. C.8 gives

$$\begin{aligned} \mathcal{F}\big(f(\boldsymbol{x}^{\gamma+},t)+f(\boldsymbol{x}^{\gamma-},t)\big) &= 2\mathcal{F}\left(f(\boldsymbol{x})+\frac{\partial^2 f(\boldsymbol{x})}{\partial x_i\partial x_j}r_i^{\gamma}r_j^{\gamma}\frac{(2)^2}{2!}+\frac{\partial^4 f(\boldsymbol{x})}{\partial x_i\partial x_j\partial x_k\partial x_l}r_i^{\gamma}r_j^{\gamma}r_k^{\gamma}r_l^{\gamma}\frac{(2)^4}{4!}+\ldots\right) \\ &= 2\left(1+\frac{(2\imath\boldsymbol{\xi}\cdot\boldsymbol{r}^{\gamma})^2}{2!}+\frac{(2\imath\boldsymbol{\xi}\cdot\boldsymbol{r}^{\gamma})^4}{4!}+\frac{(2\imath\boldsymbol{\xi}\cdot\boldsymbol{r}^{\gamma})^6}{6!}+\frac{(2\imath\boldsymbol{\xi}\cdot\boldsymbol{r}^{\gamma})^8}{8!}+\ldots\right)\tilde{f}(\boldsymbol{\xi},\omega) \\ &= 2\left(1-\frac{(2\boldsymbol{\xi}\cdot\boldsymbol{r}^{\gamma})^2}{2!}+\frac{(2\boldsymbol{\xi}\cdot\boldsymbol{r}^{\gamma})^4}{4!}-\frac{(2\boldsymbol{\xi}\cdot\boldsymbol{r}^{\gamma})^6}{6!}+\frac{(2\boldsymbol{\xi}\cdot\boldsymbol{r}^{\gamma})^8}{8!}-\ldots\right)\tilde{f}(\boldsymbol{\xi},\omega) \\ &= 2\cos(2a\boldsymbol{\xi}\cdot\boldsymbol{r}^{\gamma})\,\tilde{f}(\boldsymbol{\xi},\omega) \quad \text{(C.10)} \\ \mathcal{F}\big(f(\boldsymbol{x}^{\gamma+},t)+f(\boldsymbol{x}^{\gamma-},t)\big) &= \big(2-4\sin^2(\boldsymbol{\xi}\cdot\boldsymbol{r}^{\gamma})\big)\,\tilde{f}(\boldsymbol{\xi},\omega). \quad \text{(C.11)} \end{aligned}$$

Similarly, Fourier transform of the Eq. C.9 gives

$$\begin{aligned} \mathcal{F}\big(f(\boldsymbol{x}^{\gamma+},t)-f(\boldsymbol{x}^{\gamma-},t)\big) &= 2\mathcal{F}\left(\frac{\partial f(\boldsymbol{x})}{\partial x_i}r_i^{\gamma}(2)+\frac{\partial^3 f(\boldsymbol{x})}{\partial x_i\partial x_j\partial x_k}r_i^{\gamma}r_j^{\gamma}r_k^{\gamma}\frac{(2)^3}{3!}+\ldots\right) \\ &= 2\left(\frac{(2\imath\boldsymbol{\xi}\cdot\boldsymbol{r}^{\gamma})}{1!}+\frac{(2\imath\boldsymbol{\xi}\cdot\boldsymbol{r}^{\gamma})^3}{3!}+\frac{(2\imath\boldsymbol{\xi}\cdot\boldsymbol{r}^{\gamma})^5}{5!}+\frac{(2\imath\boldsymbol{\xi}\cdot\boldsymbol{r}^{\gamma})^7}{7!}+\ldots\right)\tilde{f}(\boldsymbol{\xi},\omega) \\ &= 2\imath\left(\frac{(2\boldsymbol{\xi}\cdot\boldsymbol{r}^{\gamma})}{1!}-\frac{(2\boldsymbol{\xi}\cdot\boldsymbol{r}^{\gamma})^3}{3!}+\frac{(2\boldsymbol{\xi}\cdot\boldsymbol{r}^{\gamma})^5}{5!}-\frac{(2\boldsymbol{\xi}\cdot\boldsymbol{r}^{\gamma})^7}{7!}+\ldots\right)\tilde{f}(\boldsymbol{\xi},\omega) \\ \mathcal{F}\big(f(\boldsymbol{x}^{\gamma+},t)-f(\boldsymbol{x}^{\gamma-},t)\big) &= 2e^{\imath\pi/2}\sin(2\boldsymbol{\xi}\cdot\boldsymbol{r}^{\gamma})\tilde{f}(\boldsymbol{\xi},\omega) \quad \text{(C.12)} \end{aligned}$$

For translational components

Governing equations of translational component u_i for the spherical-mass spring systems

$$m\ddot{u}_i^{\mu}=\sum_{\gamma}K_{ij}^{\gamma}\left(u_j^{\gamma+}-2u_j^{\mu}+u_j^{\gamma-}\right)-\sum_{\gamma}\hat{K}_{ij}^{\gamma}\left(\theta_j^{\gamma+}-\theta_j^{\gamma-}\right)$$

Taking the Fourier transform of the above equation, and using Eq. C.11 and Eq. C.12, we can obtain

$$-m\omega^2\tilde{u}_i(\boldsymbol{\xi},\omega)+\sum_{\gamma}K_{ij}^{\gamma}\left(4\sin^2(\boldsymbol{\xi}\cdot\boldsymbol{r}^{\gamma})\right)\tilde{u}_j(\boldsymbol{\xi},\omega)+\sum_{\gamma}\hat{K}_{ij}^{\gamma}\left(2e^{\imath\pi/2}\sin(2\boldsymbol{\xi}\cdot\boldsymbol{r}^{\gamma})\right)\tilde{\theta}_j(\boldsymbol{\xi},\omega)=0$$

For rotational components

Governing equations of rotational component θ_i for the spherical-mass spring system

$$I_{ij}\ddot{\theta}_j^{\mu} = \sum_{\gamma}\hat{K}_{ji}^{\gamma}\left(u_j^{+}-u_j^{-}\right)-\sum_{\gamma}\bar{K}_{ij}^{\gamma}\left(\theta_j^{+}+2\theta_j^{\mu}+\theta_j^{-}\right)+\sum_{\gamma}\bar{\bar{K}}_{ij}^{\gamma}\left(\theta_j^{+}-2\theta_j^{\mu}+\theta_j^{-}\right)$$

Just as the above, taking the Fourier transform and using Eq. C.11 and Eq. C.12, we get

$$\begin{aligned}-I_{ij}\omega^2\tilde{\theta}_j(\boldsymbol{\xi},\omega)-\sum_{\gamma}\hat{K}_{ji}^{\gamma}\left(2e^{\imath\pi/2}\sin(2\boldsymbol{\xi}\cdot\boldsymbol{r}^{\gamma})\right)\tilde{u}_j(\boldsymbol{\xi},\omega)+\sum_{\gamma}\bar{K}_{ij}^{\gamma}\left(4\cos^2(\boldsymbol{\xi}\cdot\boldsymbol{r}^{\gamma})\right)\tilde{\theta}_j(\boldsymbol{\xi},\omega)&\\ +\sum_{\gamma}\bar{\bar{K}}_{ij}^{\gamma}\left(4\sin^2(\boldsymbol{\xi}\cdot\boldsymbol{r}^{\gamma})\right)\tilde{u}_j(\boldsymbol{\xi},\omega) &= 0\end{aligned}$$

Characteristic equation

The above set of equations in Fourier domain can be written in the follwoing matrix form

$$\begin{bmatrix} 4\sum_{\gamma}K_{ij}^{\gamma}\sin^2(\boldsymbol{\xi}\cdot\boldsymbol{r}^{\gamma})-\boldsymbol{m}\omega^2 & 2e^{\imath\pi/2}\sum_{\gamma}\hat{K}_{ij}^{\gamma}\sin(2\boldsymbol{\xi}\cdot\boldsymbol{r}^{\gamma}) \\ -2e^{\imath\pi/2}\sum_{\gamma}\hat{K}_{ji}^{\gamma}\sin(2\boldsymbol{\xi}\cdot\boldsymbol{r}^{\gamma}) & 4\sum_{\gamma}\bar{K}_{ij}^{\gamma}\cos^2(\boldsymbol{\xi}\cdot\boldsymbol{r}^{\gamma})+4\sum_{\gamma}\bar{\bar{K}}_{ij}^{\gamma}\sin^2(\boldsymbol{\xi}\cdot\boldsymbol{r}^{\gamma})-\boldsymbol{I}\omega^2 \end{bmatrix} \begin{Bmatrix} \tilde{u}_j \\ \tilde{\theta}_j \end{Bmatrix} = \begin{Bmatrix} 0 \\ 0 \end{Bmatrix}$$

The above have non-trivial solutions when following charateristic equation is satisfied.

$$\det\begin{bmatrix} 4\sum_{\gamma}K_{ij}^{\gamma}\sin^2(\boldsymbol{\xi}\cdot\boldsymbol{r}^{\gamma})-\boldsymbol{m}\omega^2 & 2e^{\imath\pi/2}\sum_{\gamma}\hat{K}_{ij}^{\gamma}\sin(2\boldsymbol{\xi}\cdot\boldsymbol{r}^{\gamma}) \\ -2e^{\imath\pi/2}\sum_{\gamma}\hat{K}_{ji}^{\gamma}\sin(2\boldsymbol{\xi}\cdot\boldsymbol{r}^{\gamma}) & 4\sum_{\gamma}\bar{K}_{ij}^{\gamma}\cos^2(\boldsymbol{\xi}\cdot\boldsymbol{r}^{\gamma})+4\sum_{\gamma}\bar{\bar{K}}_{ij}^{\gamma}\sin^2(\boldsymbol{\xi}\cdot\boldsymbol{r}^{\gamma})-\boldsymbol{I}\omega^2 \end{bmatrix}=0 \qquad \text{(C.13)}$$

For 2D systems, Eq. C.13 can be expanded as.

$$\det\begin{bmatrix} 4\sum_{\gamma}K_{11}^{\gamma}\sin^2(\boldsymbol{\xi}\cdot\boldsymbol{r}^{\gamma})-m\omega^2 & 4\sum_{\gamma}K_{12}^{\gamma}\sin^2(\boldsymbol{\xi}\cdot\boldsymbol{r}^{\gamma}) & 2\sum_{\gamma}e^{\imath\pi/2}\hat{K}_{13}^{\gamma}\sin(2\boldsymbol{\xi}\cdot\boldsymbol{r}^{\gamma}) \\ 4\sum_{\gamma}K_{21}^{\gamma}\sin^2(\boldsymbol{\xi}\cdot\boldsymbol{r}^{\gamma}) & 4\sum_{\gamma}K_{22}^{\gamma}\sin^2(\boldsymbol{\xi}\cdot\boldsymbol{r}^{\gamma})-m\omega^2 & 2\sum_{\gamma}e^{\imath\pi/2}\hat{K}_{23}^{\gamma}\sin(2\boldsymbol{\xi}\cdot\boldsymbol{r}^{\gamma}) \\ -2\sum_{\gamma}e^{\imath\pi/2}\hat{K}_{31}^{\gamma}\sin(2\boldsymbol{\xi}\cdot\boldsymbol{r}^{\gamma}) & -2\sum_{\gamma}e^{\imath\pi/2}\hat{K}_{32}^{\gamma}\sin(2\boldsymbol{\xi}\cdot\boldsymbol{r}^{\gamma}) & A \end{bmatrix}=0 \tag{C.14}$$

where $A=4\sum_{\gamma}\bar{K}_{33}^{\gamma}\cos^2(\boldsymbol{\xi}\cdot\boldsymbol{r}^{\gamma})+4\sum_{\gamma}\bar{\bar{K}}_{33}^{\gamma}\sin^2(\boldsymbol{\xi}\cdot\boldsymbol{r}^{\gamma})-I_{33}\omega^2$.

Appendix D

Analytic expressions for PDS-FEM in 2D

This appendix presents the explicit expressions for implementing PDS-FEM for brick structures, in 2D settings. In 2D problems, the active DOFs are $\{u_1, u_2, \theta_3\}$. In deriving the stiffness matrices, we consider the triangle Ψ formed by connecting the centroids of the bricks Φ^1, Φ^2, Φ^3 shown in Figure D.1. $\bar{\boldsymbol{x}}$ is the point at which Φ^1, Φ^2 and Φ^3 meets each other.

D.1 First derivative

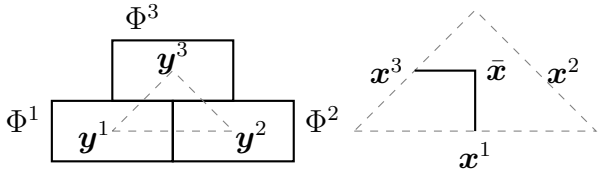

Figure D.1: Tessellation of 2D domain

D.1.1 $A_i^{\beta\alpha}$'s

From the Figure D.1 we can evaluate $A_i^{\beta\alpha}$ for $\Phi^a{=}\Phi^1$ as

$$\begin{aligned}\frac{1}{\Psi^\beta}\int_{\partial\Psi^\beta\cap\partial\Phi^1}\boldsymbol{n}^1 dl &= -\frac{1}{\Psi^\beta}\big((\boldsymbol{x}^2{-}\boldsymbol{x}^1){+}(\boldsymbol{x}^3{-}\boldsymbol{x}^2)\big){\times}\boldsymbol{k}\\ \boldsymbol{A}^{\beta 1} &= -\frac{1}{\Psi^\beta}(\boldsymbol{x}^3{-}\boldsymbol{x}^1){\times}\boldsymbol{k}.\end{aligned}$$

Ψ^β is the area of Ψ^β, while Φ^a's is that of Φ^a. In vector form, we can write $\boldsymbol{A}^{\beta 1}$ as

$$\left\{\begin{array}{c}A_1^{\beta 1}\\ A_2^{\beta 1}\end{array}\right\} = \frac{1}{\Psi^\beta}\left\{\begin{array}{c}-(x_2^3{-}x_2^1)\\ (x_1^3{-}x_1^1)\end{array}\right\}$$

$\boldsymbol{A}^{\beta 2}$ and $\boldsymbol{A}^{\beta 3}$ can be obtained by cyclic replacement of $\boldsymbol{x}^i$'s. as

$$\left\{ \begin{array}{c} A_1^{\beta 2} \\ A_2^{\beta 2} \end{array} \right\} = \frac{1}{\Psi^\beta} \left\{ \begin{array}{c} -(x_2^1 - x_2^2) \\ x_1^1 - x_1^2 \end{array} \right\}$$

$$\left\{ \begin{array}{c} A_1^{\beta 3} \\ A_2^{\beta 3} \end{array} \right\} = \frac{1}{\Psi^\beta} \left\{ \begin{array}{c} -(x_2^2 - x_2^3) \\ x_1^2 - x_1^3 \end{array} \right\}$$

Finally, for the sake of convenience, lets form the following matrix with $A_i^{\beta\alpha}$'s

$$\overline{\boldsymbol{A}}^{\beta\alpha} = \left[\begin{array}{cc} A_1^{\beta\alpha} & 0 \\ A_2^{\beta\alpha} & 0 \\ 0 & A_1^{\beta\alpha} \\ 0 & A_2^{\beta\alpha} \end{array} \right] \tag{D.1}$$

Now, we can express the coefficients involving the derivatives (i.e. u_{ij}^β's and θ_{ij}^β's) as

$$\left\{ \begin{array}{c} u_{11}^\beta \\ u_{12}^\beta \\ u_{21}^\beta \\ u_{22}^\beta \end{array} \right\} = \frac{1}{\Psi^\beta} \left[\overline{\boldsymbol{A}}^{\beta 1} \middle| \overline{\boldsymbol{A}}^{\beta 2} \middle| \overline{\boldsymbol{A}}^{\beta 3} \right] \left\{ \begin{array}{c} u_1^1 \\ u_2^1 \\ u_1^2 \\ u_2^2 \\ u_1^3 \\ u_2^3 \end{array} \right\}$$

$$\left\{ \begin{array}{c} \theta_{31} \\ \theta_{32} \end{array} \right\} = \frac{1}{\Psi^\beta} \left[\begin{array}{ccc} A_1^{\beta 1} & A_1^{\beta 2} & A_1^{\beta 3} \\ A_2^{\beta 1} & A_2^{\beta 2} & A_3^{\beta 3} \end{array} \right] \left\{ \begin{array}{c} \theta_3^1 \\ \theta_3^2 \\ \theta_3^3 \end{array} \right\}.$$

D.1.2 Stiffness matrices

D.1.2.1 K_{jl}'s

$K_{jl}^{\beta\alpha\alpha'} = \int_{\Psi^\beta} A_i^{\beta\alpha} c_{ijkl}^\beta A_k^{\beta\alpha'} \mathrm{d}s$ can be expressed in matrix form as

$$\left[\begin{array}{cc} K_{11}^{\beta\alpha\alpha'} & K_{12}^{\beta\alpha\alpha'} \\ K_{21}^{\beta\alpha\alpha'} & K_{22}^{\beta\alpha\alpha'} \end{array} \right] = \Psi^\beta \left(\overline{\boldsymbol{A}}^{\beta\alpha} \right)^T \boldsymbol{C} \overline{\boldsymbol{A}}^{\beta\alpha}$$

where

$$\boldsymbol{C}=\begin{bmatrix} c^{\beta}_{1111} & c^{\beta}_{1121} & c^{\beta}_{1112} & c^{\beta}_{1122} \\ c^{\beta}_{2111} & c^{\beta}_{2121} & c^{\beta}_{2112} & c^{\beta}_{2122} \\ c^{\beta}_{1211} & c^{\beta}_{1221} & c^{\beta}_{1212} & c^{\beta}_{1222} \\ c^{\beta}_{2211} & c^{\beta}_{2221} & c^{\beta}_{2212} & c^{\beta}_{2222} \end{bmatrix}$$

D.1.2.2 $\check{K}^{\beta\alpha\alpha'}_{jl}$'s

In matrix form $\check{K}^{\beta\alpha\alpha'}_{jl}=\int_{\Psi^\beta}\phi^\alpha q^\beta_{lkj}A^{\beta\alpha'}_k\,\mathrm{d}s$ with $i,k=\{1,2\}$ and $j=3$.

$$\begin{Bmatrix} \check{K}^{\beta a a'}_{31} \\ \check{K}^{\beta a a'}_{32} \end{Bmatrix} = \Phi^a \begin{bmatrix} q^\beta_{113} & q^\beta_{123} \\ q^\beta_{213} & q^\beta_{223} \end{bmatrix} \begin{Bmatrix} A^{\beta a'}_1 \\ A^{\beta a'}_2 \end{Bmatrix}$$

D.1.2.3 $\tilde{K}^{\beta\alpha\alpha'}_{jl}$'s

$\tilde{K}^{\beta\alpha\alpha'}_{jl}=\int_{\Psi^\beta}\phi^\alpha d^\beta_{jl}\phi^{\alpha'}\,\mathrm{d}s$ with $j,l=3$.

$$\begin{aligned} \tilde{K}^{\beta aa}_{33} &= \Phi^a \quad d^\beta_{33} \\ \text{and } \tilde{K}^{\beta aa'}_{33} &= \quad 0 \text{ if } a\neq a'. \end{aligned}$$

D.1.2.4 $\grave{K}^{\beta\alpha\alpha'}_{jl}$'s

$\grave{K}^{\beta aa'}_{jl}=\int_{\Psi^\beta}A^{\beta\alpha}_i v^\beta_{ijkl}A^{\beta\alpha'}_k\,\mathrm{d}s$ with $i,k=\{12\}$ and $j,l=3$.

$$\grave{K}^{\beta aa'}_{33} = \Psi^\beta \begin{Bmatrix} A^{\beta a}_1 & A^{\beta a}_2 \end{Bmatrix} \begin{bmatrix} v^\beta_{1313} & v^\beta_{1323} \\ v^\beta_{2313} & v^\beta_{2323} \end{bmatrix} \begin{Bmatrix} A^{\beta a'}_1 \\ A^{\beta a'}_2 \end{Bmatrix}$$

D.1.3 How to assemble the global matrices

In solving the resulting governing equations, if we use explicit time integration, we can either assemble both the linear set of equations Eq. 5.10 and 5.11 into one global matrix, or independently advance those in time. The global matrix with both the set of equations for one triangular element would look like.

$$\begin{Bmatrix} f_1^1 \\ f_2^1 \\ t_3^1 \\ f_1^2 \\ f_2^2 \\ t_3^2 \\ f_1^3 \\ f_3^3 \\ t_3^1 \end{Bmatrix} = \begin{bmatrix} K_{11}^{\beta 11} & K_{12}^{\beta 11} & \check{K}_{13}^{\beta 11} & K_{11}^{\beta 12} & K_{12}^{\beta 12} & \check{K}_{13}^{\beta 12} & K_{11}^{\beta 13} & K_{12}^{\beta 13} & \check{K}_{13}^{\beta 13} \\ K_{12}^{\beta 11} & K_{22}^{\beta 11} & \check{K}_{23}^{\beta 11} & K_{12}^{\beta 12} & K_{22}^{\beta 12} & \check{K}_{23}^{\beta 12} & K_{12}^{\beta 13} & K_{22}^{\beta 13} & \check{K}_{23}^{\beta 13} \\ \check{K}_{13}^{\beta 11} & \check{K}_{23}^{\beta 11} & \bar{K}_{33}^{\beta 11} & \check{K}_{13}^{\beta 12} & \check{K}_{23}^{\beta 12} & \grave{K}_{33}^{\beta 12} & \check{K}_{13}^{\beta 13} & \check{K}_{23}^{\beta 13} & \grave{K}_{33}^{\beta 13} \\ K_{11}^{\beta 21} & K_{12}^{\beta 21} & \check{K}_{13}^{\beta 21} & K_{11}^{\beta 22} & K_{12}^{\beta 22} & \check{K}_{13}^{\beta 22} & K_{11}^{\beta 23} & K_{12}^{\beta 23} & \check{K}_{13}^{\beta 23} \\ K_{12}^{\beta 21} & K_{22}^{\beta 21} & \check{K}_{23}^{\beta 21} & K_{12}^{\beta 22} & K_{22}^{\beta 22} & \check{K}_{23}^{\beta 22} & K_{12}^{\beta 23} & K_{22}^{\beta 23} & \check{K}_{23}^{\beta 23} \\ \check{K}_{13}^{\beta 21} & \check{K}_{23}^{\beta 21} & \grave{K}_{33}^{\beta 21} & \check{K}_{13}^{\beta 22} & \check{K}_{23}^{\beta 22} & \bar{K}_{33}^{\beta 22} & \check{K}_{13}^{\beta 23} & \check{K}_{23}^{\beta 23} & \grave{K}_{33}^{\beta 23} \\ K_{11}^{\beta 31} & K_{12}^{\beta 31} & \check{K}_{13}^{\beta 31} & K_{11}^{\beta 32} & K_{12}^{\beta 32} & \check{K}_{13}^{\beta 32} & K_{11}^{\beta 33} & K_{12}^{\beta 33} & \check{K}_{13}^{\beta 33} \\ K_{12}^{\beta 31} & K_{22}^{\beta 31} & \check{K}_{23}^{\beta 31} & K_{12}^{\beta 32} & K_{22}^{\beta 32} & \check{K}_{23}^{\beta 32} & K_{12}^{\beta 33} & K_{22}^{\beta 33} & \check{K}_{23}^{\beta 33} \\ \check{K}_{13}^{\beta 31} & \check{K}_{23}^{\beta 31} & \grave{K}_{33}^{\beta 31} & \check{K}_{13}^{\beta 32} & \check{K}_{23}^{\beta 32} & \grave{K}_{33}^{\beta 32} & \check{K}_{13}^{\beta 33} & \check{K}_{23}^{\beta 33} & \bar{K}_{33}^{\beta 33} \end{bmatrix} \begin{Bmatrix} u_1^1 \\ u_2^1 \\ \theta_3^1 \\ u_1^2 \\ u_2^2 \\ \theta_3^2 \\ u_1^3 \\ u_3^3 \\ \theta_3^1 \end{Bmatrix}$$

where $\bar{K}_{33}^{\beta ii} = \tilde{K}_{33}^{\beta ii} + \grave{K}_{33}^{\beta ii}$

D.2 Second derivative

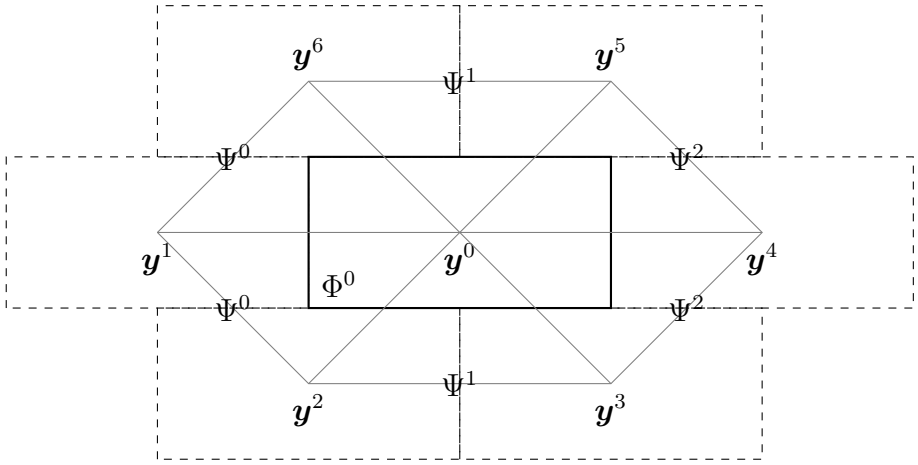

Figure D.2: 2D setting. To calculate second order derivatives, we use tessellation Φ^α

Let the triangles in the Figure D.2 named as follows; Ψ^{β_1} is the triangle $\boldsymbol{y}^0\boldsymbol{y}^1\boldsymbol{y}^2$, Ψ^{β_2} is the triangle $\boldsymbol{y}^0\boldsymbol{y}^2\boldsymbol{y}^3$, ..., Ψ^{β_6} is the triangle $\boldsymbol{y}^0\boldsymbol{y}^6\boldsymbol{y}^1$.

Lets evaluate $\int_{\partial\Psi^\beta}\phi^\alpha(\boldsymbol{x})n_k^\beta \boldsymbol{d}l$ for Φ^0 and the triangle Ψ^{β_1} formed by $\boldsymbol{y}^0\boldsymbol{y}^1\boldsymbol{y}^2$;$\boldsymbol{i}$, $\boldsymbol{j}$ and $\boldsymbol{k}$ are the unit base vectors. \n

$$\begin{aligned}
\frac{1}{\Phi^\alpha}\int_{\partial\Psi^\beta}\phi^\alpha(\boldsymbol{x})n_k^\beta \boldsymbol{d}l &= -\frac{1}{\Phi^\alpha}\left(\left(\boldsymbol{y}^0-\frac{\boldsymbol{y}^0+\boldsymbol{y}^2}{2}\right)\times\boldsymbol{k}+\left(\frac{\boldsymbol{y}^1+\boldsymbol{y}^0}{2}-\boldsymbol{y}^0\right)\times\boldsymbol{k}\right)\\
&= -\frac{1}{\Phi^\alpha}\left(\frac{\boldsymbol{y}^1-\boldsymbol{y}^2}{2}\right)\times\boldsymbol{k}\\
&= \frac{1}{2\Phi^\alpha}\left(-\left(y_2^1-y_2^2\right)\boldsymbol{i}+\left(y_1^1-y_1^2\right)\boldsymbol{j}\right)\\
\left\{\begin{array}{c} S_1^{\alpha\beta_1} \\ S_2^{\alpha\beta_1}\end{array}\right\} &= \frac{1}{\Phi^\alpha}\left\{\begin{array}{c} -(y_2^1-y_2^2) \\ (y_1^1-y_1^2)\end{array}\right\}
\end{aligned}$$

Similarly, next, lets evaluate $\int_{\partial\Psi^\beta}\phi^\alpha(\boldsymbol{x})n_k^\beta \boldsymbol{d}l$ for Φ^0 and the triangle Ψ^{β_2} formed by $\boldsymbol{y}^0\boldsymbol{y}^2\boldsymbol{y}^3$.

$$\begin{aligned}
\frac{1}{\Phi^\alpha}\int_{\partial\Psi^\beta}\phi^\alpha(\boldsymbol{x})n_k^\beta \boldsymbol{d}l &= -\frac{1}{\Phi^\alpha}\left(\left(\boldsymbol{y}^0-\frac{\boldsymbol{y}^0+\boldsymbol{y}^3}{2}\right)\times\boldsymbol{k}+\left(\frac{\boldsymbol{y}^2+\boldsymbol{y}^0}{2}-\boldsymbol{y}^0\right)\times\boldsymbol{k}\right)\\
&= \frac{1}{\Phi^\alpha}\left(\frac{\boldsymbol{y}^2-\boldsymbol{y}^3}{2}\right)\times\boldsymbol{k}\\
&= \frac{1}{2\Phi^\alpha}\left(-\left(y_2^2-y_2^3\right)\boldsymbol{i}+\left(y_1^2-y_1^3\right)\boldsymbol{j}\right)\\
\left\{\begin{array}{c} S_1^{\alpha\beta_2} \\ S_2^{\alpha\beta_2}\end{array}\right\} &= \frac{1}{\Phi^\alpha}\left\{\begin{array}{c} -(y_2^2-y_2^3) \\ (y_1^2-y_1^3)\end{array}\right\}
\end{aligned}$$

According to the above equations, we can express u_{11k}^α in the following matrix form.

$$\left\{\begin{array}{c} u_{111}^\alpha \\ u_{112}^\alpha\end{array}\right\} = \left[\begin{array}{c|c|c|c} S_1^{\alpha\beta_1} & S_1^{\alpha\beta_2} & \cdots & S_1^{\alpha\beta_6} \\ S_2^{\alpha\beta_1} & S_2^{\alpha\beta_2} & & S_2^{\alpha\beta_6}\end{array}\right]\left\{\begin{array}{c} u_{11}^{\beta_1} \\ u_{11}^{\beta_2} \\ u_{11}^{\beta_3} \\ \vdots \\ u_{11}^{\beta_5} \\ u_{11}^{\beta_6}\end{array}\right\}$$

In general, u_{ijk}^α, can be expressed in the following matrix form

$$\left\{ \begin{array}{c} u^{\alpha}_{ij1} \\ u^{\alpha}_{ij2} \end{array} \right\} = \left[\begin{array}{c|c|c|c} S^{\alpha\beta_1}_1 & S^{\alpha\beta_2}_1 & \cdots & S^{\alpha\beta_6}_1 \\ S^{\alpha\beta_1}_2 & S^{\alpha\beta_2}_2 & & S^{\alpha\beta_6}_2 \end{array} \right] \left\{ \begin{array}{c} u^{\beta_1}_{ij} \\ u^{\beta_2}_{ij} \\ u^{\beta_3}_{ij} \\ \vdots \\ u^{\beta_5}_{ij} \\ u^{\beta_6}_{ij} \end{array} \right\}$$

In the case of inner Φ^{α}, the above calculation involves 6 Ψ^{β} as,

$$\left\{ \begin{array}{c} u^{\alpha}_{111} \\ u^{\alpha}_{112} \\ u^{\alpha}_{121} \\ u^{\alpha}_{122} \\ u^{\alpha}_{211} \\ u^{\alpha}_{212} \\ u^{\alpha}_{221} \\ u^{\alpha}_{222} \end{array} \right\} = \left[\bar{\boldsymbol{S}}^{\alpha\beta_1} \middle| \bar{\boldsymbol{S}}^{\alpha\beta_2} \middle| \ldots \middle| \bar{\boldsymbol{S}}^{\alpha\beta_6} \right] \left\{ \begin{array}{c} \bar{\boldsymbol{u}}'^{\beta_1} \\ \bar{\boldsymbol{u}}'^{\beta_2} \\ \bar{\boldsymbol{u}}'^{\beta_3} \\ \bar{\boldsymbol{u}}'^{\beta_4} \\ \bar{\boldsymbol{u}}'^{\beta_5} \\ \bar{\boldsymbol{u}}'^{\beta_6} \end{array} \right\}$$

where

$$\bar{\boldsymbol{S}}^{\alpha\beta_i} = \left[\begin{array}{cccc} S^{\alpha\beta_i}_1 & 0 & 0 & 0 \\ S^{\alpha\beta_i}_2 & 0 & 0 & 0 \\ 0 & S^{\alpha\beta_i}_1 & 0 & 0 \\ 0 & S^{\alpha\beta_i}_2 & 0 & 0 \\ 0 & 0 & S^{\alpha\beta_i}_1 & 0 \\ 0 & 0 & S^{\alpha\beta_i}_2 & 0 \\ 0 & 0 & 0 & S^{\alpha\beta_i}_1 \\ 0 & 0 & 0 & S^{\alpha\beta_i}_2 \end{array} \right]$$

and

$$\bar{\boldsymbol{u}}'^{\beta_i} = \left\{ \begin{array}{c} u^{\beta_i}_{11} \\ u^{\beta_i}_{12} \\ u^{\beta_i}_{21} \\ u^{\beta_i}_{22} \end{array} \right\}$$

Derivative, $\bar{\boldsymbol{u}}'^{\beta_i}$, can be written in matrix form and in term of translation as,

$$\left\{\begin{array}{c}\bar{\boldsymbol{u}}'^{\beta_1}\\ \bar{\boldsymbol{u}}'^{\beta_2}\\ \bar{\boldsymbol{u}}'^{\beta_3}\\ \bar{\boldsymbol{u}}'^{\beta_4}\\ \bar{\boldsymbol{u}}'^{\beta_5}\\ \bar{\boldsymbol{u}}'^{\beta_6}\end{array}\right\}=\left[\begin{array}{ccccccc}\overline{\boldsymbol{A}}^{\beta_1 1} & \overline{\boldsymbol{A}}^{\beta_1 2} & \overline{\boldsymbol{A}}^{\beta_1 3} & \mathbf{0} & \mathbf{0} & \mathbf{0} & \mathbf{0}\\ \overline{\boldsymbol{A}}^{\beta_2 3} & \mathbf{0} & \overline{\boldsymbol{A}}^{\beta_2 1} & \overline{\boldsymbol{A}}^{\beta_2 2} & \mathbf{0} & \mathbf{0} & \mathbf{0}\\ \overline{\boldsymbol{A}}^{\beta_3 2} & \mathbf{0} & \mathbf{0} & \overline{\boldsymbol{A}}^{\beta_3 3} & \overline{\boldsymbol{A}}^{\beta_3 1} & \mathbf{0} & \mathbf{0}\\ \overline{\boldsymbol{A}}^{\beta_4 1} & \mathbf{0} & \mathbf{0} & \mathbf{0} & \overline{\boldsymbol{A}}^{\beta_4 2} & \overline{\boldsymbol{A}}^{\beta_4 3} & \mathbf{0}\\ \overline{\boldsymbol{A}}^{\beta_5 3} & \mathbf{0} & \mathbf{0} & \mathbf{0} & \mathbf{0} & \overline{\boldsymbol{A}}^{\beta_5 1} & \overline{\boldsymbol{A}}^{\beta_5 2}\\ \overline{\boldsymbol{A}}^{\beta_6 2} & \overline{\boldsymbol{A}}^{\beta_6 1} & \mathbf{0} & \mathbf{0} & \mathbf{0} & \mathbf{0} & \overline{\boldsymbol{A}}^{\beta_6 3}\end{array}\right]\left\{\begin{array}{c}\boldsymbol{u}^0\\ \boldsymbol{u}^1\\ \boldsymbol{u}^2\\ \vdots\\ \boldsymbol{u}^6\end{array}\right\}$$

Where $\overline{\boldsymbol{A}}^{\beta_i j}$ can be obtained from Eq. D.1.
Thus, the damping force can be written as,

$$\left\{\begin{array}{c}F_1\\ F_2\end{array}\right\}=\Phi^{\alpha}\left[\begin{array}{cccccccc}\hat{C}_{1111} & \hat{C}_{1121} & \hat{C}_{2111} & \hat{C}_{2121} & \hat{C}_{1112} & \hat{C}_{1122} & \hat{C}_{2112} & \hat{C}_{2122}\\ \hat{C}_{1211} & \hat{C}_{1221} & \hat{C}_{2211} & \hat{C}_{2221} & \hat{C}_{1212} & \hat{C}_{1222} & \hat{C}_{2212} & \hat{C}_{2222}\end{array}\right]\left\{\begin{array}{c}\dot{u}^{\alpha}_{111}\\ \dot{u}^{\alpha}_{112}\\ \dot{u}^{\alpha}_{121}\\ \dot{u}^{\alpha}_{122}\\ \dot{u}^{\alpha}_{211}\\ \dot{u}^{\alpha}_{212}\\ \dot{u}^{\alpha}_{221}\\ \dot{u}^{\alpha}_{222}\end{array}\right\}$$

.

Appendix E

Artificial damping

According to the analytical solution and numerical simulation for both RBSM and PDS-FEM, it is seen that the frequency is high. However, the rotation of bricks cannot produce this such high frequency in practices. It is mentioned by Hori et al.[1] that the high frequency spin can be a possible source of damping in granule materials.

This chapter presents the physical explanation of energy dissipation due to high frequency rotation.

E.1 Artificial damping

In order to show hypothesized damping mechanism, the stone block wall shown in Figure E.1 is considered. According to the stone block properties, Eq. (4.23) predicts that spin frequency of the blocks is about 12600 rad/s. Physically, this high frequency vibrations should rapidly decay due to interface friction, non-linear properties of mortar, etc. However, due to the coupling between translation and rotation, some energy is transfer from translational modes to generate rotational waves. As a result, the energy of system should continuously loose as the effect of damping, due to the high frequency rotations . Note that there could be other mechanisms that cause damping; e.g. nonlinear effects due to spins, translation induced damping, etc.

E.1.1 Numerical simulation for the rotational damping

To support the claim of the hypothesis explained above, a RBSM model of stone brick wall is constructed following the experiments reported by Elmenshawi et al.[30] as shown in Figure E.1. Stiffness k and h are set to be $2.03\times10^{10}\mathrm{N/m^3}$ and $4.69\times10^{8}\mathrm{N/m^3}$, respectively. The block density is assumed to be $2650\mathrm{kg/m^3}$. For the initial condition, The model is subjected by 9 kN horizontal distributed static force over the top edge (see Figure E.1) induced initial deformation. Then, the distributed static force was suddenly released, and the dynamic response of the wall, at the point A, is recorded.

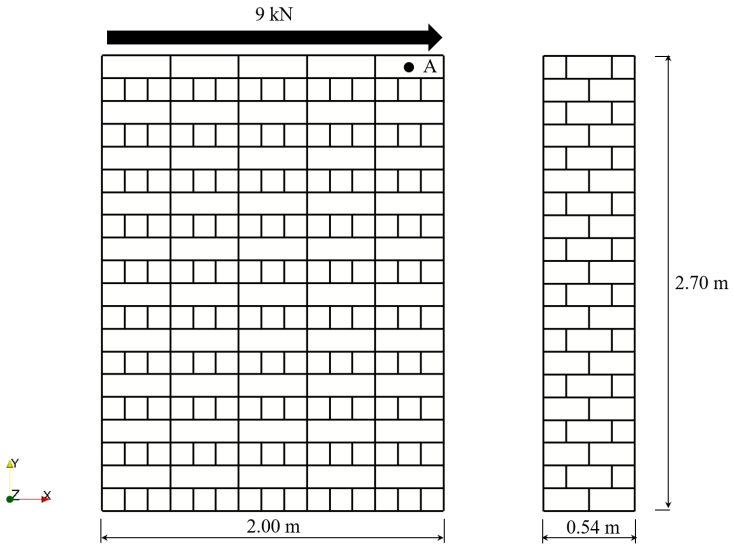

Figure E.1: Brick wall model.

In this simulation, an artificial damping term $-\overline{\boldsymbol{C}}\cdot\dot{\boldsymbol{\theta}}^{\mu}$ is added in to discrete equation of rotation, Eq. 4.6, to produce rapid decay of high speed spins. In this 2D in-plane problem, in-plane component the damping coefficient, $\overline{C}_{33}=2\zeta I_{33}\omega_{\text{spin}}$, is applied where ζ is the rotational damping ratio, ω_{spin} is the rotational frequency from Eq. 4.23 in chapter 4. I_{33} is the mass moment of the inertia of a brick. The discrete equation of motion with the artificial damping is

$$\begin{aligned} m^{\mu}\ddot{\boldsymbol{u}}^{\mu} &= \sum_{\gamma}\Big\{\boldsymbol{K}^{\mu\gamma}\cdot\left(\boldsymbol{u}^{\gamma+}-2\boldsymbol{u}^{\mu}+\boldsymbol{u}^{\gamma-}\right) \\ &\quad -\hat{\boldsymbol{K}}^{\mu\gamma}\cdot\left(\boldsymbol{\theta}^{\gamma+}-\boldsymbol{\theta}^{\gamma-}\right)\Big\} \\ \boldsymbol{I}^{\mu}\cdot\ddot{\boldsymbol{\theta}}^{\mu} &= -\overline{\boldsymbol{C}}\cdot\dot{\boldsymbol{\theta}}^{\mu}+\sum_{\gamma}\Big\{\left(\hat{\boldsymbol{K}}^{\mu\gamma}\right)^{\mathrm{T}}\cdot\left(\boldsymbol{u}^{\gamma+}-\boldsymbol{u}^{\gamma-}\right) \\ &\quad -\overline{\boldsymbol{K}}^{\mu\gamma}\cdot\left(\boldsymbol{\theta}^{\gamma+}+2\boldsymbol{\theta}^{\mu}+\boldsymbol{\theta}^{\gamma-}\right) \\ &\quad +\overline{\overline{\boldsymbol{K}}}^{\mu\gamma}\cdot\left(\boldsymbol{\theta}^{\gamma+}-2\boldsymbol{\theta}^{\mu}+\boldsymbol{\theta}^{\gamma-}\right)\Big\} \end{aligned} \tag{E.1}$$

E.1.2 Contributions to kinetic energy

In this section, comparison of the kinetic energy from translational and rotational modes of undamped system is represented. Figure E.2 represents the kinetic energy of the undamped free vibrating brick wall, where E.2(a) and (b) show the energy due to translation ($T_u=\sum_{\mu}\frac{1}{2}m\dot{\boldsymbol{u}}^{\mu}\cdot\dot{\boldsymbol{u}}^{\mu}$) and rotation ($T_{\theta}=\sum_{\mu}\frac{1}{2}\dot{\boldsymbol{\theta}}^{\mu}\cdot\boldsymbol{I}\cdot\dot{\boldsymbol{\theta}}^{\mu}$).

According to Figure E.2, T_{θ} is several orders smaller than T_u. This dramatically difference in several orders raises the doubt whether the hypothesized high frequency damping mechanism have

any significance to cause damping. However, the next section will show that the high frequency rotations can cause significant damping.

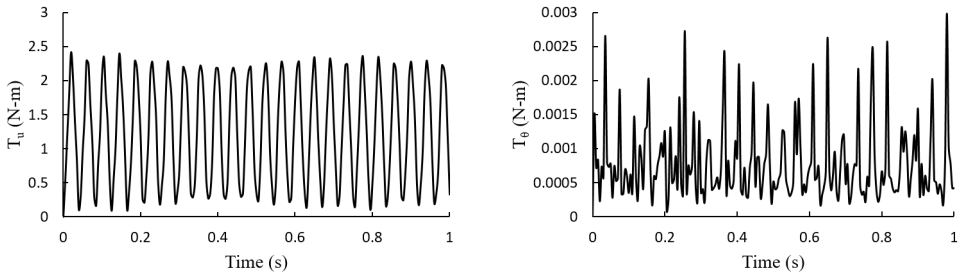

(a) (b)

Figure E.2: Kinetic energy of the undamped free vibration brick wall, (a) translation term, (b) rotation term.

E.1.3 Energy dissipation due to high frequency vibrations

This section express the effect of the artificial damping term, $-\overline{\boldsymbol{C}}\cdot\dot{\boldsymbol{\theta}}^{\mu}$, on the dissipation of energy. Figure E.3 shows time history of the total energy of the artificially damped system (i.e. with $-\overline{\boldsymbol{C}}\cdot\dot{\boldsymbol{\theta}}^{\mu}$ term) with different damping ratios. For unhampered system, $\zeta=0$, the near perfect energy conservation is shown which is prove to be indirect evidence of the accuracy of the simulations. Further, the higher the rate of decay of high speed spin due to higher ζ indicate the faster the loss of energy of the system. The continuous loss of energy is due to the coupling between the rotational and translational modes, $\hat{\boldsymbol{K}}^{\mu\gamma}\cdot(\boldsymbol{\theta}^{\gamma+}-\boldsymbol{\theta}^{\gamma-})$ and $\left(\hat{\boldsymbol{K}}^{\mu\gamma}\right)^{\mathrm{T}}\cdot(\boldsymbol{u}^{\gamma+}-\boldsymbol{u}^{\gamma-})$ in Eq. 4.6 (or $\boldsymbol{q}:\nabla\boldsymbol{\theta}$ and $\boldsymbol{q}^{\mathrm{T}}:\nabla\boldsymbol{u}$ in Eq. 4.19)

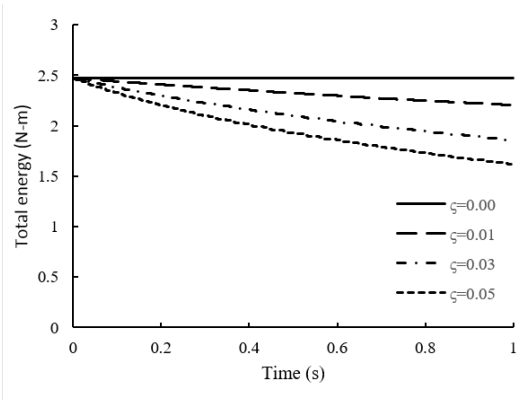

Figure E.3: Time history of total energy with different ζ.

E.1.4 The decay of the acceleration amplitude

For further investigation of the damping mechanisms, Figure E.4 shows the time history of the horizontal acceleration of the brick at the point A in Figure E.1, for $\zeta = 0.05$. As the time history of accelerations is nearly closed to the observations by Elmenshawi et al.[30], it is clearly shown that decaying of the acceleration amplitude is due to damping effect. The high frequency vibration at the beginning is caused by the instantaneous release of the external distributed force in the numerical model. However, high frequency is not observed in the observations by Elmenshawi et al.[30]. This is probably because the external load is not release instantaneously in the real experiment. Also, sampling rate of accelerometers have limited. However, after 0.5s, the frequency and the amplitude of the wave profile of the numerical results are comparable to observations by Elmenshawi et al.[30].

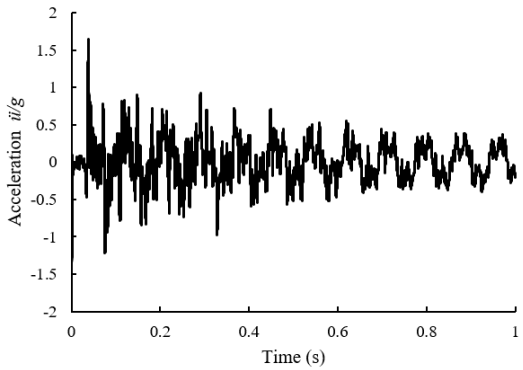

Figure E.4: Horizontal acceleration at point A with $\zeta = 0.05$.

Appendix F

Equations of motion of damped block spring system

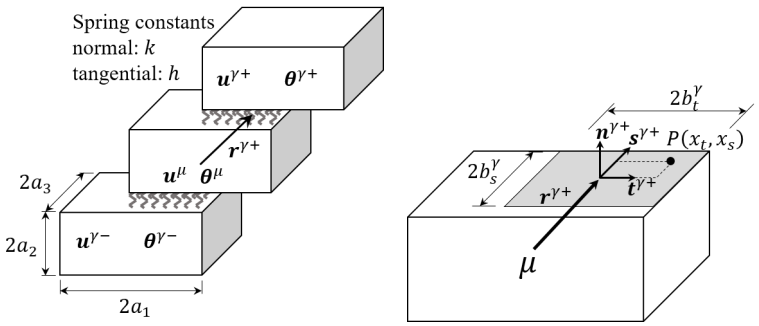

Figure F.1: (a): Idealized block-spring model, (b): Contact area..

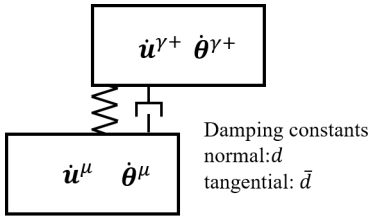

Figure F.2: damping on the contact area.

This appendix express the formulation of continuumnization of block spring while mortar is the source of damping. In additional to the idealized block spring systems in chapter Figure F.1, the damping is add in each contact area as well as springs assuming that the damping forces are proportional to the velocity as d and $\bar{d}$ denote normal and tangential damping constants, respectively.

Like the relative motion, $\boldsymbol{L}^{\mu\gamma+}$, the relative velocity,$\dot{\boldsymbol{L}}^{\mu\gamma+}$, at point $P(x_t,x_s)$ on the interface of block μ and its $\gamma+$ is

$$\dot{\boldsymbol{L}}^{\mu\gamma+} = \left(\dot{\boldsymbol{u}}^{\gamma+}-\dot{\boldsymbol{u}}^{\mu}\right)-\left(\dot{\boldsymbol{\theta}}^{\gamma+}+\dot{\boldsymbol{\theta}}^{\mu}\right)\times\boldsymbol{r}^{\gamma+}+\left(\dot{\boldsymbol{\theta}}^{\gamma+}-\dot{\boldsymbol{\theta}}^{\mu}\right)\times\left(x_t\boldsymbol{t}^{\gamma+}+x_s\boldsymbol{s}^{\gamma+}\right). \tag{F.1}$$

Then, the damping force per unit area at the interface of block μ and its $\gamma+$ neighbor can be expressed as

$$\boldsymbol{F}^{\mu\gamma+} = -d(\dot{\boldsymbol{L}}^{\gamma+}\cdot\boldsymbol{n}^{\gamma+})\boldsymbol{n}^{\gamma+}-\bar{d}(\dot{\boldsymbol{L}}^{\gamma+}\cdot\boldsymbol{s}^{\gamma+})\boldsymbol{s}^{\gamma+}-\bar{d}(\dot{\boldsymbol{L}}^{\gamma+}\cdot\boldsymbol{t}^{\gamma+})\boldsymbol{t}^{\gamma+}$$

As the damping force is obtained above, the virture work due to the nonconervative can be expressed as,

$$\delta W^{\mu\gamma+} = \int_{-b_s}^{b_s}\int_{-b_t}^{b_t}\boldsymbol{F}^{\mu\gamma+}\cdot\delta\boldsymbol{L}^{\mu\gamma+}\mathrm{d}x_t\mathrm{d}x_s$$

where $\delta\boldsymbol{L}^{\mu\gamma+}$ is the variation of relative motion in chapter 4 as

$$\delta L_j^+ = -\left(\delta u_j+\epsilon_{jvw}\delta\theta_v r_w+\epsilon_{jvw}\delta\theta_v(x_t t_w+x_s s_w)\right). \tag{F.2}$$

For the sake of simplicity, superscripts μ and γ are omitted in the following formulation of $\delta W^{\mu\gamma+}$. Then,

$$\begin{aligned}
\delta W^{\mu\gamma+} &= -\int_{-b_s}^{b_s}\int_{-b_t}^{b_t}\left(d(\dot{\boldsymbol{L}}^{+}\cdot\boldsymbol{n}^{+})\boldsymbol{n}^{+}+\bar{d}(\dot{\boldsymbol{L}}^{+}\cdot\boldsymbol{s}^{+})\boldsymbol{s}^{+}+\bar{d}(\dot{\boldsymbol{L}}^{+}\cdot\boldsymbol{t}^{+})\boldsymbol{t}^{+}\right)\cdot\delta\boldsymbol{L}^{+}\mathrm{d}x_t\mathrm{d}x_s \\
&= -\left(dn_i^+n_j^++\bar{d}s_i^+s_j^++\bar{d}t_i^+t_j^+\right)\int_{-b_s}^{b_s}\int_{-b_t}^{b_t}\dot{L}_i^+\delta L_j^+\mathrm{d}x_t\mathrm{d}x_s \\
&= -\frac{1}{4b_t^\gamma b_s^\gamma}D_{ij}^{\gamma+}\int_{-b_s}^{b_s}\int_{-b_t}^{b_t}\dot{L}_i^+\delta L_j^+\mathrm{d}x_t\mathrm{d}x_s
\end{aligned} \tag{F.3}$$

where

$$D_{ij}^{\gamma+} = 4b_t^\gamma b_s^\gamma\left(dn_i^{\gamma+}n_j^{\gamma+}+\bar{d}s_i^{\gamma+}s_j^{\gamma+}+\bar{d}t_i^{\gamma+}t_j^{\gamma+}\right)$$

Using Eq. F.1 and F.2 , $\int_{-b_s}^{b_s}\int_{-b_t}^{b_t}\dot{L}_i^+\delta L_j^+\mathrm{d}x_t\mathrm{d}x_s$ term can be expressed as.

$$
\begin{aligned}
\int_{-b_s}^{b_s}\int_{-b_t}^{b_t} \dot{L}_i^+ \delta L_j^+ \mathrm{d}x_t \mathrm{d}x_s &= -\int_{-b_s}^{b_s}\int_{-b_t}^{b_t} \left(\left(\dot{u}_i^+ - \dot{u}_i\right) - \epsilon_{ipq}\left(\dot{\theta}_p^+ + \dot{\theta}_p\right) r_q^+ + \epsilon_{ipq}\left(\dot{\theta}_p^+ - \dot{\theta}_p\right)\left(x_t t_q^+ + x_s s_q^+\right)\right) \\
&\quad \left(\delta u_j + \epsilon_{jvw}\delta\theta_v r_w^+ + \epsilon_{jvw}\delta\theta_v\left(x_t t_w^+ + x_s s_w^+\right)\right)\mathrm{d}x_t \mathrm{d}x_s \\
&= -\int_{-b_s}^{b_s}\int_{-b_t}^{b_t} \left(\left(\dot{u}_i^+ - \dot{u}_i\right) - \epsilon_{ipq}\left(\dot{\theta}_p^+ + \dot{\theta}_p\right) r_q^+ + \epsilon_{ipq}\left(\dot{\theta}_p^+ - \dot{\theta}_p\right)\left(x_t t_q^+ + x_s s_q^+\right)\right) \\
&\quad \left(\delta u_j + \epsilon_{jvw}\delta\theta_v r_w^+\right)\mathrm{d}x_t \mathrm{d}x_s \\
&\quad -\int_{-b_s}^{b_s}\int_{-b_t}^{b_t} \left(\left(\dot{u}_i^+ - \dot{u}_i\right) - \epsilon_{ipq}\left(\dot{\theta}_p^+ + \dot{\theta}_p\right) r_q^+ + \epsilon_{ipq}\left(\dot{\theta}_p^+ - \dot{\theta}_p\right)\left(x_t t_q^+ + x_s s_q^+\right)\right) \\
&\quad \left(\epsilon_{jvw}\delta\theta_v\left(x_t t_w^+ + x_s s_w^+\right)\right)\mathrm{d}x_t \mathrm{d}x_s \\
&= -4b_s b_t\left(\left(\dot{u}_i^+ - \dot{u}_i\right) - \epsilon_{ipq}\left(\dot{\theta}_p^+ + \dot{\theta}_p\right) r_q^+\right)\delta u_j \\
&\quad -4b_s b_t\left\{ \left(\left(\dot{u}_i^+ - \dot{u}_i\right) - \epsilon_{ipq}\left(\dot{\theta}_p^+ + \dot{\theta}_p\right) r_q^+\right)\left(\epsilon_{jvw} r_w^+\right)\right. \\
&\quad \left. + \frac{1}{3}\left(\epsilon_{ipq}\left(\dot{\theta}_p^+ - \dot{\theta}_p\right)\epsilon_{jvw}\right)\left(b_s^2 s_q^+ s_w^+ + b_t^2 t_q^+ t_w^+\right)\right\}\delta\theta_v
\end{aligned} \tag{F.4}
$$

Substitute the above expression into Eq. F.3, the variation of the work done by damping force is

$$
\begin{aligned}
\delta W^{\gamma+} &= D_{ij}^{\gamma}\left(\dot{u}_i^+ - \dot{u}_i\right)\delta u_j \\
&\quad -4b_s b_t\left(d\left(n_i^+\epsilon_{ipq}r_q^+\right)n_j^+ + \bar{d}\left(s_i^+\epsilon_{ipq}r_q^+\right)s_j^+ + \bar{d}\left(t_i^+\epsilon_{ipq}r_q^+\right)t_j\right)\left(\theta_p^+ + \theta_p\right)\delta u_j \\
&\quad +4b_s b_t\left(dn_i^+\left(n_j^+\epsilon_{jvw}r_w^+\right) + \bar{d}s_i^+\left(s_j^+\epsilon_{jvw}r_w^+\right) + \bar{d}t_i\left(t_j^+\epsilon_{jvw}r_w^+\right)\right)\left(u_i^+ - u_i\right)\delta\theta_v \\
&\quad -4b_s b_t\left\{d\left(n_i^+\epsilon_{ipq}r_q^+\right)\left(n_j^+\epsilon_{jvw}r_w^+\right) + \bar{d}\left(s_i^+\epsilon_{ipq}r_q^+\right)\left(s_j^+\epsilon_{jvw}r_w^+\right)\right. \\
&\quad \left. + \bar{d}\left(t_i^+\epsilon_{ipq}r_q^+\right)\left(t_j^+\epsilon_{jvw}r_w^+\right)\right\}\left(\theta_p^+ + \theta_p\right)\delta\theta_v \\
&\quad +\frac{4}{3}b_s b_t\left(dn_i^+ n_j^+ + \bar{d}s_i^+ s_j^+ + \bar{d}t_i^+ t_j^+\right)\epsilon_{ipq}\epsilon_{jvw}\left(b_s^2 s_q^+ s_w^+ + b_t^2 t_q^+ t_w^+\right)\left(\theta_p^+ - \theta_p\right)\delta\theta_v \\
&= \boldsymbol{D}^{\gamma} : \left(\boldsymbol{u}^+ - \boldsymbol{u}\right)\otimes\delta\boldsymbol{u} - \hat{\boldsymbol{D}}^{\gamma+} : \left(\boldsymbol{\theta}^+ + \boldsymbol{\theta}\right)\otimes\delta\boldsymbol{u} + \left(\hat{\boldsymbol{D}}^{\gamma+}\right)^t : \left(\boldsymbol{u}^+ - \boldsymbol{u}\right)\otimes\delta\boldsymbol{\theta} \\
&\quad -\bar{\boldsymbol{D}}^{\gamma+} : \left(\boldsymbol{\theta}^+ + \boldsymbol{\theta}\right)\otimes\delta\boldsymbol{\theta} + \bar{\bar{\boldsymbol{D}}}^{\gamma+} : \left(\boldsymbol{\theta}^+ - \boldsymbol{\theta}\right)\otimes\delta\boldsymbol{\theta}
\end{aligned}
$$

where

$$
\begin{aligned}
\boldsymbol{D}^{\gamma+} &= 4b_t^\gamma b_s^\gamma \left(d\boldsymbol{n}^{\gamma+}\otimes\boldsymbol{n}^{\gamma+}+\bar{d}\left(\boldsymbol{s}^{\gamma+}\otimes\boldsymbol{s}^{\gamma+}+\boldsymbol{t}^{\gamma+}\otimes\boldsymbol{t}^{\gamma+}\right)\right)\\
\hat{\boldsymbol{D}}^{\gamma+} &= 4b_t^\gamma b_s^\gamma \left(d\boldsymbol{n}^{\gamma+}\otimes\left(\boldsymbol{r}^{\gamma+}\times\boldsymbol{n}^{\gamma+}\right)+\bar{d}\boldsymbol{s}^{\gamma+}\otimes\left(\boldsymbol{r}^{\gamma+}\times\boldsymbol{s}^{\gamma+}\right)+\bar{d}\boldsymbol{t}^{\gamma+}\otimes\left(\boldsymbol{r}^{\gamma+}\times\boldsymbol{t}^{\gamma+}\right)\right)\\
\bar{\boldsymbol{D}}^{\gamma+} &= 4b_t^\gamma b_s^\gamma \left\{d\left(\boldsymbol{r}^{\gamma+}\times\boldsymbol{n}^{\gamma+}\right)\otimes\left(\boldsymbol{r}^{\gamma+}\times\boldsymbol{n}^{\gamma+}\right)+\bar{d}\left(\boldsymbol{r}^{\gamma+}\times\boldsymbol{s}^{\gamma+}\right)\otimes\left(\boldsymbol{r}^{\gamma+}\times\boldsymbol{s}^{\gamma+}\right)\right.\\
&= \left.+\bar{d}\left(\boldsymbol{r}^{\gamma+}\times\boldsymbol{t}^{\gamma+}\right)\otimes\left(\boldsymbol{r}^{\gamma+}\times\boldsymbol{t}^{\gamma+}\right)\right\}\\
\bar{\bar{\boldsymbol{D}}}^{\gamma+} &= \frac{4}{3}b_t^\gamma b_s^\gamma \left(d\left(b_s^{\gamma 2}\boldsymbol{t}^{\gamma+}\otimes\boldsymbol{t}^{\gamma+}+b_t^{\gamma 2}\boldsymbol{s}^{\gamma+}\otimes\boldsymbol{s}^{\gamma+}\right)+\bar{d}\left(b_t^{\gamma 2}+b_s^{\gamma 2}\right)\boldsymbol{n}^{\gamma+}\otimes\boldsymbol{n}^{\gamma+}\right)
\end{aligned}
$$

Symmetrically, $\hat{\boldsymbol{D}}^{\gamma+}=-\hat{\boldsymbol{D}}^{\gamma-}$, $\bar{\boldsymbol{D}}^{\gamma+}=\bar{\boldsymbol{D}}^{\gamma-}$ and $\bar{\bar{\boldsymbol{D}}}^{\gamma+}=\bar{\bar{\boldsymbol{D}}}^{\gamma-}$. Further, due to the homogeneous assumption of the idealized system, these four tensors above are independent of position, for example independent of μ. Therefore, one can express the total virtual work done by the non-conservative damping forces as

$$
\delta W = \sum_\mu\sum_\gamma \left(\delta W^{\mu\gamma+}+\delta W^{\mu\gamma-}\right)
$$

$$
\begin{aligned}
\delta W^{\mu\gamma} &= \delta W^{\mu\gamma^+}+\delta W^{\mu\gamma^-}\\
&= \boldsymbol{D}^\gamma:\left(\dot{\boldsymbol{u}}^{\gamma+}-2\dot{\boldsymbol{u}}^{\mu}+\boldsymbol{u}^{\gamma-}\right)\otimes\delta\boldsymbol{u}^\mu-\hat{\boldsymbol{D}}^{\gamma+}:\left(\dot{\boldsymbol{\theta}}^{\gamma+}-\dot{\boldsymbol{\theta}}^{\gamma-}\right)\otimes\delta\boldsymbol{u}^\mu\\
&\quad+\left(\hat{\boldsymbol{D}}^{\gamma+}\right)^t:\left(\dot{\boldsymbol{u}}^{\gamma+}-\dot{\boldsymbol{u}}^{\gamma-}\right)\otimes\delta\boldsymbol{\theta}^\mu-\bar{\boldsymbol{D}}^{\gamma+}:\left(\dot{\boldsymbol{\theta}}^{\gamma+}+2\dot{\boldsymbol{\theta}}^{\mu}+\dot{\boldsymbol{\theta}}^{\gamma-}\right)\otimes\delta\boldsymbol{\theta}^\mu\\
&\quad+\bar{\bar{\boldsymbol{D}}}^{\gamma+}:\left(\dot{\boldsymbol{\theta}}^{\gamma+}-2\dot{\boldsymbol{\theta}}^{\mu}+\dot{\boldsymbol{\theta}}^{\gamma-}\right)\otimes\delta\boldsymbol{\theta}^\mu
\end{aligned}
$$

F.1 Equation of motion

According to the Hamilton's principal, among the admissible motions the actual motion is such that

$$
\int_{t_1}^{t_2}\delta(T-V)\,\mathrm{d}t+\int_{t_1}^{t_2}\delta W\,\mathrm{d}t = 0
$$

Substituting the above expression and $\int_{t_1}^{t_2}\delta(T-V)\,\mathrm{d}t$ obtained form chapter 4 to the above equation, we can obtain

$$
\begin{aligned}
\int_{t_1}^{t_2}\delta(T-V)\,\mathrm{d}t+\int_{t_1}^{t_2}\delta W\,\mathrm{d}t &= \sum_{\mu}\int_{t_1}^{t_2}\left(\delta T-\sum_{\gamma}\delta V^{\mu\gamma}+\sum_{\gamma}\delta W^{\mu\gamma}\right)\\
0 &= -\sum_{\mu}\int_{t_1}^{t_2}(m\ddot{u}_i^{\mu}\cdot\delta u_i^{\mu}+\ddot{\theta}_j^{\mu}I_{ij}\delta\theta_i^{\mu})\,\mathrm{d}t\\
&\quad+\sum_{\mu}\sum_{\gamma}\int_{t_1}^{t_2}\Big[K_{ij}^{\gamma}(u_j^{+}-2u_j+u_j^{-})\delta u_i-\hat{K}_{ip}^{\gamma}\left(\theta_p^{+}-\theta_p^{-}\right)\delta u_i\\
&\quad+\hat{K}_{pi}^{\gamma}\left(u_p^{+}-u_p^{-}\right)\delta\theta_i+\hat{K}_{pi}^{\gamma}\left(u_p^{+}-u_p^{-}\right)\delta\theta_i\\
&\quad-\bar{K}_{ip}^{\gamma}\left(\theta_p^{+}+2\theta_p+\theta_p^{-}\right)\delta\theta_i+\bar{K}_{ip}^{\gamma}\left(\theta_p^{+}-2\theta_p+\theta_p^{-}\right)\delta\theta_i\Big]\,\mathrm{d}t\\
&\quad+\sum_{\mu}\sum_{\gamma}\int_{t_1}^{t_2}\Big[\left(D_{ij}^{\gamma}\left(\dot{u}_i^{+}-2\dot{u}_i+\dot{u}_i^{-}\right)-\hat{D}_{ip}^{\gamma}\left(\dot{\theta}_p^{+}-\dot{\theta}_p^{-}\right)\right)\delta u_i\\
&\quad+\hat{D}_{pi}^{\gamma}\left(u_p^{+}-u_p^{-}\right)\delta\theta_i-\bar{D}_{ip}^{\gamma}\left(\dot{\theta}_p^{+}+2\dot{\theta}_p+\dot{\theta}_p^{-}\right)\delta\theta_i\\
&\quad+\bar{\bar{D}}_{ip}^{\gamma+}\left(\dot{\theta}_p^{+}-2\dot{\theta}_p+\dot{\theta}_p^{-}\right)\delta\theta_i\Big]\,\mathrm{d}t
\end{aligned}
\tag{F.5}
$$

As the variation above should be 0 for arbitrary δu_i^{μ} and $\delta\theta_i^{\mu}$, which are admissible variations of u_i^{μ} and θ_i^{μ}, the following should hold

$$
\begin{aligned}
m\ddot{u}_i^{\mu} &= \sum_{\gamma}\left(K_{ij}^{\gamma}(u_j^{+}-2u_j+u_j^{-})-\hat{K}_{ip}^{\gamma}\left(\theta_p^{+}-\theta_p^{-}\right)+D_{ij}^{\gamma}\left(\dot{u}_i^{+}-2\dot{u}_i+\dot{u}_i^{-}\right)-\hat{D}_{ip}^{\gamma}\left(\dot{\theta}_p^{+}-\dot{\theta}_p^{-}\right)\right)\\
I_{ij}\ddot{\theta}_j^{\mu} &= \sum_{\gamma}\Big(\hat{K}_{pi}^{\gamma}\left(u_p^{+}-u_p^{-}\right)-\bar{K}_{ip}^{\gamma}\left(\theta_p^{+}+2\theta_p+\theta_p^{-}\right)+\bar{K}_{ip}^{\gamma}\left(\theta_p^{+}-2\theta_p+\theta_p^{-}\right)\\
&\quad\hat{D}_{pi}^{\gamma}\left(\dot{u}_p^{+}-\dot{u}_p^{-}\right)-\bar{D}_{ip}^{\gamma}\left(\dot{\theta}_p^{+}+2\dot{\theta}_p+\dot{\theta}_p^{-}\right)+\bar{\bar{D}}_{ip}^{\gamma+}\left(\dot{\theta}_p^{+}-2\dot{\theta}_p+\dot{\theta}_p^{-}\right)\Big)
\end{aligned}
\tag{F.6}
$$

F.2 Continuumnization for damped system

As the discrete equations of motion is obtained in the previous sections, tn this section, these equations are continuumnized based on the Homogenization by differential expansions, as

$$
\begin{aligned}
u_i^+ - 2u_i + u_i^- &\approx 4\frac{\partial^2 u_i(\boldsymbol{x})}{\partial x_j \partial x_k} r_j^{\gamma+} r_k^{\gamma+} \\
u_i^+ - u_i^- &\approx 4\frac{\partial u_i(\boldsymbol{x})}{\partial x_j} r_j^{\gamma+} \\
\theta_i^+ - 2\theta_i + \theta_i^- &\approx 4\frac{\partial^2 \theta_i(\boldsymbol{x})}{\partial x_j \partial x_k} r_j^{\gamma+} r_k^{\gamma+} \\
\theta_i^+ + 2\theta_i + \theta_i^- &\approx 4\theta_i + 4\frac{\partial^2 \theta_i(\boldsymbol{x})}{\partial x_j \partial x_k} r_j^{\gamma+} r_k^{\gamma+} \\
\theta_i^+ - \theta_i^- &\approx 4\frac{\partial \theta_i(\boldsymbol{x})}{\partial x_j} r_j^{\gamma+}
\end{aligned}
\tag{F.7}
$$

Substituting the discrete variables given in Eq. F.7 to Eq. F.6, one can obtain the corresponding continuum forms. First, the equations of translations is continuumized as

$$
\begin{aligned}
m\ddot{u}_i &= \sum_\gamma \left(K_{ij}^\gamma (4\frac{\partial^2 u_j}{\partial x_k \partial x_l} r_k r_l) - \hat{K}_{ip}^\gamma \left(4\frac{\partial \theta_p}{\partial x_k} r_k \right) + D_{ij}^\gamma (4\frac{\partial^2 \dot{u}_j}{\partial x_k \partial x_l} r_k r_l) - \hat{D}_{ip}^\gamma \left(4\frac{\partial \dot{\theta}_p}{\partial x_k} r_k \right) \right) \\
&= V_\mathrm{b} \left\{ \frac{\partial}{\partial x_k} \left(c_{kilj} \frac{\partial u_j}{\partial x_l} \right) + \frac{\partial}{\partial x_k} \left(\hat{c}_{kilj} \frac{\partial u_j}{\partial x_l} \right) - q_{ikp} \frac{\partial \theta_p}{\partial x_k} - \hat{q}_{ikp} \frac{\partial \theta_p}{\partial x_k} \right\}.
\end{aligned}
$$

Similarly, the continuum form of the equations of rotation is obtained as

$$
\begin{aligned}
I_{ij}\ddot{\theta}_j^\mu &= \sum_\gamma \left(\hat{K}_{pi}^\gamma 4\frac{\partial u_i}{\partial x_k} r_k^{\gamma+} - \bar{K}_{ip}^\gamma \left(4\theta_p + 4\frac{\partial^2 \theta_p(\boldsymbol{x})}{\partial x_k \partial x_l} r_k^{\gamma+} r_l^{\gamma+} \right) + \bar{\bar{K}}_{ip}^\gamma \left(4\frac{\partial^2 \theta_p(\boldsymbol{x})}{\partial x_k \partial x_l} r_k^{\gamma+} r_l^{\gamma+} \right) \right) \\
&\quad + \sum_\gamma \left(\hat{D}_{pi}^\gamma 4\frac{\partial \dot{u}_i}{\partial x_k} r_k^{\gamma+} - \bar{D}_{ip}^\gamma \left(4\theta_p + 4\frac{\partial^2 \dot{\theta}_p(\boldsymbol{x})}{\partial x_k \partial x_l} r_k^{\gamma+} r_l^{\gamma+} \right) + \bar{\bar{D}}_{ip}^\gamma \left(4\frac{\partial^2 \dot{\theta}_p(\boldsymbol{x})}{\partial x_k \partial x_l} r_k^{\gamma+} r_l^{\gamma+} \right) \right) \\
I_{ij}\ddot{\theta}_j &= V_\mathrm{b} \left\{ q_{pki} \frac{\partial u_p}{\partial x_k} + \hat{q}_{pki} \frac{\partial \dot{u}_p}{\partial x_k} - d_{ip}\theta_p - \hat{d}_{ip}\dot{\theta}_p + \frac{\partial}{\partial x_k} \left(v_{kilp} \frac{\partial v_p}{\partial x_l} \right) + \frac{\partial}{\partial x_k} \left(\hat{v}_{kilp} \frac{\partial \dot{v}_p}{\partial x_l} \right) \right\}.
\end{aligned}
$$

Thus the damped continuumnized equation of motions can be expressed as

$$
\begin{aligned}
\frac{m}{V_\mathrm{b}} \ddot{\boldsymbol{u}} &= \nabla\cdot(\boldsymbol{c}:\nabla\boldsymbol{u}) + \nabla\cdot(\hat{\boldsymbol{c}}:\nabla\dot{\boldsymbol{u}}) - \boldsymbol{q}:\nabla\boldsymbol{\theta} - \hat{\boldsymbol{q}}:\nabla\dot{\boldsymbol{\theta}} \\
\frac{1}{V_\mathrm{b}} \boldsymbol{I}\cdot\ddot{\boldsymbol{\theta}} &= \boldsymbol{q}^\mathrm{T}:\nabla\boldsymbol{u} + \hat{\boldsymbol{q}}^\mathrm{T}:\nabla\dot{\boldsymbol{u}} - \boldsymbol{d}\cdot\boldsymbol{\theta} - \hat{\boldsymbol{d}}\cdot\dot{\boldsymbol{\theta}} + \nabla\cdot(\boldsymbol{v}:\nabla\boldsymbol{\theta}) + \nabla\cdot\left(\hat{\boldsymbol{v}}:\nabla\dot{\boldsymbol{\theta}}\right),
\end{aligned}
\tag{F.8}
$$

where

$$
\begin{aligned}
\hat{\boldsymbol{c}} &= \sum_{\gamma} \frac{16 b_t^{\gamma} b_s^{\gamma}}{V_{\mathrm{b}}} \big(d \boldsymbol{r}^{\gamma+} \otimes \boldsymbol{n}^{\gamma} \otimes \boldsymbol{r}^{\gamma+} \otimes \boldsymbol{n}^{\gamma} + \bar{d} \boldsymbol{r}^{\gamma+} \otimes \boldsymbol{t}^{\gamma+} \otimes \boldsymbol{r}^{\gamma+} \otimes \boldsymbol{t}^{\gamma+} \\
&\quad + \bar{d} \boldsymbol{r}^{\gamma+} \otimes \boldsymbol{s}^{\gamma+} \otimes \boldsymbol{r}^{\gamma+} \otimes \boldsymbol{s}^{\gamma+} \Big) \\
\hat{\boldsymbol{q}} &= \sum_{\gamma} \frac{16 b_t^{\gamma} b_s^{\gamma}}{V_{\mathrm{b}}} \big\{ d \boldsymbol{n}^{\gamma} \otimes \boldsymbol{r}^{\gamma+} \otimes \big(\boldsymbol{r}^{\gamma+} \times \boldsymbol{n}^{\gamma} \big) + \bar{d} \boldsymbol{t}^{\gamma+} \otimes \boldsymbol{r}^{\gamma+} \otimes \big(\boldsymbol{r}^{\gamma+} \times \boldsymbol{t}^{\gamma+} \big) \\
&\quad + \bar{d} \boldsymbol{s}^{\gamma+} \otimes \boldsymbol{r}^{\gamma+} \otimes \big(\boldsymbol{r}^{\gamma+} \times \boldsymbol{s}^{\gamma+} \big) \big\} \\
\hat{\boldsymbol{d}} &= \sum_{\gamma} \frac{16 b_t^{\gamma} b_s^{\gamma}}{V_{\mathrm{b}}} \big\{ d \big(\boldsymbol{r}^{\gamma+} \times \boldsymbol{n}^{\gamma} \big) \otimes \big(\boldsymbol{r}^{\gamma+} \times \boldsymbol{n}^{\gamma} \big) + \bar{d} \big(\boldsymbol{r}^{\gamma+} \times \boldsymbol{t}^{\gamma+} \big) \otimes \big(\boldsymbol{r}^{\gamma+} \times \boldsymbol{t}^{\gamma+} \big) \\
&\quad + \bar{d} \big(\boldsymbol{r}^{\gamma+} \times \boldsymbol{s}^{\gamma+} \big) \otimes \big(\boldsymbol{r}^{\gamma+} \times \boldsymbol{s}^{\gamma+} \big) \big\} \\
\hat{\boldsymbol{v}} &= \sum_{\gamma} \frac{16}{V_{\mathrm{b}}} \Big\{ \bar{d} \Big(\frac{b_t^{\gamma} b_s^{\gamma 3}}{3} + \frac{b_t^{\gamma 3} b_s^{\gamma}}{3} \Big) \boldsymbol{r}^{\gamma+} \otimes \boldsymbol{n}^{\gamma} \otimes \boldsymbol{r}^{\gamma+} \otimes \boldsymbol{n}^{\gamma} \\
&\quad + \frac{k b_t^{\gamma} b_s^{\gamma 3}}{3} \boldsymbol{r}^{\gamma+} \otimes \boldsymbol{t}^{\gamma+} \otimes \boldsymbol{r}^{\gamma+} \otimes \boldsymbol{t}^{\gamma+} + \frac{k b_t^{\gamma 3} b_s^{\gamma}}{3} \boldsymbol{r}^{\gamma+} \otimes \boldsymbol{s}^{\gamma+} \otimes \boldsymbol{r}^{\gamma+} \otimes \boldsymbol{s}^{\gamma+} \Big\} \\
&\quad - \frac{16 b_t^{\gamma} b_s^{\gamma}}{V_{\mathrm{b}}} \big\{ d \boldsymbol{r}^{\gamma+} \otimes \big(\boldsymbol{r}^{\gamma+} \times \boldsymbol{n}^{\gamma} \big) \otimes \boldsymbol{r}^{\gamma+} \otimes \big(\boldsymbol{r}^{\gamma+} \times \boldsymbol{n}^{\gamma} \big) \\
&\quad + \bar{d} \boldsymbol{r}^{\gamma+} \otimes \big(\boldsymbol{r}^{\gamma+} \times \boldsymbol{t}^{\gamma+} \big) \otimes \boldsymbol{r}^{\gamma+} \otimes \big(\boldsymbol{r}^{\gamma+} \times \boldsymbol{t}^{\gamma+} \big) + \bar{d} \boldsymbol{r}^{\gamma+} \otimes \big(\boldsymbol{r}^{\gamma+} \times \boldsymbol{s}^{\gamma+} \big) \otimes \boldsymbol{r}^{\gamma+} \otimes \big(\boldsymbol{r}^{\gamma+} \times \boldsymbol{s}^{\gamma+} \big) \big\} .
\end{aligned}
$$

Appendix G

Imaginary part of Fourier transform

Let $\mathcal{F}(f(t))=F(\omega)$, where $\mathcal{F}()$ denotes Fourier Transform (FT) of function $f(t)$. Let's write the real and imaginary parts of FT as $F_R(\omega)$ and $F_I(\omega)$. Then

$$\begin{aligned}\mathcal{F}^{-1}(F_R(\omega)) &= \frac{1}{2}\mathcal{F}^{-1}(F(\omega)+F^*(\omega)) \\ &= \frac{1}{2}(f(t)+f(-t)) \\ &= f_e(t)\end{aligned}$$

$$\begin{aligned}\mathcal{F}^{-1}(F_I(\omega)) &= \frac{1}{2\imath}\mathcal{F}^{-1}(F(\omega)-F^*(\omega)) \\ &= -\frac{\imath}{2}(f(t)-f(-t)) \\ &= -\imath f_o(t)\end{aligned}$$

Here, $f_e(t)$ and $f_o(t)$ stands for even and odd parts of $f(t)$. In short, $F_R(\omega)$ corresponds to f_e, while $F_I(\omega)$ corresponsds $f_o(t)$

So,

$$\mathcal{F}^{-1}(F_R(\omega)-\imath F_I(\omega)) = f_e(t)-f_o(t)$$

Appendix H

Verification of second derivative based on PDS-FEM

Let $f(x,y)=x^2y^2$ be the analytical function field in 2d domain shown in Figure H.1 where the origin of the (x,y) coordinate is on the centroid of the brick at the bottom left corner. The following expression are the 2nd derivative of the $f(x,y)$

$$\begin{aligned} f_{,xx} &= 2y^2 \\ f_{,xy} &= 4xy \\ f_{,yy} &= 2x^2 \end{aligned}$$

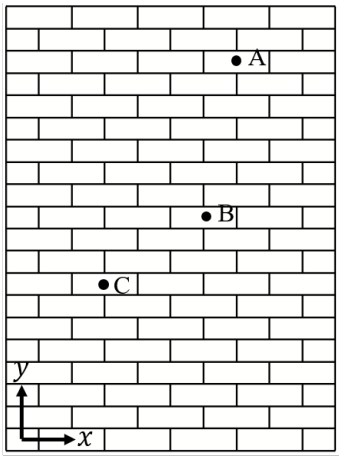

Figure H.1: 2d domain for the verification of second derivative based on PDS-FEM

Table H.1 shows the verification of the 2nd derivative based on PDS-FEM with the analytical expression above.

Table H.1: The comparison between numerical based on PDS-FEM and analytical results of the 2nd derivative of a function

Point	$f_{,xx}$			$f_{,xy}$			$f_{,xy}$		
	PDS	Analytical	Error(%)	PDS	Analytical	Error(%)	PDS	Analytical	Error(%)
A(1.4,2.295)	10.35	10.35	0.00	0.00	12.85	12.85	4.00	3.92	2.04
BA(1.2,1.35)	3.65	3.65	0.00	0.00	6.48	6.48	2.96	2.88	2.78
CA(0.6,0.945)	1.79	1.79	0.00	0.00	2.268	2.268	0.80	0.72	11.11

Bibliography

[1] Hori, M., Wijerathne, L., Chen, J., and Ichimura, T.: Continuumnization of regularly arranged rigid bodies, *Journal of JSCE*,Vol. 4, pp. 38-45, 2016.

[2] Wijerathne,M.L.L., Oguni, K. and Hori, M.: Numerical analysis of growing crack problem using particle discretization scheme, *Int. J. for Numerical Methods in Engineering*, Vol. 80, pp. 46-73, 2009.

[3] Ferris, M.C., Tin-Loi, F.: Limit analysis of frictional block assemblies as a mathematical program with complementarity constraints, *International Journal of Mechanical Sciences*: Vol. 43(1), pp. 209-224, 2001.

[4] Ordu$\widetilde{n}$a, A., Lourenco, P.B.:Three-dimensional limit analysis of rigid blocks assemblages. Part I: Torsion failure on frictional interfaces and limit analysis formulation, *International Journal of Solids and Structures*, Vol. 42, pp. 5140-5160, 2005.

[5] Portioli, F., Cascini,L., Casapulla, C., and D'Aniello, M.: Limit analysis of masonry walls by rigid block modelling with cracking units and cohesive joints using linear programming, *Engineering Structures,* Vol. 57, pp. 232–247, 2013

[6] Portiolia, F., Casapullaa, C., Gilbertb, M., Cascinia, L.: Limit analysis of 3D masonry block structures with non-associative frictional joints using cone programming, *Computers & Structures*, Vol. 143, pp. 108-121, 2014.

[7] Lourenco, P.B. and Rots, J. G.: Multisurface interface model for analysis of masonry structures, *Journal of Engineering Mechanics,* Vol. 123(7), pp. 660-668, 1997.

[8] Casapulla, C. and Portioli, F.: Experimental and analytical investigation on the frictional contact behavior of 3D masonry block assemblages, *Construction and Building Materials* Vol. 78, pp. 126-143, 2015.

[9] Furukawa, A., Kiyono, J., and Toki, K.: Numerical simulation of the failure propagation of masonry buildings during an earthquake, *Journal of Natural Disaster Science*, Vol. 33(1), pp. 11-36, 2012.

[10] Cakti, E., Saygılı ,Ö., Lemos, J., Oliveira, C. S., Discrete element modeling of a scaled masonry structure and its validation, Engineering Structures, Vol. 126, pp. 224-236, 2016

[11] Wang, S.Y., Sloan, S.W., Abbo, A.J., Masia M.J. and Tang, C.A. :Numerical simulation of the failure process of unreinforced masonry walls due to concentrated static and dynamic loading, *International Journal of Solids and Structures*, Vol. 49, Issue 2, pp. 377-394, 2012.

[12] Drougkas A., Roca P., Molins, C.: Numerical prediction of the behavior, strength and elasticity of masonry in compression, Engineering Structures, Vol. 90, pp. 15-28, 2015.

[13] Topping, B.H.V. and Wong, F.L.: Finite element modelling of the sonic method of testing masonry structures, *Computers & Structures*,Vol. 41(1), pp. 109-136, 1991.

[14] Hansapinyo, C. and Poovarodom, N.: Ambient Vibration Tests and Finite Element Analysis for Dynamic Properties of Brick Masonry Inverted Bell-shaped Chedi, *APCBEE Procedia,* Vol. (9), pp. 212 -216, 2014.

[15] Asteris, P.G., Chronopoulos, M.P., Chrysostomou, C.Z., Varum, H., Plevris, V., Kyriakides, N., and Silva, V.: Seismic vulnerability assessment of historical masonry structural systems, *Engineering Structures* Vol. 62–63, pp.118–134, 2014.

[16] Parajuli, H.R., Kiyono, J.,Taniguchi, H., Toki, K., Furukawa, A., and Maskey, P.N.: Parametric Study and Dynamic Analysis of a Historical Masonry Building of Kathmandu, *Disaster Mitigation of Cultural Heritage and Historic Cities*, Vol. 4, pp. 149-156, 2010.

[17] Parajuli, H.R.: *Determination of mechanical properties of the Kathmandu World Heritage brick masonry buildings*, The 15^{th} World Conference on Earthquake Engineering, Lisbon, Portugal, 2012.

[18] Brencich, A. and Sabia, D.: Experimental identification of a multi-span masonry bridge: The Tanaro Bridge, *Construction and Building Materials*, Vol. 22(10), pp. 2087-2099, 2008.

[19] Pavlov I.S., Potapov, A. I., Maugin, G.A., A 2D granular medium with rotating particles, International Journal of Solids and Structures, Vol. 43, pp. 6194–6207,2006.

[20] Yang, J., Sutton, M.: Nonlinear wave propagation in a hexagonally packed granular channel under rotational dynamics, International Journal of Solids and Structures,Vol. 77, pp. 65–73, 2015.

[21] Mouraille, O.: Sound propagation in dry granular materials: discrete element simulations, theory, and experiments, Thesis University of Twente, 2009.

[22] Stefanou, I., Sulem, J. and Vardoulakis, I.:Three-dimensional cosserat homogenization of masonry structures: elasticity, *Acta Geotechnica*, *Springer Verlag*, Vol. 3(1), pp.71-83, 2008.

[23] Stefanou, I., Sulem, J. and Vardoulakis, I.: Homogenization of interlocking masonry structures using a generalized differential expansion technique, *International Journal of Solids and Structures*, Vol. 47 (11-12), pp.1522-1536, 2010.

[24] Pau, A. and Trovalusci, P:Block masonry as equivalent micropolar continua: the role of relative rotations,Acta Mech, Vol. 223, pp 1455–1471, 2012.

[25] Salerno, G. and de Felice, G,:Continuum modeling of periodic brickwork,International Journal of Solids and Structures, Vol. 46, pp 1251–1267 , 2009.

[26] Cecchi, A. and Sab, K,:Discrete and continuous models for in plane loaded random elastic brickwork, European Journal of Mechanics, Vol. 28, pp 610–625 , 2009.

[27] Sorour M., Elmenshawi, A., Parsekian G., Mufti A., Jaeger L. G., DuchesneD.P.J., Paquette, J., and Shrive, N.: An experimental programme for determining the characteristics of stone masonry walls, Can. J. Civ. Eng. Vol. 38, pp 1204–1215, 2011.

[28] Godio M., Stefanou, I., Sab, K., Sulem, J., Dynamic finite element formulation for Cosserat elastic plates., Numerical Methods in Engineering, 101 (13), pp. 992-1018, 2015

[29] Giordano, A., Mele, E., and De Luca, A.,: Modelling of historical masonry structures: comparison of different approaches through a case study, Engineering Structures, Vol. 24, pp 1057-1069 , 2002.

[30] Elmenshawi, A., Sorour, M,. Mufti, A. Jaeger, L.G. and Shrive, N.: Damping mechanisms and damping ratios in vibrating unreinforced stone masonry, *Engineering Structures*, Vol. 32, pp. 3269-3278, 2010.

[31] Kačianauskas R., Kruggel-Emden, H., Markauskas D., Zdancevičius, E.: Critical assessment of visco-elastic damping models used in DEM simulations, Procedia Engineering, Vol.102, pp. 1415 – 1425, 2015.

[32] Caserta A. J., Navarro H. A., and Cabezas-Gómez L.: Damping coefficient and contact duration relations for continuous nonlinear spring-dashpot contact model in DEM, Powder Technology, Vol. 302, pp.462-479, 2016.

[33] Woodhouse, J.: Linear damping models for structural vibration, Journal of Sound and Vibration , Vol. 215(3), pp. 547-569, 1998

[34] Rabinovitch O., Madah, H.: Finite element modeling and shake-table testing of unidirectional infill masonry walls under out-of-plane dynamic loads, Engineering Structures,

[35] Resemini, S., Lagomarsino, S., and Giovinazzi, S.: Damping Factors and Equivalent SDOF definition in the displacement-based assessment of monumental masonry structures, First European Conference on Earthquake Engineering and Seismology,Geneva, Switzerland, Paper Number: 258, 2006

[36] Shakya, M., Varum, H., Vicente, R., and Costa, A.:Empirical Formulation for Estimating the Fundamental Frequency of Slender Masonry Structures, International Journal of Architectural Heritage, Vol. 10, NO. 1, pp. 55–66,2016

[37] Sorrentino, L., Al Shawa, O., and Decanini, L.D.:Experimental Evaluation of Impulsive Energy Damping in Masonry Collapse Mechanisms, 15 WCEE LISBOA, 2012.

[38] Sorrentino, L., Al Shawa, O., and Decanini, L.D.:The relevance of energy damping in unreinforced masonry rocking mechanisms. Experimental and analytic investigations, Bull Earthquake Eng, Vol. 9, pp. 1617–1642, 2011.

[39] Bolhassani, M., Hamid, A. A., Lau, A.C.W., Moon, F.:Simplified micro modeling of partially grouted masonry assemblages, Construction and Building Materials, Vol 83, pp. 159–173, 2015.

[40] Schuller, M., Berra, Atkinson, R., and Binda, L.: Acoustic tomography for evaluation of unreinforced masonry, *Construction and Building Materials*, Vol. 11(3) pp.199-204, 1997.

[41] Calderini, C., Cattari, S., and Lagomarsino, S. The use of the diagonal compression test to identify the shear mechanical parameters of masonry, *Construction and Building Materials*, Vol. 24, Issue 5, pp. 677-685, 2010.

[42] Fonseca, F.S., Mohamad, G., Lourenco, P.B., and Roman H.R.: *Deformation and Failure mode of masonry*, 12^{th} North American Masonry Conference, Denver, Colorado, 2015.

[43] Wang, J., Heath, A., and Walker, P.: Experimental investigation of brickwork behaviour under shear, compression and flexure, *Construction and Building Materials,* Vol. 48, pp. 448-456, 2013.

[44] Alecci, V., Fagone, M., Rotunno T., and Stefanom M. D.: Shear strength of brick masonry walls assembled with different types of mortar, Construction and Building Materialsm Vol. 40 , pp. 1038-1045, 2013.